EPITAXIAL GROWTH OF III-NITRIDE NANOSTRUCTURES AND APPLICATIONS FOR VISIBLE EMITTERS AND ENERGY GENERATION

by

BED NIDHI PANTHA

M. Sc., Tribhuvan University, 2001

AN ABSTRACT OF A DISSERTATION

submitted in partial fulfillment of the requirements for the degree

DOCTOR OF PHILOSOPHY

Department of Physics
College of Arts and Sciences

KANSAS STATE UNIVERSITY
Manhattan, Kansas

2009

Abstract

III-nitride nanostructures and devices were synthesized by metal organic chemical vapor deposition (MOCVD) for their applications in various photonic, optoelectronic, and energy devices such as deep ultraviolet (DUV) photodetectors, solar cells, visible emitters, thermometric (TE) power generators, etc.

Structural and optical properties in thicker AlN epilayers were found to be better than those in thinner AlN epilayers. Full-width at half maxima (FWHM) of x-ray diffraction (XRD) rocking curves as small as 63 and 437 arcsec were measured at (002) and (102) reflections, respectively in a thick AlN epilayer (4 μm). The dark current of the fabricated AlN detectors decreases drastically as AlN epilayer thickness increases. DUV photoluminescence (PL) spectroscopy and x-ray diffraction (XRD) measurements were employed to study the effect of biaxial stress in AlN epilayers grown on different substrates. Stress-induced band gap shift of 45 meV/GPa was obtained in AlN epilayers.

The potential of InGaN alloys as TE materials for thermopower generation has been investigated. It was found that as In content increases, thermal conductivity decreases and power factor increases, which leads to an increase in the TE figure of merit (ZT). The value of ZT was found to be 0.08 at 300 K and reached 0.23 at 450 K for $In_{0.36}Ga_{0.64}N$ alloy, which is comparable to that of SiGe based alloys.

Single phase $In_xGa_{1-x}N$ alloys inside the theoretically predicted miscibility gap region (x = 0.4 to 0.7) were successfully synthesized. A single peak of XRD ω-2θ scans of the (002) plane in InGaN alloys confirms that there is no phase separation. Electrical properties and surface morphologies were found to be reasonably good. It was found that growth rate should be high enough (>400 nm/hr) to achieve high quality and single phase $In_xGa_{1-x}N$ alloys in this miscibility gap region.

Mg-doped $In_xGa_{1-x}N$ alloys were synthesized and characterized by Hall-effect and PL measurements for their application as visible emitters. P-type conductivity was measured up to x = 0.35 with accepter activation energy as low as 43 meV, which is about 4 times lower than that of Mg-doped p-type GaN. Resistivity as low as 0.4 Ω-cm with a free hole concentration as high as 5×10^{18} cm^{-3} was measured in Mg-doped $In_{0.22}Ga_{0.78}N$. PL intensity decreased ~3 orders in magnitude when x increased from 0 to 0.22 in Mg-doped $In_xGa_{1-x}N$ alloys.

EPITAXIAL GROWTH OF III-NITRIDE NANOSTRUCTURES AND APPLICATIONS FOR VISIBLE EMITTERS AND ENERGY GENERATION

by

BED NIDHI PANTHA

M. Sc. in Physics, Tribhuvan University, 2001

A DISSERTATION

submitted in partial fulfillment of the requirements for the degree

DOCTOR OF PHILOSOPHY

Department of Physics
College of Arts and Sciences

KANSAS STATE UNIVERSITY
Manhattan, Kansas

2009

Approved by:

Major Professor
Jingyu Lin

Abstract

III-nitride nanostructures and devices were synthesized by metal organic chemical vapor deposition (MOCVD) for their applications in various photonic, optoelectronic, and energy devices such as deep ultraviolet (DUV) photodetectors, solar cells, visible emitters, thermometric (TE) power generators, etc.

Structural and optical properties in thicker AlN epilayers were found to be better than those in thinner AlN epilayers. Full-width at half maxima (FWHM) of x-ray diffraction (XRD) rocking curves as small as 63 and 437 arcsec were measured at (002) and (102) reflections, respectively in a thick AlN epilayer (4 μm). The dark current of the fabricated AlN detectors decreases drastically as AlN epilayer thickness increases. DUV photoluminescence (PL) spectroscopy and x-ray diffraction (XRD) measurements were employed to study the effect of biaxial stress in AlN epilayers grown on different substrates. Stress-induced band gap shift of 45 meV/GPa was obtained in AlN epilayers.

The potential of InGaN alloys as TE materials for thermopower generation has been investigated. It was found that as In content increases, thermal conductivity decreases and power factor increases, which leads to an increase in the TE figure of merit (ZT). The value of ZT was found to be 0.08 at 300 K and reached 0.23 at 450 K for $In_{0.36}Ga_{0.64}N$ alloy, which is comparable to that of SiGe based alloys.

Single phase $In_xGa_{1-x}N$ alloys inside the theoretically predicted miscibility gap region (x = 0.4 to 0.7) were successfully synthesized. A single peak of XRD ω-2θ scans of the (002) plane in InGaN alloys confirms that there is no phase separation. Electrical properties and surface morphologies were found to be reasonably good. It was found that growth rate should be high enough (>400 nm/hr) to achieve high quality and single phase $In_xGa_{1-x}N$ alloys in this miscibility gap region.

Mg-doped $In_xGa_{1-x}N$ alloys were synthesized and characterized by Hall-effect and PL measurements for their application as visible emitters. P-type conductivity was measured up to x = 0.35 with accepter activation energy as low as 43 meV, which is about 4 times lower than that of Mg-doped p-type GaN. Resistivity as low as 0.4 Ω-cm with a free hole concentration as high as $5x10^{18}$ cm^{-3} was measured in Mg-doped $In_{0.22}Ga_{0.78}N$. PL intensity decreased ~3 orders in magnitude when x increased from 0 to 0.22 in Mg-doped $In_xGa_{1-x}N$ alloys.

Table of Contents

Table of Contents ……………………………………………………………………………...v

List of Figures……………………………………………………………………………vii

List of Tables……………………………………………………………………………xiv

Acknowledgements…………………………………………………………………….....xv

Dedication....……………………………………………………………………………xvi

CHAPTER 1-Introduction ……………………………………………………………..1

1.1. Motivation……………………………………………………………………1

1.2. Brief history of III-nitride materials and devices……………………………..2

1.3. Dislocations and biaxial stain in III-nitrides…………………………………3

1.4. Thermoelectric properties of III-nitrides……………………………………..6

1.5. InGaN alloys and miscibility gap…………………………………………...10

1.6. Mg-doping in high In content $In_xGa_{1-x}N$ alloys for long wavelength emitters……..12

1.7. Overview of the thesis………………………………………………………14

CHAPTER 2- Experimental methods and tools…………………………………………15

2.1. Metal organic chemical vapor deposition…………………………………...15

2.2. MOCVD system ……………………………………………………………16

2.3. Material characterization……………………………………………………20

2.3.1. Measurement of thermal conductivity of thin films………………………20

2.3.2. Hall-effect measurement…………………………………………………..25

2.3.3. X-ray diffraction…………………………………………………………..28

2.3.4. Atomic force microscopy…………………………………………………30

2.3.5. Other characterization tools………………………………………………31

CHAPTER 3 - Structural and optical properties of AlN epilayers grown by MOCVD…………32

3.1. Introduction……………..32

3.2. Defects in crystals…………………………………………………………...33

3.3. Burger vectors………………………………………………………………35

3.4. Epilayer thickness dependence of optoelectronic and structural properties of AlN...36

3.5. Structural properties of silicon doped AlN…………………………………43

3.6. Correlation between biaxial stress and free exciton transition in AlN epilayers……50
CHAPTER 4- III-nitrides for thermoelectric thermopower generation…………………………59
4.1. Introduction…………………………………………………………………...59
4.2. Thermoelectricity……………………………………………………………60
4.2.1. The Seebeck effect………………………………………………..60
4.2.2. The Peltier effect……………………………………………………61
4.2.3. The Thomson effect…………………………………………………62
4.2.4. The Kelvin relation…………………………………………………..63
4.2.5. Basics of thermoelectric devices………………………………………63
4.2.6. Thermal and electrical conductivities………………………………..64
4.2.7. Thermoelectric figure of merit……………………………………………65
4.2.8. Thermoelectric power factor (*P*)…………………………………………..65
4.3. Experimental investigation of thermoelectric properties of InGaN alloys…………66
4.3.1. Optimization of power factor in InGaN alloys……………………………66
4.3.2. Thermal conductivity of InGaN alloys……………………………………72
4.3.3. Thermoelectric figure of merit in InGaN alloys…………………………..77
4.3.4. Conclusion and future direction of InGaN alloys as TE materials………..79
CHAPTER 5-Growth and characterization of single phase InGaN alloys in the middle range…81
5.1. Introduction……………………………………………………………………81
5.2. Growth conditions for the suppression of phase separation………………………...82
5.2.1. Biaxial strain……………………………………………………………83
5.2.2. Thermodynamic process…………………………………………………..85
5.2.3. Low growth temperature…………………………………………………86
5.3. Growth and characterization of single phase InGaN alloys………………………...87
5.4. Correlations between growth rate phase separation/suppression and film quality of $In_{0.65}Ga_{0.35}N$ alloys ..…………………………………………………………94
CHAPTER 6- Synthesis of p-type InGaN alloys for longer wavelength emitters………………99
6.1. Introduction……………………………………………………………………99
6.2. Basic working principle of semiconductor LDs…………………………………...100
6.3. InGaN based green LDs…………………………………………………………101
6.4. Electrical and optical properties of Mg-doped $In_xGa_{1-x}N$ ($0 \leq x \leq 0.35$) alloys……105

CHAPTER 7- General conclusion…………………………………………………………...115
References ………………………………………………………………………………...118
Appendix A – Publications…………………………………………………………………..129

List of Figures

Figure 1.1 Lattice mismatches of III-nitrides with different substrates…………………………...4

Figure 1.2 Schematic GaN/InGaN QW LED structure together with TEM showing the high density of threading dislocations [35]……………………………………………………..5

Figure 1.3 Applications of TE devices………………………………………………………7

Figure 1.4 Measured lattice thermal conductivity (K_L) and calculated average phonon mean free path (l_{mfp}) as functions of the period in Bi_2Te_3/Sb_2Te_3 SL and other reference materials [43]……………………………………………………………………………………. .9

Figure 1.5 A newly established low band gap for InN means that $In_{1-x}Ga_xN$ alloys cover the full solar spectrum [47]………………………………………………………………....11

Figure 1.6 Formation energy a function of Fermi level for Mg in different configurations (Ga-substitutional Mg_{Ga}, N-substitutional Mg_N, and interstitial configuration Mg_i). Also included are the native defects and interstitial H [56]…………………………………. 13

Figure 2.1 (Top) The picture of a custom built MOCVD system, (Bottom) Schematic illustration of a horizontal reactor. ………………………………………………………………..17

Figure 2.2 (a) Layer structure and (b) *In-situ* temperature profile and interference spectrum during growth for a LD structure……………………………………………………..19

Figure 2.3 Schematic relationship between current, voltage, and thermal transfer……………..21

Figure 2.4 (a) Basic electronics of 3ω method, (b) schematic of 3ω experimental set-up, and (c) schematic of metal pattern on the top of the sample. The narrow metal line serves as heater and sensor for the measurement of κ.. 22

Figure 2.5 An optical microscopic image of the top surface of the sample deposited with heater sensor pattern. Length and width of the metal line are 1500 and 20 μm respectively….24

Figure 2.6 Measured in-phase and out-of-phase ΔT (rms) at T = 300 K for a sapphire substrate and for 0.2-μm-thick SiO_2 on a sapphire substrate. Change in resistance of the metal line with temperature is shown in the inset…………………………………………………...25

Figure 2.7 Schematic diagram of Hall-effect measurement set up………………………………27

Figure 2.8 (Top) A picture of XRD systems and (Bottom) (002) and (102) rocking curves of AlN/Al_2O_3……………………………………………………………………………….29

Figure 2.9 (Left) AFM System (Q-Scope 250 model from Quesant Co.), (Right) An AFM image (size: 10 μm x 10 μm) of $In_{0.45}Ga_{0.55}N$ alloy. Surface roughness is ~ 1.8 nm…………...30
Figure 3.1 Motion of edge dislocation line under the shear stress [11]………………………….34
Figure 3.2 Motion of a screw dislocation under the shear stress………………………………...35
Figure 3.3 Schematic of finding Burger vector………………………………………………36
Figure 3.4 Epilayer thickness dependence of FWHM of (002) and (102) rocking curves of undoped AlN epilayers. XRD rocking curves of (002) and (102) planes for a 4 μm AlN epilayer are shown in the inset…………………………………………………………...37
Figure 3.5 Rocking curves of (00*l*) planes obtained from a 4 μm AlN epilayer in symmetric diffraction geometry…………………………………………………………………38
Figure 3.6 Plot of FWHM of (*hkl*) planes as a function of the lattice plane inclination angle (χ), according to Ref. 1 (solid points) and fitted with Eq. (3.2)……………………………40
Figure 3.7 Dark *I-V* characteristics of AlN MSM photodetectors fabricated from 1.5 and 4 μm thick AlN epilayers measured at bias voltages above 150 V. The inset shows the schematic of the device layout (device size = 80×80 μm^2 and finger width/spacing = 2/4 μm)……………………………………………………………………………..41
Figure 3.8 (a) PL emission spectra of AlN of different epilayer thicknesses *t*, (b) Epilayer thickness dependence of the ratio of the free exciton (FX) emission to the deep level impurity emission (I_{FX}/I_{imp}), the FWHM of the FX transition, and the peak position of the FX transition……………………………………………………………………..42
Figure 3.9 Angular shift (2θ) of (002) reflection in radial scan mode in an un-doped and Si-doped AlN epilayers……………………………………………………………………45
Figure 3.10 The Williamosn-Hall plot (W-H plot) using integral width of the (002), (004), and (006) rocking curves for an un-doped and Si-doped AlN epilayers…………………….47
Figure 3.11 FWHM of the rocking curves of the (*hkl*) planes as a function of lattice plane inclination angle (χ) with respect to sample surface for an undoped and several Si doped AlN epilayers and fitted with Eq. (3.2)…………………………………………………49
Figure 3.12 Dislocation densities of screw (N_{screw}) and edge (N_{edge}) type, as functions of N_{Si} calculated from Eqs. (3.1) and (3.3)……………………………………………………..49

Figure 3.13 10 K PL spectra of AlN/Al_2O_3, AlN/SiC, AlN/Si, and AlN/AlN bulk, measured in (a) a broad spectral range from 2.4 to 6.2 eV and (b) small spectral range from 5.8 to 6.2 eV……………………………………………………………………………………...52
Figure 3.14 The Arrhenius plot of the intensity of the dominant emission line (6.060 eV at 10 K) in AlN/Al_2O_3 epilayers. The measured activation energy is about 78 meV. (b) The Arrhenius plot of the intensity of the lower energy emission line (6.012 eV at 10 K) in AlN/AlN homoepilayers. The measured activation energy is about 16.4 meV. The inset shows the temperature evolution of the band edge emissions in AlN homoepilayers…...54
Figure 3.15 ω-2θ scan of (a) asymmetric (102) and (b) symmetric (002) reflection planes for an AlN homoepilayer and AlN bulk substrate……………………………………………55
Figure 3.16 (a) Free exciton spectral peak positions (E_P) and (b) in-plane lattice constants a of AlN epilayers grown on different substrates. Stress in AlN/Al_2O_3 is compressive and is tensile in AlN/SiC and AlN/Si epilayers……………………………………………...56
Figure 3.17 Stress-induced shift of the free exciton emission peak position in AlN epilayers as a function of the in-plane stress. The solid line is the least-squares linear fit of the experimental data. The linear coefficient of stress-induced bandgap shift in AlN epilayers is deduced to be 45 meV/GPa…………………………………………………………57
Figure 4.1 The history of TE material developments…………………………………………59
Figure 4.2 Schematic diagram for the Seebeck effect and A and B represent two different conductors…………………………………………………………………………..61
Figure 4.3 Schematic diagram for the Peltier effect………………..…………………………...62
Figure 4.4 Schematic diagram for the Thomson effect………………………………………62
Figure 4.5 Schematic diagram for TE devices…………………………………………………...64
Figure 4.6 TE parameters in different materials and carrier concentrations……………………..66
Figure 4.7 Schematic illustration of Seebeck coefficient (V_s) measurement method……………68
Figure 4.8 The measured Seebeck voltage V_s of $In_{0.3}Ga_{0.7}N$/GaN/sapphire samples of different electron concentrations (n) at as a function of ΔT………………………………………69
Figure 4.9 (a) Electrical conductivity (σ) and the Seebeck coefficient (S) and (b) power factor ($S^2\sigma$) as functions of electron concentration (n) of $In_{0.3}Ga_{0.7}N$ alloys…………………70

Figure 4.10 (a) Electrical conductivity (σ) and the Seebeck coefficients (S) and (b) power factor ($S^2\sigma$) as functions of temperature (T) of $In_{0.3}Ga_{0.7}N$ alloy with electron concentration ~$7x10^{18}$ cm^{-3}……………………………………………………………………...71
Figure 4.11 (a) Schematic illustration of cross sections and optical photograph of the top surface of a fabricated sample for 3ω measurements…………………………………………73
Figure 4.12 In-phase components of the temperature oscillation (ΔT) of the heater/sensor as a function of frequency of the driving current measured at 300 and 450 K for the reference (GaN/sapphire template) and an actual sample ($In_{0.28}Ga_{0.72}N$ epilayer grown on GaN/sapphire template)……………………………………………………………74
Figure 4.13 (a) Thermal conductivity (κ) of $In_xGa_{1-x}N$ alloys as a function of In content (x) at 300 K, (b) comparison of our data with AlGaN and InAlN [4, 5]………………………75
Figure 4.14 (a) Seebeck coefficient (S) and electrical conductivity (σ) of $In_xGa_{1-x}N$ alloys as functions of In content (x). (b) Power factor ($P=S^2\sigma$) and figure of merit (ZT) of $In_xGa_{1-x}N$ alloys as functions of In content (x) measured at 300 K……………………...77
Figure 4.15 Measured ZT values of $In_{0.36}Ga_{0.64}N$ alloy from 300 to 450 K. Data for SiGe alloys [25] are included for comparison……………………………………………………...78
Figure 5.1 Binodal (solid) and spinodle (dahed) curves for the InGaN alloys, calculated assuming a constant average value for the solid phase interaction parameter [11]………………...83
Figure 5.2 T-x phase diagrams of ternary $In_xGa_{1-x}N$ alloys for (a) relaxed layers, (b) strained layers [14]……………………………………………………………………………..84
Figure 5.3 (a) X-ray diffraction spectra of (002) plane of $In_{0.65}Ga_{0.55}N$ alloys of different layer thickness in ω-2θ scan mode, (b) Layer structure……………………………………….85
Figure 5.4 ω-2θ x-ray diffraction spectra of (002) plane of $In_{0.65}Ga_{0.55}N$ alloys grown at different growth rate G_R………………………………………………………………………………86
Figure 5.5 XRD ω-2θ spectra of (002) plane of $In_{0.46}Ga_{0.54}N$ alloys grown at different growth temperature T_G……………………………………………………………………………...87
Figure 5.6 In composition (x) and growth rate (R_G) of $In_xGa_{1-x}N$ alloys as functions of growth temperature (T_G). Solid lines are linear fit of data………………………………………89
Figure 5.7 XRD ω-2θ curves of (002) planes of $In_xGa_{1-x}N$ alloys grown on GaN/Al_2O_3 templates (a) in linear scale and (b) in semi-log scale. The inset shows the full width at half maxima

(FWHM) and relative intensities as functions of In content. In contents # are also indicated in the figures…………………………………………………………………...90

Figure 5.8 (a) XRD (002) rocking curves for different InGaN alloys and (b) variation of FWHMs as a function of In content in $In_xGa_{1-x}N$ alloys………………………………………….92

Figure 5.9 (a) AFM images and (b) surface roughness (RMS) as functions of In content in $In_xGa_{1-x}N$ alloys…………………………………………………………………………93

Figure 5.10 (a) Hall mobility and (a) electron concentration as functions of In content in $In_xGa_{1-x}N$ alloys. The layer structure employed for this study is shown in the inset of (a)……………………………………………………………………………………...93

Figure 5.11 (a) XRD spectra of (002) ω-2θ scan of $In_{0.65}Ga_{0.35}N$ alloys at different growth rate R_G, (b) In content as a function of growth rate G_R with fixed growth temperature T_G and pressure P…………………………………………………………………………...95

Figure 5.12 FWHMs and intensity of XRD spectra of (002) (a) ω-2θ scan (b) ω-scans of $In_{0.65}Ga_{0.35}N$ alloy as a function of growth rate, R_G……………………………………97

Figure 5.13 Hall mobility of electrons μ and background electron concentration n of $In_{0.65}Ga_{0.35}N$ alloy as functions growth rate G_R……………………………………………………..97

Figure 6.1 Schematic illustrations of a typical (a) LD structure, (b) band structures, (c) refractive index profile for wave guiding, (d) Intensity profile of optical mode………………….100

Figure 6.2 (a) Layer structure for 500 nm laser diode (b) and electronic band diagram near active region……………………………………………………………………………...102

Figure 6.3 (a) Probe station where LD structure is emitting light under the forward bias @ 20 mA dc current (b) and EL spectrum showing peak emission wavelength ~ 500 nm…..102

Figure 6.4 Schematic of a fabricated ridge waveguide laser diode grown on sapphire substrate. ……………………………………………………………………………………103

Figure 6.5 (a) I-V and (b) L-I characteristics of a fabricated LD device………………………104

Figure 6.6 Room temperature (a) hole concentration p, (b) hole mobility μ_h, and (c) reistivity ρ as functions of In content x in Mg doped $In_xGa_{1-x}N$ alloys……………………………109

Figure 6.7 The Arrhenius plot of free hole concentration, p, in Mg doped $In_xGa_{1-x}N$ alloys…..110

Figure 6.8 Energy level E_A of Mg acceptors in Mg doped p-$In_xGa_{1-x}N$ alloys as a function of In content x. Data from references available up to x = 0.17 are also included……………111

Figure 6.9 Photoluminance spectra of Mg-doped p-type $In_xGa_{1-x}N$ alloys measured at 10 K…112

Figure 6.10 Integrated PL intensity, I_{int}, peak position of Mg related emission $E_{p,}$ and Mg acceptor energy levels as functions of In content x. (a) E_A, (b) E_p, (c) I_{int} (c)…………113

List of Tables

Table 1.1 In-plane lattice constants and thermal expansion coefficients of III-nitrides and commonly used substrates [32]……………………………………………………………..12

Table 1.2 Calculated E_A of possible acceptors for GaN and other III-V compound semiconductors [55]………………………………………………………………………...46

Acknowledgements

First, I would like to take this opportunity to thank my supervising advisors, Professor Jingyu Lin and Professor Hongxing Jiang. This work could not have been completed without their valuable advice, encouragement and guidance. Their depth of understanding and ability to relate many ideas together are highly appreciated. I have enjoyed the extraordinary facilities and supportive research environment they have provided me.

I am much indebted to Dr. Jing Li for teaching me III-nitride materials growth, their characterization, and MOCVD techniques. Thank you Dr. Li so much.

I would also like to thank my supervisory committee members Professor Michael O'Shea and Professor Christopher Culbertson, and external chairperson Professor Hayder Rasheed for their valuable advice and time.

I would like to acknowledge my past and present colleagues, Dr. Zhaoyang Fan, Professor Jin Sixuan, Dr. Jagat Shakya, Dr. Mim Nakarmi, Dr. Neeraj Nepal, Dr. Talal Al Tahtamouni, Dr. Cris Ugolini, Dr. Neelam Khan, Rajendra Dahal, Ashok Sedhain, I-Win Feng, and Weiping Zhao for their cooperation, help, and for all the informative discussions we had together.

Many thanks go to Department of Physics K-State University for giving me the opportunity for graduate studies and Department of Electrical and Computer Engineering Texas Tech University for providing internships. I would also like to thank Mr. Frank Jiang for proof-reading of this thesis.

Last but not least, I would like to thank my wife, parents, and other family members for their devoted love, endless support and encouragement throughout my life. Specially, I am grateful to my wife Narmada and sons who always stand with me.

Dedication

To my loving parents Biniram and Radhika, wonderful wife Narmada and lovely sons Bidur and Biraj

CHAPTER 1 - Introduction

1.1. Motivation

III-nitride compound semiconductors and their alloys have been the subject of intense scientific research during the last decade due to their potential importance in a broad range of optoelectronic/photonics device applications. Depending on the alloy composition, the direct band gap of nitrides varies from about 0.7 eV to 6.1 eV, covering a wide wavelength range from infrared (IR) to ultraviolet (UV) [1-6]. III-nitride based devices can also be operated in high temperature/power and other harsh conditions [7]. With these unique properties and the availability of both n- and p-type conductivities, commercial products such as blue-green light emitting diodes (LEDs) and near-UV laser diodes (LDs) are already available [3]. Additionally, the emission wavelength of emitters is now rapidly expanding towards the longer wavelength regions [8]. Further progress in epitaxy, technology, and physical understanding of this important material system is predicted to have a strong impact on a number of technological fields including solid state lighting, photovoltaic technology, high power/high frequency electronics, and UV-visible optoelectronics [1-8]. Photovoltaic application of III-nitride materials is relatively new and thus requires tremendous efforts, particularly in improving the material quality of relatively high In content InGaN alloys. Challenges of achieving high quality high In content InGaN alloys with the current advanced growth technology include solid phase immiscibility between InN and GaN, intrinsic defects and impurities, a high density of dislocations, and an insufficient supply of nitrogen atoms due to low ammonia cracking efficiency at lower growth temperatures.

Although III-nitrides are being extensively studied for optoelectronic applications, their prospects in thermoelectric (TE) technology are rarely studied [9-11]. Thermoelectric devices such as power generators and coolers are solid state energy devices, which convert heat energy into electrical energy without emitting toxic gases or hazardous radiation and without the need for moving parts. Some of the outstanding features of III-nitride alloys and nanostructures such as the ability for high power and high temperature operation [7], high mechanical strength and stability, and radiation hardness [12] etc are highly attractive features for TE applications. Investigations concerning the potential of III-nitrides for thermopower generation will be discussed.

1.2. Brief history of III-nitride materials and devices

GaN was first produced by Jusa and Hahn, in 1938 in the form of small needles and platelets by passing ammonia over hot gallium metal [13]. After three decades (in 1969), large area GaN was grown directly on sapphire substrate by Maruska and Tietjen by hydride vapor phase epitaxy (HVPE) [14]. Unfortunately, these samples suffered from very high background electron concentrations ($\sim10^{18}$-10^{20} cm^{-3}). In 1983, Yoshida *et al.* employed an AlN intermediate layer and demonstrated that the cathodoluminescence efficiency of the overlaying GaN layer was improved [15]. Later, this idea was further developed by Akasaki *et al.* and Nakamura with a thin AlN nucleation layer [16] or GaN nucleation layer [17] grown at low temperatures (500-750 $^{\circ}C$) prior to the growth of high temperature GaN epilayer. A low temperature nucleation layer promotes the GaN growth mode from 3D islands to 2D growth mode and leads to a flat and smooth GaN epilayer surface. The success in *p*-type doping is another breakthrough in the history of GaN growth [18-20]. Group II elements Zn, Cd, Mg or Be were investigated as p-type dopants. Unfortunately, with these dopants, GaN layers were always found to be very resistive

[21-25]. Pankove and co-workers were able to make the first nitride (LED) consisting of an un-doped n-type region, an insulating Zn-doped layer, and an indium surface contact, but this device suffered from very low efficiency [26]. Amano and Akasaki converted an insulating Mg-doped GaN layer to a conductive *p*-type layer using the low energy electron beam irradiation (LEEBI) method [27]. Later, Nakamura *et al* [28] discovered that post growth thermal annealing in hydrogen free ambient is found to be very effective way of achieving p-type conductivity in Mg-doped GaN. Since then, thermal annealing has been established as a standard method for achieving p-type conductivity in MOCVD grown Mg-doped GaN. The success of p-type GaN was a milestone of having today's GaN related devices. High-brightness blue LEDs with a brightness of over 1 candela and ultraviolet LDs were demonstrated by Nakamura in 1994 and 1995, respectively [29]. After the discovery of very narrow band gap InN (0.7 eV instead of previously thought 1.9 eV), in 2002 [4-6], III-nitrides have promised tremendous potential for photovoltaic and photoeletrolysis technology [12, 30, 31].

1.3. Dislocations and biaxial stain in III-nitrides

III-nitrides are generally grown on largely lattice mismatched substrates such as sapphire, SiC, and Si and thus suffer from a high density of threading dislocations (TDs) which can exceed 10^{10} cm^{-2}. Generally, there are three kinds of dislocations: pure edge, pure screw, and a combination of both (mixed). Table 1.1 compares the lattice constants and thermal expansion coefficients of III-nitrides with commonly used substrates [32]. It shows that InN has a lattice mismatch as high as about 25% with sapphire, the most commonly used substrate. An increasing number of growth techniques have recently been developed to reduce the defects and dislocations embedded in the GaN epitaxial films. Vaudo *et al.* [33] demonstrated the feasibility of obtaining a low density of threading dislocations (5.3×10^6 cm^{-2}) in GaN epitaxial layers by

directly growing a 300 μm GaN layer onto sapphire substrate by a single step HVPE method. Marchand *et al.* [34] observed that the density of mixed-character and pure edge threading dislocations in the laterally overgrown GaN can be reduced by at least 3-4 orders of magnitude.

Substrates	Sapphire (001)	SiC	Si (111)	AlN	GaN	InN
Lattice constant, a (Å)	4.758	3.0730	3.840	3.112	3.189	3.533
Thermal expansion coefficient ($^{-}$K)	7×10^{-6}	4.3×10^{-6}	2.6×10^{-6}	3.042×10^{-6}	5.0×10^{-6}	3.83×10^{-6}

Table 1.1 In-plane lattice constants and thermal expansion coefficients of III-nitrides and commonly used substrates [32].

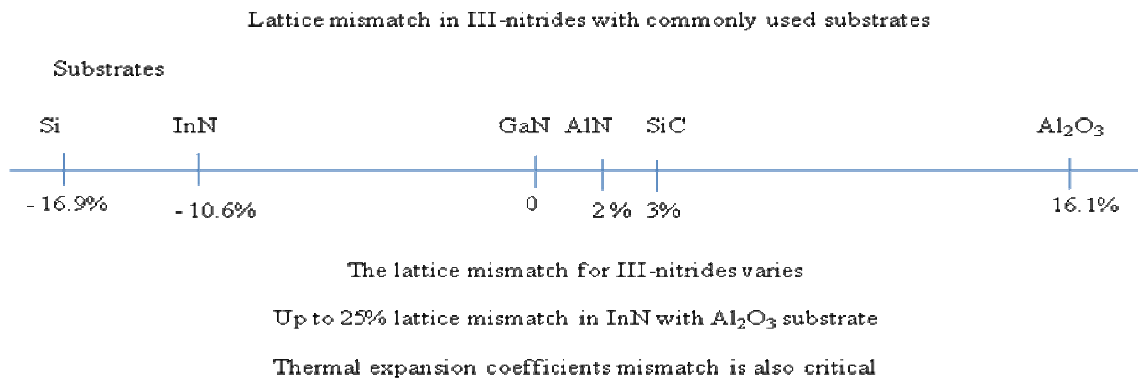

Figure 1.1 Lattice mismatches of III-nitrides with different substrates.

The density of TDs can be measured directly by transmission electron microscopy (TEM). Unfortunately, this process is destructive and time consuming. Fig. 2, for example, shows both cross-sectional and plane view TEM images of an InGaN QW LED grown on sapphire substrates [35]. The image clearly shows that the device is overwhelmingly suffered by dislocations. Alternatively, non-destructive x-ray diffraction (XRD) is a widely applied method to evaluate the crystalline perfection of epitaxial layers [36, 40]. Besides the commonly performed fast qualitative analysis, XRD enables quantitative estimations of density TDs as well. A common approach is to describe highly distorted heteroepitaxial layers as mosaic crystals. They are characterized by both the mean size of the mosaic blocks and the mean angle of their rotation against each other. The mean tilt (out-of-plane rotation) and twist (in-plane rotation) angles are utilized to estimate the screw and edge types of dislocations, respectively [37]. Tilt and twist are determined from the full width at maxima (FWHM) of rocking curves of crystallographic planes [36].

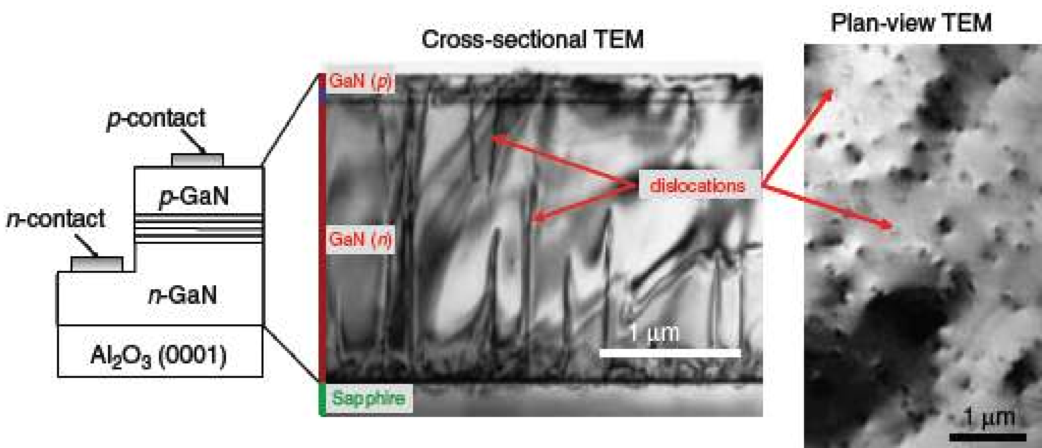

Figure 1.2 Schematic GaN/InGaN QW LED structure together with TEM showing the high density of threading dislocations [35].

III nitride epilayers grown on foreign substrates are known to have either compressive or tensile stress due to the large lattice and thermal expansion coefficients mismatch between substrates and epilayers. III-nitrides are under compressive stress on sapphire substrates while they are under tensile stress on Si and SiC substrates. State of stress (tensile or compressive) also depends on doping. For examples, un-doped AlN grown on sapphire is under compressive stress while it changes into tensile stress beyond certain Si doping concentrations. In addition to band gap shift, stress influences the electrical and optical properties of the devices through the piezoelectric effect. Furthermore, if not properly managed, stress may cause cracks in relatively thick epilayers. XRD and Raman spectroscopy are generally used to study stress induced and energy band gap shift on heterepitaxially grown epilayers. Recently, we have established that photoluminance is another simple method to monitor substrate induced biaxial stress and its influence on band gap and optical properties (Chapter 3).

1.4. Thermoelectric properties of III-nitrides

Thermoelectric (TE) devices convert heat energy directly into electrical energy. In a typical TE device, a junction is formed from two dissimilar conducting materials, one containing negative charge carriers (electrons) and the other positive charge carriers (holes). When an electric current is passed in the appropriate direction through the junction, both types of charge carriers move away from the junction and take the heat away, thus cooling the junction. Similarly, a heat source at the junction causes carriers to flow away from the junction, making an electrical generator. They have no moving parts, are lightweight, small, and inexpensive. They can be used to completely eliminate the need for CFCs or HCFCs and heavy compressors in small-scale refrigeration [41]. However, use of TE devices for large scale-refrigeration or power generation is limited because of low efficiency. Currently, major uses of TE devices include

cooling of laser diodes and providing power for deep space satellites where there is no sunlight (beyond solar system). Fig. 1.3 shows some of the applications of TE devices.

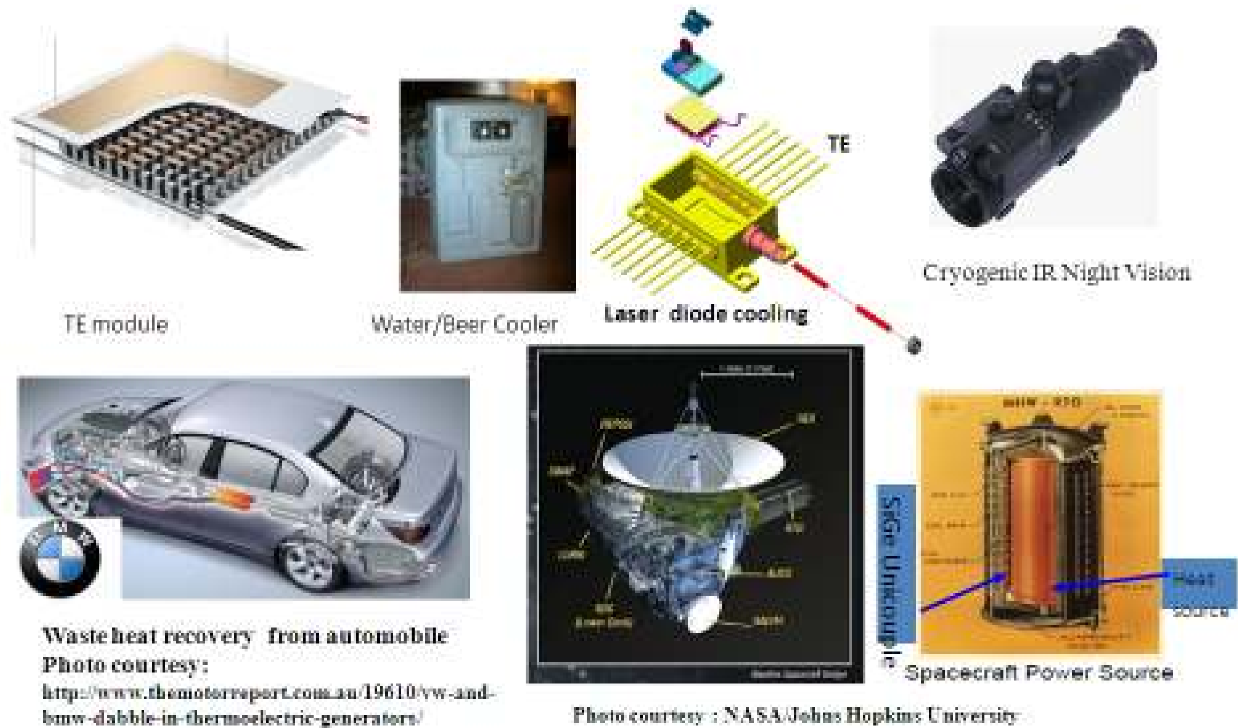

Figure 1.3 Applications of TE devices

The performance of TE materials can be quantified by the TE figure-of-merit $ZT=S^2\sigma T/\kappa$. Here, S is the Seebeck coefficient, σ is the electrical conductivity, κ is the thermal conductivity, and T is the absolute temperature. Thus, good TE materials should have high S, high σ and low κ. An ideal TE material should behave like a perfect crystal for electron and perfect glass for phonons.

Choice of material for TE application is very important because κ, S and σ couple together. Due to high κ, prospects of binary compounds such as InN, GaN, and AlN as TE materials are limited. However there are number of ways of reducing κ.

(a) Solid solution alloys: Thermal resistance of these materials is shown to be due to scattering of phonons by mass fluctuations and anharmonic phonon–phonon scattering. There are two-phonon point defect processes, three phonon anharmonic processes, and five phonon processes resulting from simultaneous processes of both. Three phonon processes are N-processes and U-processes where total momentum is conserved in the first case and total momentum is changed by a reciprocal lattice vector in the second case. The other phenomenon is the scattering of phonons due to lattice strains. Alloys whose components have widely differing lattice constants usually contain a large concentration of strained regions, which scatter phonons effectively [42].

(b) Low dimensional structure: Recently, research in thermoelectric materials has entered into a new era with the help of inspiration from band structure and phonon engineering in low dimensional structures such as quantum wells or supperlattices (SL), nanowires etc. κ in LS is found to be much less than that in bulk or homogenous alloys. A variety of mechanisms such as mismatch in acoustic impedance and phonon spectra, miniband formation, and interface scattering due to roughness and defects have been proposed as contributors [43]. Figure 1.4 shows κ as a function of SL period in Bi_2Te_3/SbTe SL system. κ in SL is found to be ~2.4 times smaller than that in homogeneous alloys.

(c) Nanostructured materials: Alloys and SL mainly scatter the phonons of short wavelengths, so the long wavelength phonons are still transporting heat. One way to further reduce κ is to scatter these phonons as well. Incorporation of nanoparticles, defects or grain boundaries of sizes comparable to the long wavelength phonons can further reduce κ [44].

We have chosen InGaN alloys for the TE properties investigations because, besides alloy scattering, one can expect that κ can be reduced significantly by lattice strains due to the large difference of lattice constants between InN and GaN. As we expected, a significant reduction in κ has been observed in higher In content InGaN alloys, indicating their promising potential for TE applications. Other properties such as the Seebeck coefficient and electrical conductivity were also found to be reasonably good. Further, with the current advanced growth methods such as MOCVD, one can easily incorporate low dimensional nanostructures with great ease.

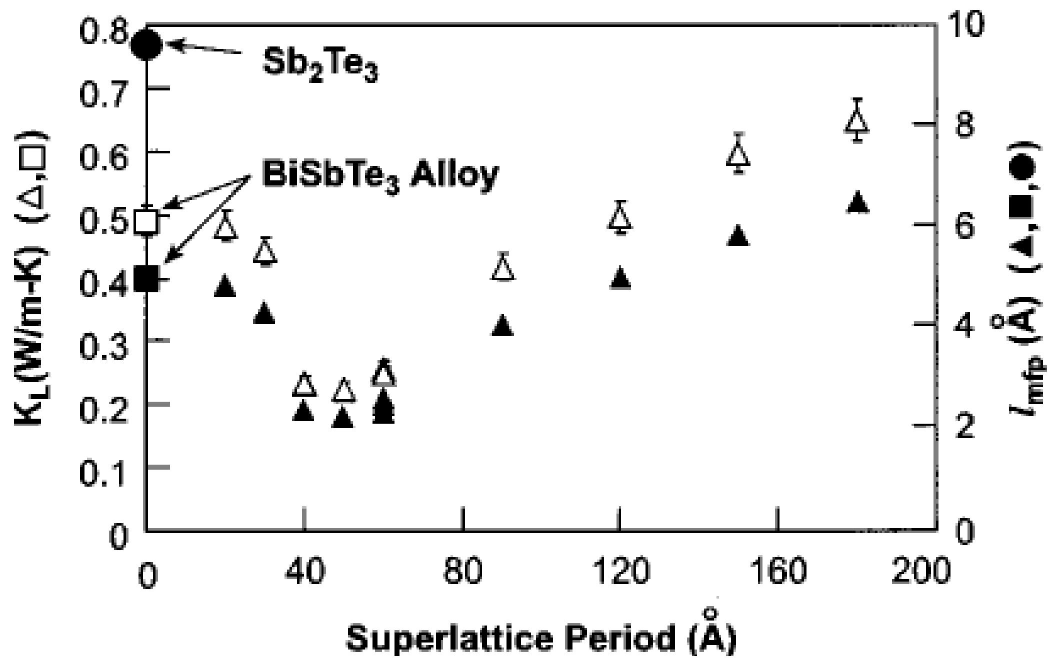

Figure 1.4 Measured lattice thermal conductivity (K_L) and calculated average phonon mean free path (l_{mfp}) as functions of the period in Bi_2Te_3/Sb_2Te_3 SL and other reference materials [43].

1.5. InGaN alloys and miscibility gap

InGaN is mainly being used as an active layer in nitride blue-green LEDs and LDs. Emission wavelengths of LEDs or LDs can be varied by changing the amount of In content in InGaN QWs. The success of super-bright LEDs and LDs is predominately attributed to the high quality of InGaN, which can be synthesized by several novel epitaxial techniques such as MOCVD and molecular beam epitaxy (MBE), etc [3, 45, 46]. After the discovery of the narrow band gap of InN (0.7 eV) in 2002 [4-6], $In_xGa_{1-x}N$ alloys have attracted tremendous attention as photovoltaic materials. This discovery means a single system of alloys, i. e. $In_xGa_{1-x}N$, can cover virtually the full solar spectrum as shown in Fig 1.5 [47]. Furthermore, InGaN can tolerate radiation levels an order of magnitude higher than existing space-based solar cell materials [12]. Because of these reasons, InGaN alloys are considered to be ideal candidates for radiation hard multi-junction (MJ) solar cells. The generation of hydrogen by using sunlight to split water is another potential field of application for InGaN alloys, as the optimum band gap to split water can be obtained by a proper composition of InN and GaN [48-50].

Although InGaN has been recognized as a novel optoelectronic/photonics material [3], there are only a few reports on the optical, structural, and electrical properties of relatively thick InGaN alloys suitable for solar cells and other applications [9-11, 48-50]. The material quality of InGaN with relatively high In content severally degrades due to phase separation, inhomogenenity of solid solution, and In metal droplets (due to decomposition of InN) as layer thickness increases. Phase separation and indium droplets are normally observed in thick InGaN with relatively higher In content [51]. Recently, methods for suppressing phase separation have been developed and the feasibility single phase InGaN alloys synthesis in the entire compositional range has been demonstrated by MOCVD and MBE; however, material quality is

not good enough to realize practical devices [52, 53]. The synthesis of high quality InGaN alloys with relatively high In content is needed in order to efficiently harvest energy using photovoltaic, thermoelectric, and phtoelectrolysis technologies.

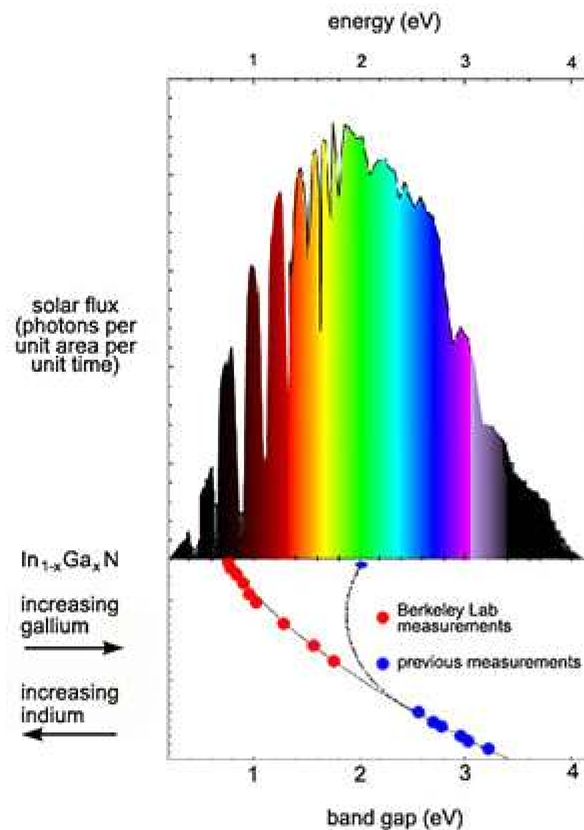

Figure 1.5 A newly established low band gap for InN means that $In_{1-x}Ga_xN$ alloys cover the full solar spectrum [47].

1.6. Mg-doping in high In content $In_xGa_{1-x}N$ alloys for long wavelength emitters

High free hole concentration in Mg-doped GaN is difficult to achieve due to the large binding energy of Mg acceptor (E_A) and the presence of donor-like impurities such as hydrogen, nitrogen vacancies, etc. Table 1.2 compares E_A of various potential acceptors for GaN together with other III-V semiconductors [54]. E_A of GaN for all possible potential acceptors are much larger than those of other III-V semiconductors. Fig 1.6 shows the formation energies of possible donor-like impurities and vacancies in Mg doped GaN [55]. In Mg-doped GaN hydrogen impurities (H^+) and nitrogen vacancies are ($V_N^{3+}$and V_N^+) formed easily, as their formation energies are low and behave as donors which compensate acceptors.

Binding energy (meV)	GaAs	InP	GaP	GaN
C	27	41.3	54	230
Mg	28.8	48	59	250
Zn	30.7	46.4	69.7	340
Cd	34.4	57	102.2	550

Table 1.2 Calculated Acceptor binding energies of possible acceptors for GaN and other III-V compound semiconductors [53].

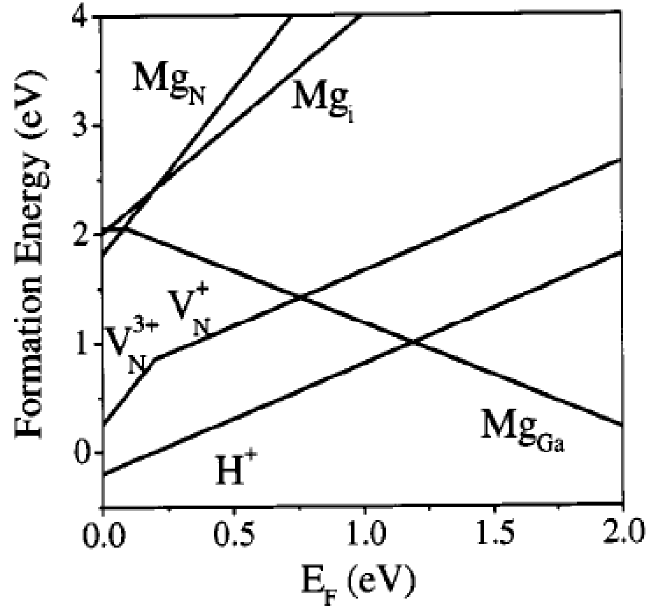

Figure 1.6 Formation energy a function of Fermi level for Mg in different configurations (Ga-substitutional Mg_{Ga}, N-substitutional Mg_N, and interstitial configuration Mg_i). Also included are the native defects and interstitial H [54].

With the great success of high brightness blue green LEDs and LDs near UV-blue region in commercial production, nitrides research has also extended toward long wavelength emitters with applications in full color displays, laser TV, and pocket projectors, etc. Potential degradation of the active region i.e. InGaN/GaN multiple-quantum-wells (MQWs) during the relatively high-temperature growth of the *p*-layer is a great challenge to realize long wavelength emitters (> 600 nm). The low temperature synthesis of p-type $In_xGa_{1-x}N$ (< 800 ^oC) compared with p-type GaN (~ 1000 ^oC) could be one of the best options for avoiding such degradation of active region. Besides its low growth temperatures, another benefit of using a high In content *p*-$In_xGa_{1-x}N$ layer is higher hole concentration and conductivity compared with Mg doped p-type GaN due to the lower E_A of the Mg acceptor.

1.7. Overview of the thesis

This thesis is divided into 7 chapters. Chapter 1 includes a brief introduction and motivation. Chapter 2 describes the experimental methods and tools employed in this work with emphasizing MOCVD growth and TE characterizations. Results are discussed in chapter 3 through 6. Chapter 3 discusses the structural characterization of AlN epilayes by XRD. The potential of InGaN as TE material is investigated in chapter 4. Chapter 5 is devoted to synthesize high quality $In_xGa_{1-x}N$ alloys in the middle composition range for photovoltaic and TE applications. P-type doping of high In content InGaN alloys is discussed in chapter 6. Lastly, this thesis is wrapped-up with general conclusions in chapter 7.

CHAPTER 2- Experimental methods and tools

In this chapter, the experimental tools and methods employed in this work are discussed. The metal organic chemical vapor deposition (MOCVD) technique and thermal conductivity measurements of thin films and nanostructures are primarily discussed. Other thin films characterization tools such as x-ray diffraction (XRD), Hall-effect measurement, atomic force microscopy (AFM), optical microscopy, photoluminance (PL), and electroluminescent (EL) are also discussed briefly.

2.1. Metal organic chemical vapor deposition

Chemical vapor deposition (CVD) is a process in which the chemical constituents react in vapor phase on or near the heated substrates to form a solid deposit. MOCVD is a specialized form of CVD which utilizes metalorganic compounds as sources of deposition elements. The basic aspects of MOCVD including thermodynamics, hydrodynamics, and kinetics, both in the gas phase and on the surface, are found elsewhere [56]. For the synthesis of III-V nitrides, metalorganic (MO) compounds, such as trimethyl-gallium (TMGa), are used as sources for the group-III elements and hydride gases, such as ammonia, for group-V elements. Typically, ammonia reacts with the MO compounds in hydrogen or nitrogen ambient under appropriate temperature and pressure conditions, producing molecules of the required semiconductor material, which then adsorbs on the substrate, producing an epitaxial layer. The key reaction process can be expressed as follows,

$$A^{III}R_3 + B^{V}X_3 \rightarrow A^{III}B^{V} + \text{Organic by-products} \quad (2.1)$$

where, A^{III} and B^{V} are cations and anions, respectively. R is an alkyl radical such as methyl (CH_3) or ethyl (C_2H_5) or other organic groups and X is usually hydrogen. For GaN growth, the reaction is as follows,

$$Ga(CH_3)_3\,(g) + NH_3\,(g) \rightarrow GaN\,(s) + 3CH_4\,(g), \qquad (2.2)$$

Synthesis of material using MOCVD technique was first reported in 1960 [57] to deposit InP and InSb. It is now a proven technique and used on a large scale, particularly in semiconductor and opto-electronic applications [58].

2.2. MOCVD system

III-nitride materials and device structures that were prepared for this work were synthesized by MOCVD method. A picture of a custom built MOCVD system used for this work and a schematic of its reactor part is shown in Fig 2.1. The MOCVD system consists of four main components; gas handling system, reaction chamber, heating/temperature control system, and vacuum/exhaust system. Pneumatic valves and mass flow controllers are used to control the MO and carrier gas flows. Two separate gas delivery lines are used in order to suppress gas phase pre-reaction between ammonia and the MO sources. Two types of ultra high pure (99.999%) carrier gases are available for the described system; nitrogen and hydrogen. However, due to the reactivity of MO compounds with water vapor and oxygen, some kind of system must be incorporated for drying and purifying the carrier gas. In our system, H_2 carrier gas can be purified through a heated (~ 400 °C) palladium (Pd) cell membrane [59].

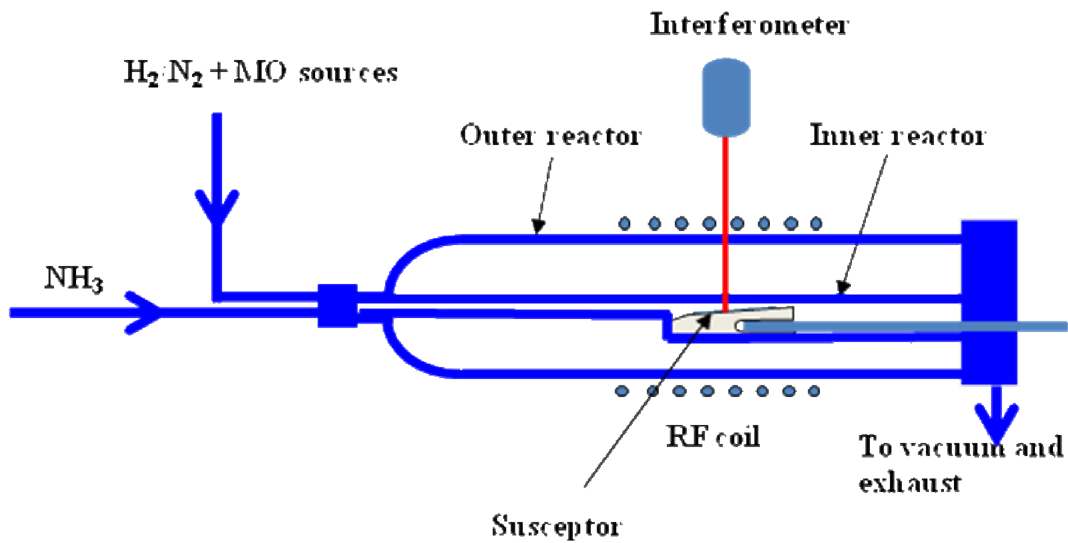

Figure 2.1 (Top) The picture of a custom built MOCVD system, (Bottom) Schematic illustration of a horizontal reactor.

A schematic of a horizontal reactor is depicted in Fig. 2.1 (Bottom). Outer and inner reactors consist of clear fused quartz tubes. Substrates on which thin films are to be deposited are held on the graphite susceptor coated with boron nitride. A 10 kW RF generator (TIG-10/100) was used for heating the susceptor. Temperature is controlled by Eurotherm temperature (Model-904) and measured by an R-type thermocouple. A high capacity mechanical pump (Pfeiffer DUO-350) is used to pump down the system to low pressure. With the aid of a turbo pump, the system can be pumped down to a high vacuum (10^{-5} Torr). A throttle valve (MKS-Type-653) is used to adjust the reactor pressure in conjunction with the pressure controller (MKS-Type-651C) and the pressure sensor (MKS-Type 722). An interferometer (EpiEye-2000) is coupled to the system for *in-situ* monitoring of surface and thickness during growth. The system is fully automatic and controlled by a computer. Five MO sources; trimethylgallium (TMGa), triethylgallium (TEGa), trimethylaluminium (TMAl), trimethylindium (TMIn), and biscyclopentadienyl-magnesium (Cp_2Mg) can be hooked up in the system which provide Ga, Ga, Al, In, and Mg, respectively. All MO sources are placed in the temperature controlled reservoir to maintain constant vapor pressure. The system has four gas lines for H_2, N_2, NH_3 and SiH_4. H_2 and N_2 are used as carrier gases, NH_3 provides N element, and SiH_4 is used as source of silicon for n-type doping. Fig 2.2 (b) shows a typical *in-situ* interference pattern and temperature profile during growth of an InAlGaN laser diode (LD) structure shown in Fig. 2.2 (a).

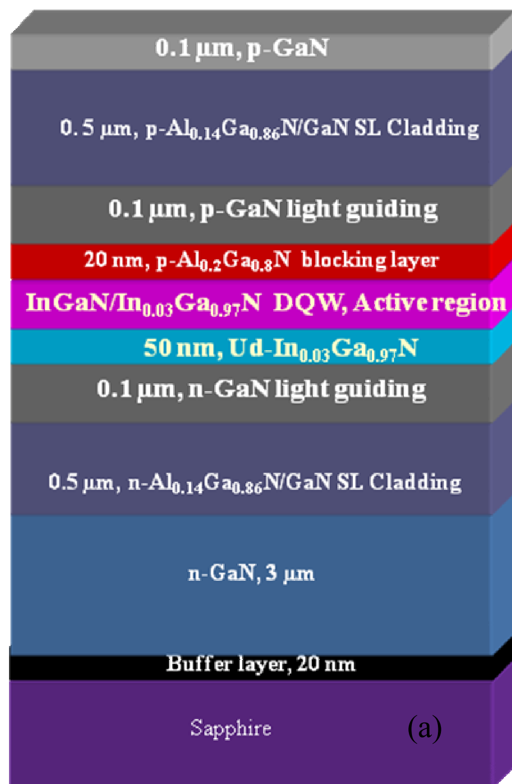

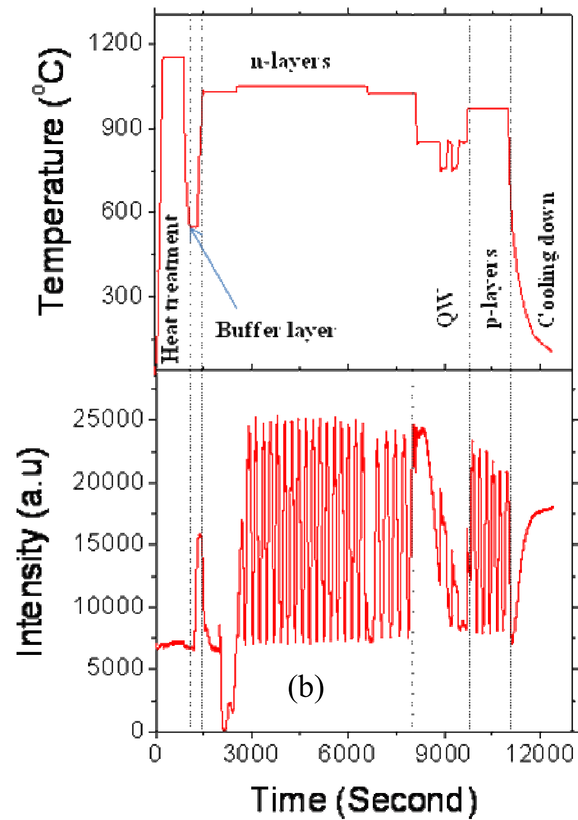

Figure 2.2 (a) Layer structure and (b) *In-situ* temperature profile and interference spectrum during growth for a laser diode structure.

2.3. Material Characterization

2.3.1. Measurement of thermal conductivity of thin films

The thermal conductivity of solids is usually determined by measuring the temperature gradient produced by a steady flow of heat in a one-dimensional geometry. This can be achieved relatively easily on large bulk materials [60]. For thin film materials, the thermal conductivity measurements need some special techniques, such as the AC calorimetric method [60], 3ω method [61, 62], and optical pump-and-probe method [63]. 3ω method is a relatively direct way to measure thermal conductivity, while AC calorimetric and optical pump-and-probe method measures the thermal diffusivity. Thermal conductivity κ is related to the thermal diffusivity D through the following relation,

$$\kappa = \rho C_v D \qquad (2.1)$$

where ρ is material's density and C_v is specific heat. In this section, we discuss only 3ω method.

3ω method was developed by Cahill and coworkers [63-65]. This method normally measures the κ of both substrates and thin films in the cross-plane direction. In the basic method, a line heater is driven by a sinusoidal current source at angular frequency ω, causing a temperature oscillation due to Joule's heating at 2ω. The magnitude of the oscillation is related to the thermal properties of the heater and/or its surrounding environment. This increases the heater resistance at 2ω, leading to a voltage signal at 3ω. A schematic relationship between current, voltage and heat transfer is shown in Fig. 2.3. The 1ω signal, which is much, larger and superimposed with 3ω signal is typically canceled either by nulling a bridge [64-66] or by subtraction with a multiplying digital-to-analog converter [61]. However, when using a lock-in

amplifier with sufficient dynamic reserve, it is simpler to omit this cancellation step [67]. To determine the κ of the thin film deposited on a substrate, a thin metal line (stripe) is deposited onto the film which serves as both a heater and a temperature sensor. Electrical isolation of heater/sensor is required if the thin film is conducting.

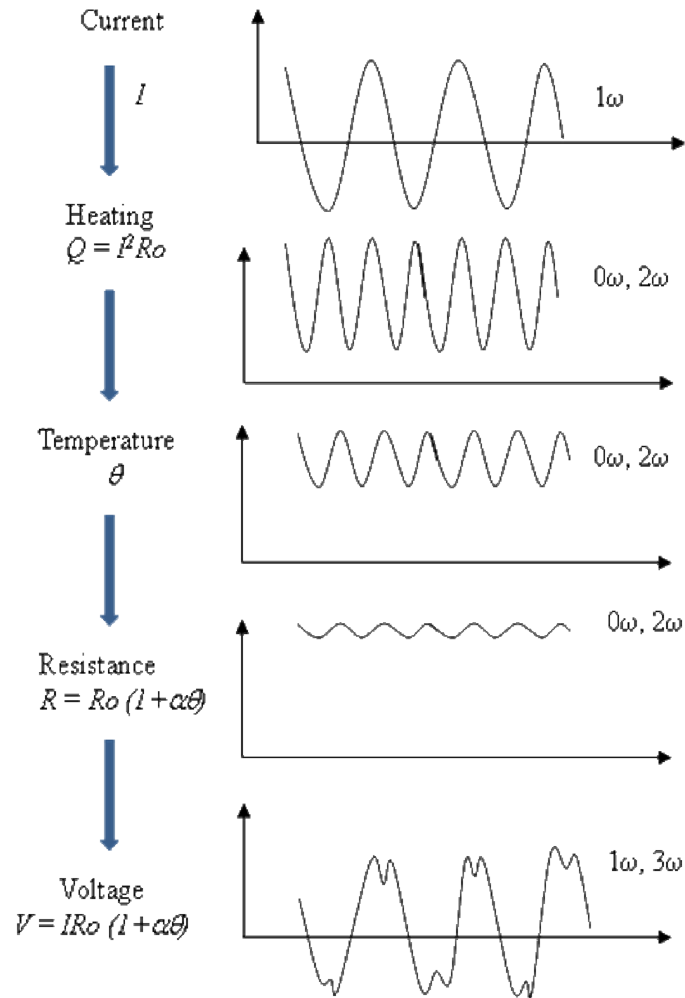

Figure 2.3 A schematic relationship between current, voltage, and thermal transfer.

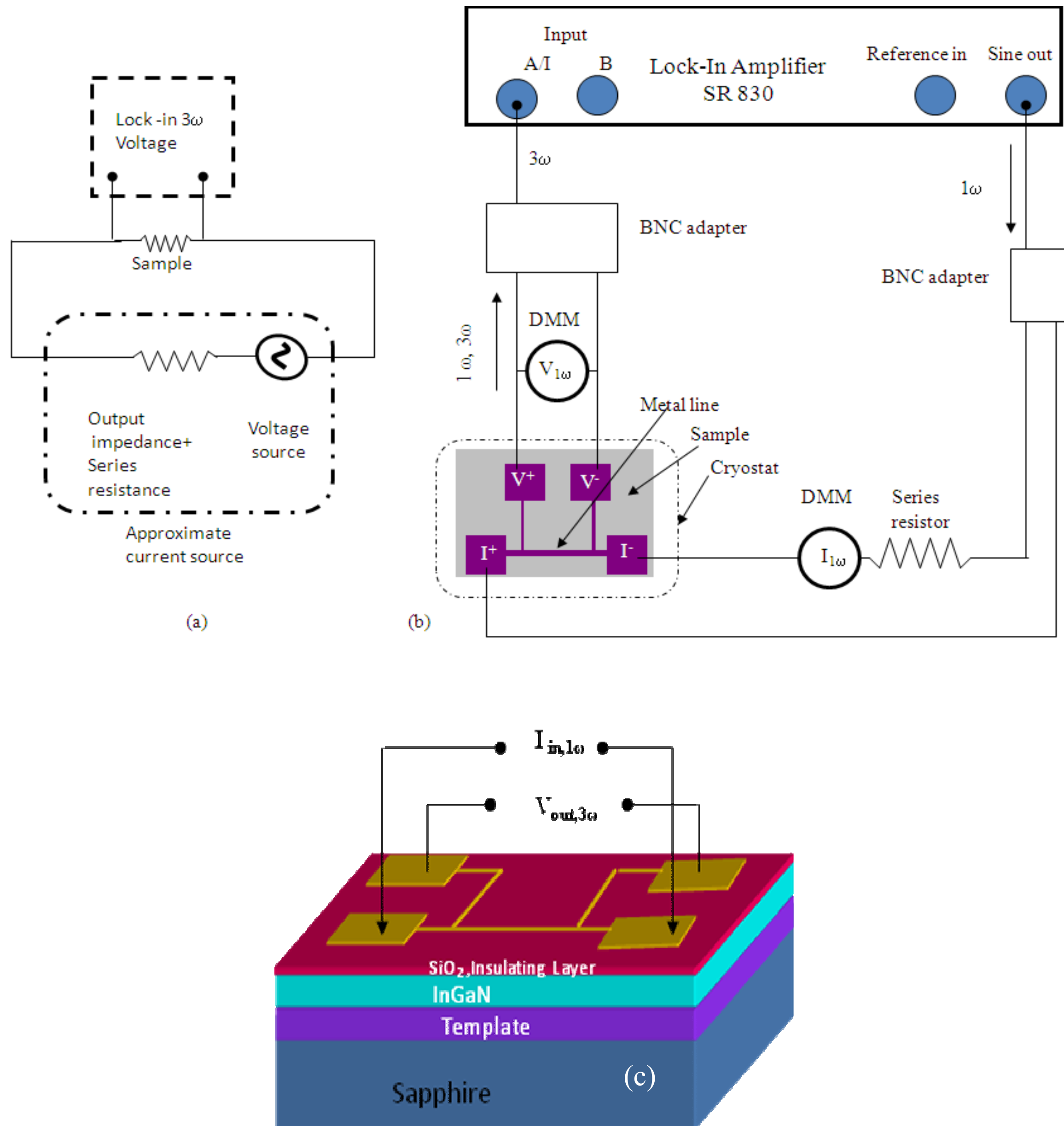

Figure 2.4 (a) Basic electronics of 3ω method, (b) schematic of 3ω experimental set-up, and (c) schematic of metal pattern on the top of the sample. The narrow metal line serves as heater and sensor for the measurement of κ.

A schematic of heater/sensor geometry and experimental set up for 3ω method is shown in Fig 2.4. We used a SR-830 lock-in amplifier to detect the 3ω signal and Keithley digital multimeters (DMM) to measure 1ω voltages and currents. Since we used input 1ω current from the sine-out of lock-in amplifier, there is no need of reference signal. High dynamic reserve assured a good signal-to-noise ratio.

The increase in temperature ΔT can be measured by the following formula [61],

$$\Delta T = \frac{dT}{dR}\frac{R}{V_{1\omega}}V_{3\omega}, \qquad (2.4)$$

where dR/dT is the temperature coefficient of resistance of the metal line, R is the average resistance of the metal line, $V_{1\omega}$ and $V_{3\omega}$ are voltages across the metal line at ω and 3ω, respectively. The κ of the sample (including substrate) can be deduced from the following formula [6],

$$\kappa = \frac{V_{1\omega}^{3}\ln(\frac{f_2}{f_1})}{4\pi l R^{2}(V_{3\omega,1} - V_{3\omega,2}}\frac{dT}{dR}, \qquad (2.5)$$

where, $V_{3\omega,1}$ and $V_{3\omega,2}$ are the in-phase 3ω voltages at frequencies f_1 and f_2 respectively ($\omega = 2\pi f$) and l is the length of the heater between the voltage probes.

To find κ of thin film only, two identical measurements were performed. The total temperature increase ΔT is the sum of the temperature increase across the substrate ΔT_s and the thin film ΔT_f.

$$\Delta T = \Delta T_s + \Delta T_f, \qquad (2.6)$$

$$\Delta T_f = \Delta T - \Delta T_s , \tag{2.7}$$

$$\kappa = \frac{Pt}{lb\Delta T_f}, \tag{2.8}$$

where P is the input power ($P = I_{1\omega}V_{1\omega}$), t is the thickness of the thin film, and b is the half-width of the metal line. A microscopic image of the heater/sensor pattern is shown in Fig. 2.5. The length and width of the metal line are 1500 and 20 μm, respectively. The Fig. 2.6 below shows the temperature rise in sapphire substrate and SiO_2/sapphire samples. Data was taken in a wide range of frequency. The presence of a SiO_2 thin film on the sapphire substrate produces a frequency-independent increase in the in-phase T and no change in the out-of-phase signal. The temperature drop across the SiO_2 film is obtained from the plot. We measured κ of SiO_2 ~1.12 W/m-K which agrees well with the literature values [68].

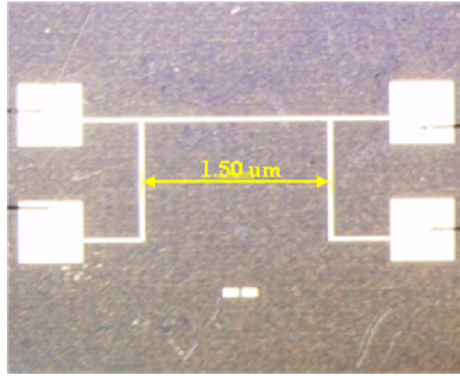

Figure 2.5 An optical microscopic image of the top surface of the sample deposited with heater/ sensor pattern. Length and width of the metal line are 1500 and 20 μm, respectively.

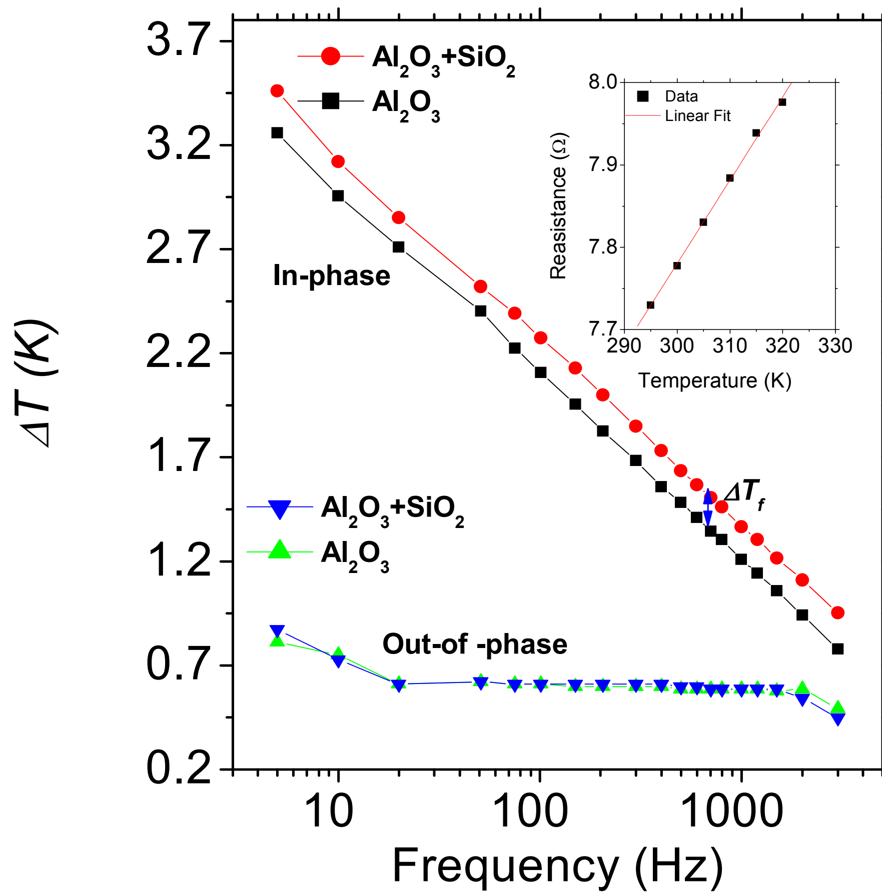

Figure 2.6 Measured in-phase and out-of-phase ΔT (rms) at T = 300 K for a sapphire substrate (Al_2O_3) and for 0.2-μm-thick SiO_2 on a sapphire substrate. Change in resistance of the metal line with temperature is shown in the inset.

2.3.2. Hall-effect measurement

The Hall-effect measurement is a very important technique for characterizing the transport properties of semiconductor materials. It measures resistivity (conductivity), carrier concentration, carrier type, and carrier mobility simultaneously. The Hall-effect occurs when an electromagnetic field is applied across a biased conductor, which produces a potential difference in the plane perpendicular to the magnetic field. Hall-effect measurements in this wok were

performed by Van der Pauw technique. A common configuration for such a measurement has four ohmic contacts at the four corners of a roughly square sample. However, this technique is also applicable for an arbitrarily shaped sample as long as the thickness of the sample is known and uniform, the contact areas are small, and the contacts are all on the perimeter of the sample. Ohmic contacts can be formed by either Indium dots or multilayers of metals, such as Ti/Al/Ni/Au for n-type and Ni/Au for p-type, deposited by e-beam evaporator. Metal contacts need to anneal in suitable conditions. According to van der Pauw's theorem, the resistivity is given by [69],

$$\rho = 1.1331\left(\frac{t}{I}\right)\left(\frac{f_1 \Delta V_1 + f_2 \Delta V_2}{2}\right) \tag{2.9}$$

where t is the thickness of the film, I is the applied current, ΔV_i (I = 1, 2) is the voltage drop across the sample in various configurations, and f_1 and f_2 are the geometrical factors (that are unity for perfect squares). Similarly, the relationship of the mobility μ to the magnetic field B is given by [69],

$$\mu = 2.5x10^7\left(\frac{t}{IB\rho}\right)\left(\frac{\Delta V_3 - \Delta V_4}{2}\right) \tag{2.10}$$

and carrier concentrations are given by,

$$n = -\frac{1}{\rho q \mu} \; and \quad p = \frac{1}{\rho q \mu} \tag{2.11}$$

A schematic of Hall-effect measurement system used for this work is shown in Fig. 2.6. Hall mobility, resistivity, and carrier concentration measurements were performed by a Hall-effect switching card (Keithley Model 7065) [69]. A current source (Keithley model 220) with a

range from 0.1 pA to 101 mA and 10^{14} Ω output resistance provides a current for the sample. A picoammeter (Keithley model 485) and a digital multimeter (Keithley model 196) were used to measure the current and Hall voltage, respectively. The system has an electromagnet (Alpha Scientific, Inc.) controlled through a DIO-200 controller (ERBTEC Engineering, Inc.) with a magnetic field of 0.528 Tesla.

For variable temperature Hall measurements, the system is coupled with a Janis 10 K closed-cycle-refrigeration system (Model CCS 400H/204) and a SHI APD coldhead (Model DE 204 SLFF). A SHI APD (Model HC-4MK2-1) helium compressor is connected to the system to exchange the heat. Temperatures can be varied from from 10 K to 900 K.

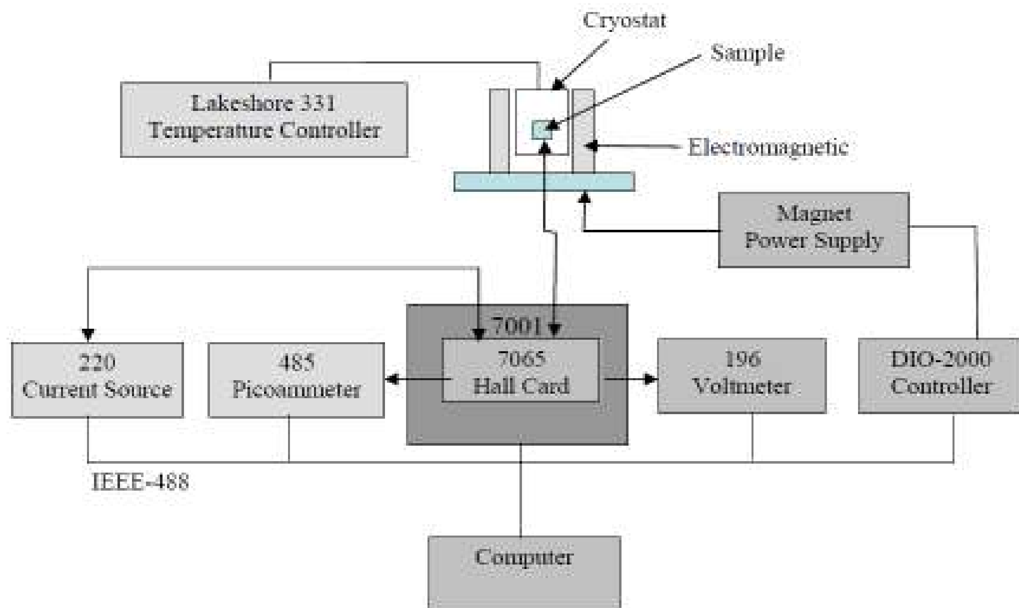

Figure 2.7 Schematic diagram of Hall-effect measurement set up

2.3.3. X-ray diffraction

X-ray diffraction (XRD) is an essential tool for studying microstructures and defects in materials. In this work, the prime purpose of XRD measurement was to determine the lattice constants, alloys composition, and crystalline quality of the nitride thin films. XRD is a fast and non-destructive measurement technique, so it quickly feedbacks the information needed for the optimization of growth conditions and was performed routinely. Additionally, information about the interface quality, tilt, twist stress, and dislocation density can also be examined by XRD.

When X-rays scatter with atoms in adjacent crystal planes at a specific angle, the scattered X-rays interfere constructively. This angle is called as Bragg angle (θ_B) and the Bragg condition is given by,

$$n\lambda = 2d_{hkl}\,Sin\theta_B \qquad (2.12)$$

where λ is the x-ray wavelength, d_{hkl} is the lattice plane spacing, *hkl* are miller indices, and *n* is the order of the reflection. For hexagonal system d_{hkl} is related with c and *a* lattice constants by the formula,

$$\frac{1}{d_{hkl}^2} = \frac{4}{3}\left(\frac{h^2 + hk + k^2}{a^2}\right) + \frac{l^2}{c^2}, \qquad (2.13)$$

A Rigaku single crystal RINT2000V/PC series XRD system was employed for this work and is shown in Fig. 2.8 (Top). X-rays are produced from a sealed-off Cu filament with the characteristic wavelengths at Cu $K_{\alpha 1}$ = 0.154056 nm and Cu $K_{\alpha 2}$ = 0.154439 nm. The peaks due to Cu $K_{\alpha 2}$ are eliminated by software application.

For III-nitrides, we routinely performed XRD of (002) and (102) planes in ω-2θ and ω-scan modes. ω-2θ scan gives lattice parameters or alloy composition and stress or stain in the films while the FWHM of ω scan curves (rocking curves) dictates the crystalline quality of the film. To quantify the dislocation density of edge and screw types, a series of rocking curves of both symmetric and asymmetric planes have to be taken (Chapter 3). XRD (002) and (102) rocking curves of one of the best AlN epilayers grown on Al_2O_3 substrate is shown in Fig. 2.8 (Bottom).

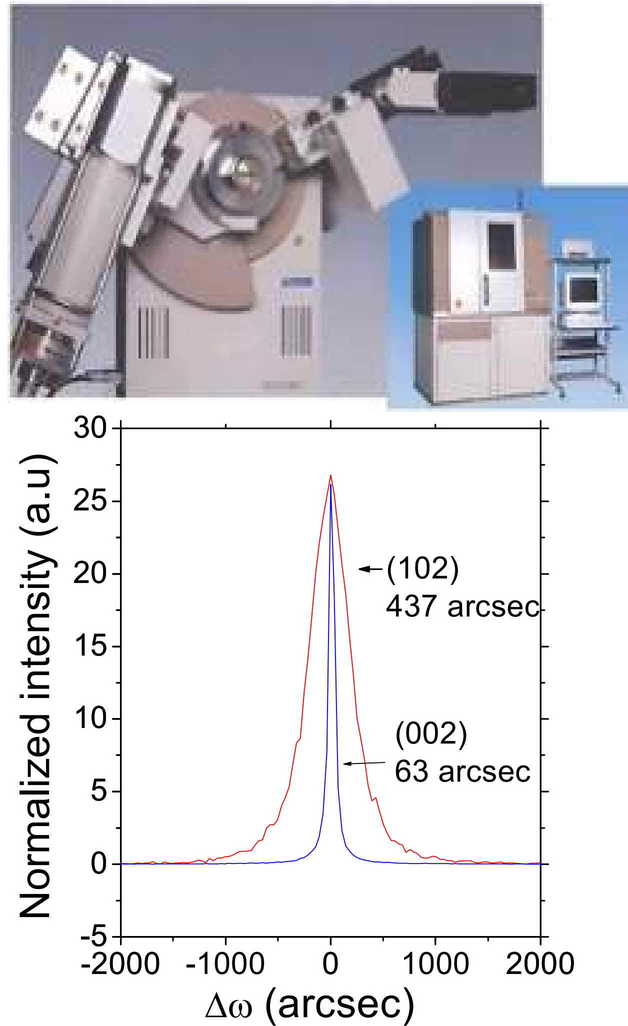

Figure 2. 8 (Top) A picture of XRD systems and (Bottom) (002) and (102) rocking curves of AlN/Al_2O_3.

2.3.4. Atomic force microscopy

The surface morphologies of InGaN alloys were characterized by atomic force microscopy (AFM). AFM makes use of a microscopic metal or semiconductor tip to probe the surface features of a film such as surface roughness, growth modes (2D or 3D), defects that terminate on the surface etc. at atomic scale resolution. The principle of operation is based on the measurement of the deflection of the tip and cantilever using reflected laser light and a photodetector. There are three distinct modes that can be used to study the sample surface, which are contact mode, non-contact mode, and tapping mode. We normally scan the samples in contact mode in which the tip is simply dragged across the surface. Quesant Q-scope 250 AFM system as shown in Fig. 2.9 (Left) was used in this work. A typical image of an $In_{0.45}Ga_{0.55}N$ alloy taken by this AFM is shown in Fig. 2.9 (Right).

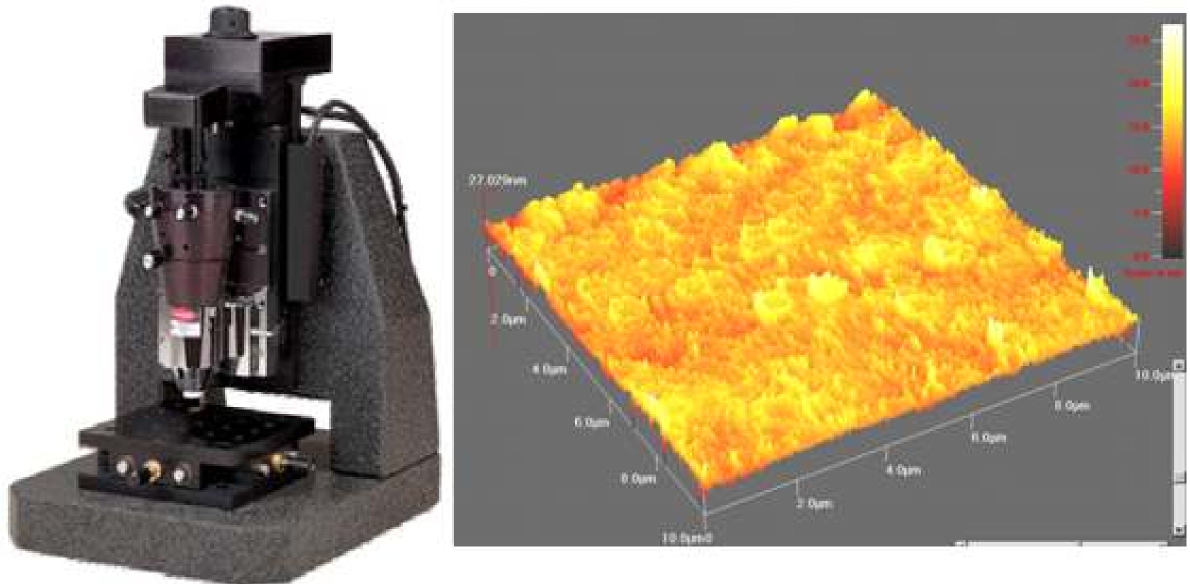

Figure 2.9 (Left) AFM System (Q-Scope 250 model from Quesant Co.), (Right) An AFM image (size: 10 µm x 10 µm) of $In_{0.45}Ga_{0.55}N$ alloy. Surface roughness is ~ 1.8 nm.

2.3.5. Other characterization tools

Besides 3ω, Hall, XRD, and AFM, other characterization tools were also employed in this work. A **Seebeck coefficient** measurement system was set up for thermoelectric characterization of InGaN alloys. A traditional temperature gradient method was employed to measure the Seebeck voltage. The experimental method is briefly described in chapter 4.

Photoluminanace (PL) measurements were performed by a specially designed deep UV laser spectroscopy system. This system basically consists of a frequency quadrupled Ti:sapphire laser and a streak camera, providing an excitation power of about 3 mW at 197 nm with a time-resolution of 2 ps. The detection wavelength range spans from the IR (1.7 μm) to the deep UV (down to 200 nm).

Electroluminescence (EL) measurements are an indispensable technique to characterize the spectral properties of the optical devices. In an LED, EL is the process of radiative recombination resulting from excess carrier injection into the *p-n* junction active region. The EL spectroscopy system mainly consists of a power supply, a spectrometer and a signal acquisition unit. A DC current source is used to supply current to the devices. Our EL detection system consists of an ocean-optics USB 2000-mixed bifurcated fiber (200-800 nm). A Keithley 2430 source meter was used for bias while a Nikon eclipse ME 600 microscope was used for device positioning.

Optical microscope (OM) is a powerful visual inspection tool. It can inspect the surface morphologies such as defects, scratches or cracks, and particles. A Nikon-600 microscope system was used in this work. One can magnify the image up to 1000 time using this microscope.

CHAPTER 3 - Structural and optical properties of AlN epilayers grown by MOCVD

3.1. Introduction

AlN has the widest direct band gap (~6.1 eV) among the III-nitrides and possesses outstanding properties such as high temperature stability, high thermal conductivity, and deep ultraviolet (DUV) transparency. These properties make AlN a good candidate for high power/temperature electronic and optoelectronic device applications such as UV emitters and detectors active in the spectral wavelength region down to 200 nm. AlN epilayers are commonly grown on foreign substrates, such as sapphire and SiC, since high quality AlN bulk wafers are not readily available. Similarly with GaN, AlN thin films grown on sapphires are plagued by a high threading dislocation (TD) density on the order of $\sim10^{9}$–10^{10} cm^{-2} [36, 70, 71]. It is well documented that the presence of high TD density in III-nitrides is a major obstacle for the realization of high performance devices [72, 73]. Thus, approaches for obtaining low defect AlN epilayers as well as effective methods to probe the TD density in AlN are widely sought.

Heteroepitaxial thin films with large lattice mismatch in respect to the substrate commonly exhibit a large number of dislocations. X-ray diffraction (XRD) is a well-established technique and is used extensively to examine the crystallinity and nature of stress in thin films. More recently, it has become a popular method for probing dislocation density in various thin films grown on foreign substrates because it is non-destructive and has no statistical limitation as in the case of transmission electron microscopy (TEM) and atomic force microscopy (AFM), which only cover very small areas. Tilt (out-of plane rotation) and twist (in-plane rotation) spread caused by the mosaicity of the thin film can be measured by XRD to estimate density of

TD [37]. In wurtzite nitrides, tilt spread due to screw dislocations with Burgers vector $\mathbf{b_c}$ = [0001] is directly related to the full-width at half maximum (FWHM) of the ω-scan of symmetric rocking curves obtained from the planes perpendicular to the surface normal. A Williamson-Hall plot of the rocking curves using integral breadth is generally used to determine the tilt angle [38]. Twist spreading connected with the density of edge dislocation with Burgers vector $\mathbf{b_a}$ = $\frac{1}{3}[11\bar{2}0]$ is rather difficult to measure by XRD. There are a number of ways of measuring the twist angle, including (i) a χ-scan of a reflecting plane perpendicular to (001) [such as $(1\bar{1}00)$] in transmission geometry or a ϕ-scan of the same plane in grazing incidence and (ii) ω-scan of asymmetric reflections measured in a quasi-symmetric configuration (skew geometry) [39, 40]. A four-circle diffractometer is required [40] to perform the ω-scan of asymmetric reflection in the skew geometry configuration since the surface normal has to be tilted with respect to the diffraction plane. A model developed by Srikant *et al* [37] is widely used to determine the twist spread in various mosaic thin films. More recently, Lee *et al.* [36] developed a reciprocal space model which describes the (*hkl*) dependence of the broadened Bragg's spectrum produced by XRD from epilayers with dislocations. This model is found to be quite simple and is pursued in the present work.

3.2. Defects in crystals

Defects in crystals [74] are classified as (a) **point defects-** missing atoms or atoms in irregular places in the lattice e.g. lattice vacancies, substitutional and interstitial impurities, self-interstitials etc, (b) **linear defects-** groups of atoms in irregular positions in 1D e.g. screw and edge dislocations, and (c) **planar defects**- the interfaces between homogeneous regions of the

material e.g. grain boundaries, stacking faults, and external surfaces. In this section, the linear defects will be discussed briefly.

Line defects in crystals are called dislocations. They can be edge dislocations, screw dislocations, and mixed dislocations (combination of edge and screw). They can be looked at as an extra partial line or plane of atoms. The number of dislocations per unit volume is the dislocation density. In a plane, they are measured per unit area.

Edge dislocations have an extra half-plane of atoms somewhere in the lattice. As shown in Fig. 3.1 [75] below, the dislocation moves a small amount at a time. The dislocation in the top half of the crystal is slipping one plane at a time as it moves to the right from its position in image (a) to image (b) and finally to image (c). The dislocation line, in this case, is parallel to the stress.

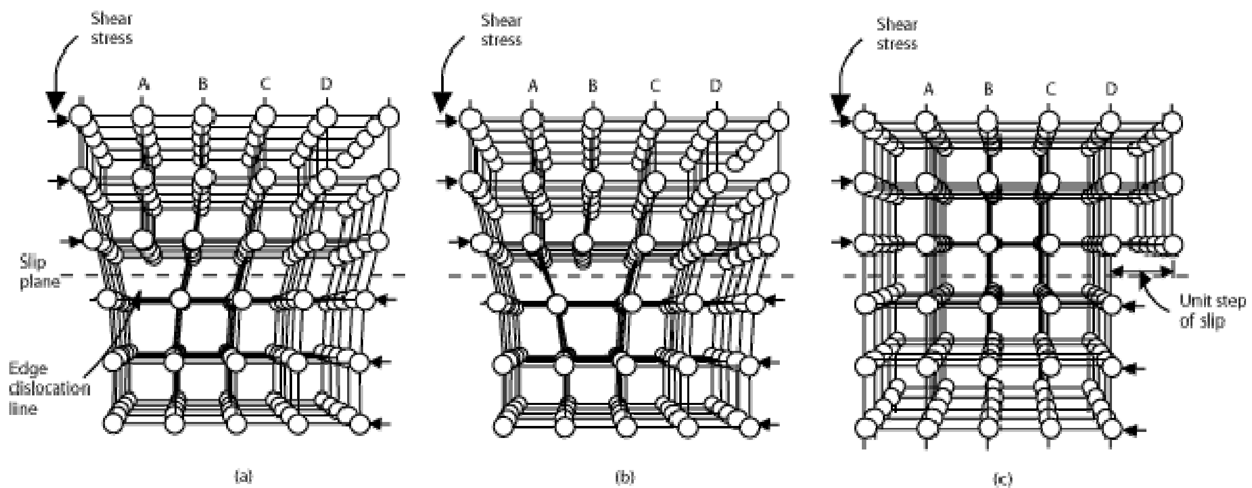

Figure 3.1 Motion of an edge dislocation line under the shear stress [75].

The screw dislocation is slightly more difficult to visualize. The motion of a screw dislocation is also a result of shear stress, but the movement of defect line is perpendicular to the direction of the stress and the displacement of atoms, rather than parallel as shown in Fig. 3.2.

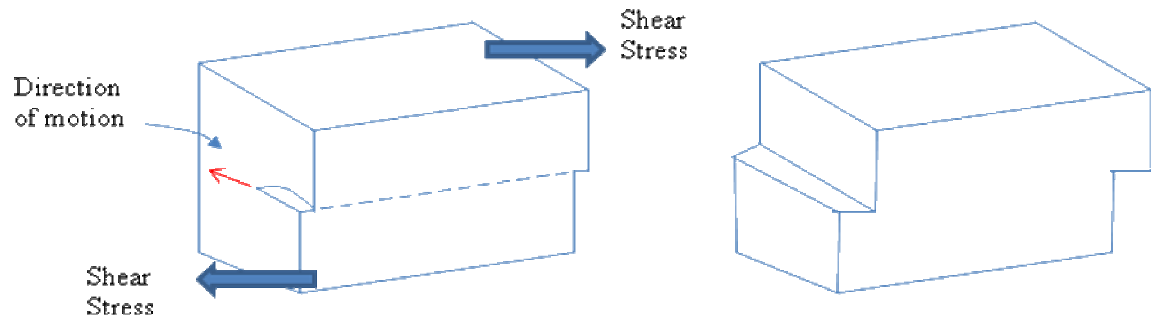

Figure 3.2 Motion of a screw dislocation under the shear stress.

For mixed dislocations, direction of motion is in between parallel and perpendicular to the applied shear stress.

3.3. Burger vectors

The size and the direction of the lattice distortions caused by dislocations are described by Burgers vector **b**. To find **b**, we should make a circuit from atom to atom counting the same number of atomic distances in each direction as shown in Fig 3.3. If the circuit encloses a dislocation, it will not close. The vector that closes the loop is **b**.

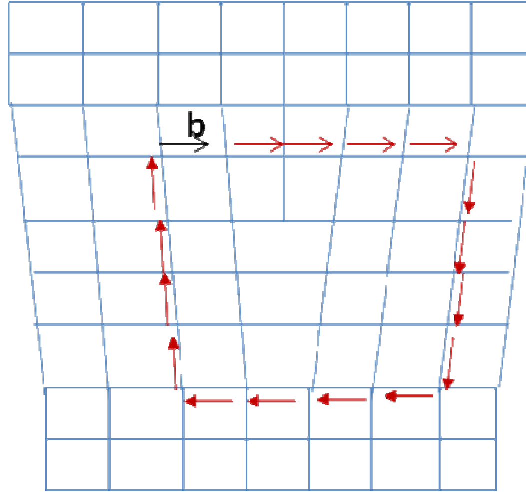

Figure 3.3. Schematic of finding the Burger vector **b**.

3.4. Epilayer thickness dependence of optoelectronic and structural properties and of AlN

AlN epilayers are commonly grown on foreign substrates, such as sapphire and SiC, since high quality AlN bulk wafers are not readily available. Similar with GaN, AlN thin films grown on sapphire substrates are plagued by high TDs as mention above. Presence of high TD density in III-nitrides is a major obstacle for the realization of high performance devices. Thus, approaches for obtaining low defect AlN epilayers as well as effective methods to probe the TD density in AlN are widely sought.

Un-doped AlN epilayers were grown on *c*-plane sapphire by MOCVD. The sources of Al and N were trimethylaluminum (TMAl) and blue ammonia, respectively. We employed DUV PL spectroscopy to investigate the optical properties of AlN epilayers. Metal-semiconductor-metal (MSM) photodetectors were fabricated by depositing Pt (10 nm) Schottky contacts on AlN epilayers. The fabrication procedure has been outlined in a previous paper [76]. We used XRD measurements to evaluate the crystalline quality of AlN epilayers. Tilt (out-of-plane rotation) and

twist (in-plane rotation) spreads caused by the mosaicity of the thin film were measured and utilized to estimate the density of TDs [36, 37-40].

Rocking curves of ω scans of the (002) and (102) reflections were measured and the representative results for a 4 μm AlN epilayer are illustrated in the inset of Fig. 3.4. The main plot of Fig. 3.4 shows the FWHM of rocking curves of ω scans of the (002) and (102) reflections as functions of AlN epilayer thickness *t*. The FWHM of the (102) rocking curve sharply decreases with increasing *t*, while that of the (002) rocking curve moderately decreases with increasing *t*. The FWHMs of the (002) and (102) rocking curves as small as 63 and 437 arc sec, respectively, have been measured for the 4 μm epilayer, which are among the smallest values reported for AlN epilayers grown on sapphire [77].

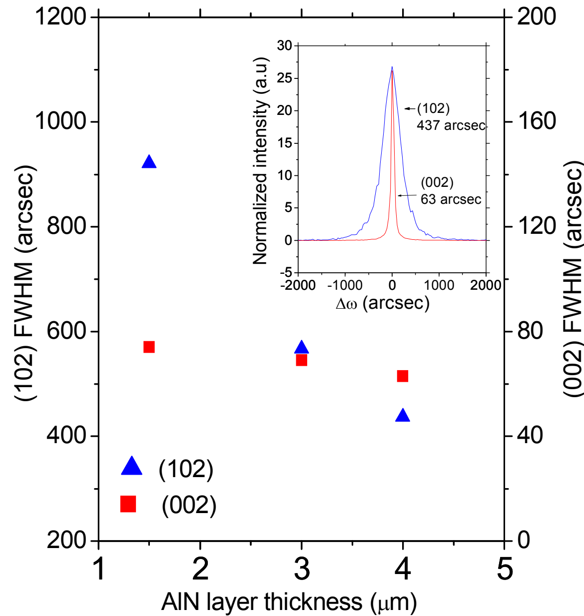

Figure 3.4 Epilayer thickness dependence of FWHM of (002) and (102) rocking curves of undoped AlN epilayers. XRD rocking curves of (002) and (102) planes for a 4 μm AlN epilayer are shown in the inset.

Rocking curves of ω scans of the (002), (004), and (006) reflections for the 4 μm AlN epilayer are shown in Fig. 3.5 and the FWHMs of the (002), (004), and (006) reflections are 63, 72, and 122 arcsec, respectively. We used the FWHM of the (002) reflection to estimate the tilt angle β_{tilt} which was found to be 0.0175°. The density of screw TDs N_{screw} is then estimated using the classical formula [78],

$$N_{Screw} = \beta_{tilt}{}^2 / 4.35 \boldsymbol{b}_c^2, \quad (3.1)$$

where $\mathbf{b}_c$ is the Burgers vector of c-type TDs ($|b_c|$=0.4982 nm). N_{screw} for this film is estimated to be ~5×10^6 cm^{-2}, which represents one of the lowest reported values for AlN epilayers grown on sapphire.

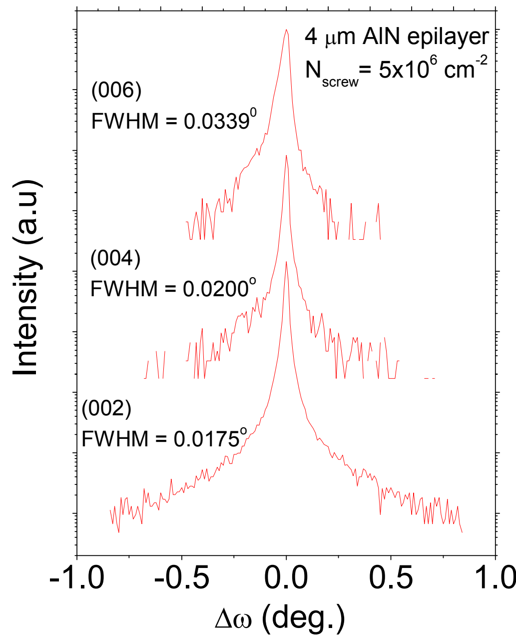

Figure 3.5 Rocking curves of (00l) planes obtained from a 4 μm thick AlN epilayer in symmetric diffraction geometry.

The twist angle was estimated using the method outlined previously by Lee *et al.* [36],

$$\beta = \sqrt{(\beta_{tilt}\, cos\chi)^2 + (\beta_{twist}\, sin\chi)^2}, \tag{3.2}$$

where β_{tilt} and β_{twist} are tilt and twist spreads, respectively, and χ is the angle between the reciprocal lattice vector (K_{hkl}) and the (001) surface normal. The density of edge TDs N_{edge} is then calculated by the classical formula [78],

$$N_{edge} = {\beta_{twist}}^2 / 4.35\boldsymbol{b}_a^2, \tag{3.3}$$

where $\mathbf{b}_a$ is the Burgers vector of *a*-type TDs ($|b_a|$=0.3112 nm). The validity of Eq. (3.3) has already been proven by various authors by comparing the XRD results with those from TEM and etch pit density counting using AFM or SEM in GaN [36, 38, 79]. N_{edge} was calculated to be ~2.5×10^9 cm^{-2} in the 4 μm thick AlN epilayer which is about three orders higher than N_{screw}. The sharp decrease of N_{edge} with decreasing epilayer thickness indicated by the FWHM of the (102) rocking curve could be due to the termination of an edge type dislocation by forming a loop with similar neighboring dislocations having opposite **b** as the epilayer thickness increases. The results indicate that AlN epilayer acts as an effective dislocation filter.

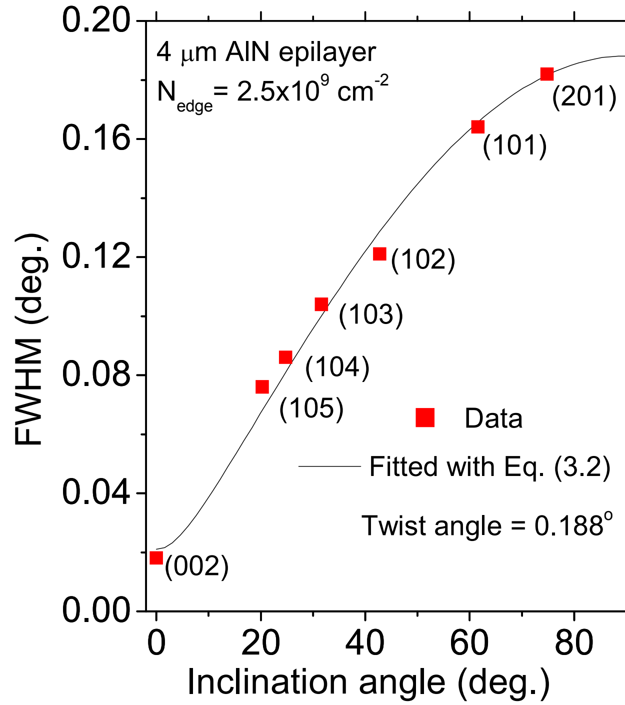

Figure 3.6 Plot of FWHM of (*hkl*) planes as a function of the lattice plane inclination angle (χ), according to Ref. 1 (solid points) and fitted with Eq. (3.2).

In spite of the recognition of its outstanding physical properties, so far there have been only a few demonstrations of AlN as an active DUV optoelectronic device material [76, 80] due to the lack of high quality AlN epilayers in the past. The 1.5 and 4 μm AlN epilayers were utilized to fabricate MSM photodetectors with the same active device area. The fabricated AlN MSM photodetectors exhibit a peak responsity at 200 nm, a sharp cutoff wavelength around 207 nm, and more than four orders of magnitude DUV to UV/visible rejection ratio at the applied bias voltages below 150 V [76].

Figure 3.7 shows the dark *I-V* characteristics of the fabricated AlN MSM photodetectors measured at bias voltages, $V_b > 150$ V. It can be seen that the dark current is drastically reduced in the detector with a thick (4 μm) AlN active epilayer. The results suggest that the magnitude of the dark current is directly correlated with the density of *TDs* and DUV photodetectors with improved sensitivity being obtainable by depositing device structures on thick AlN epilayer templates.

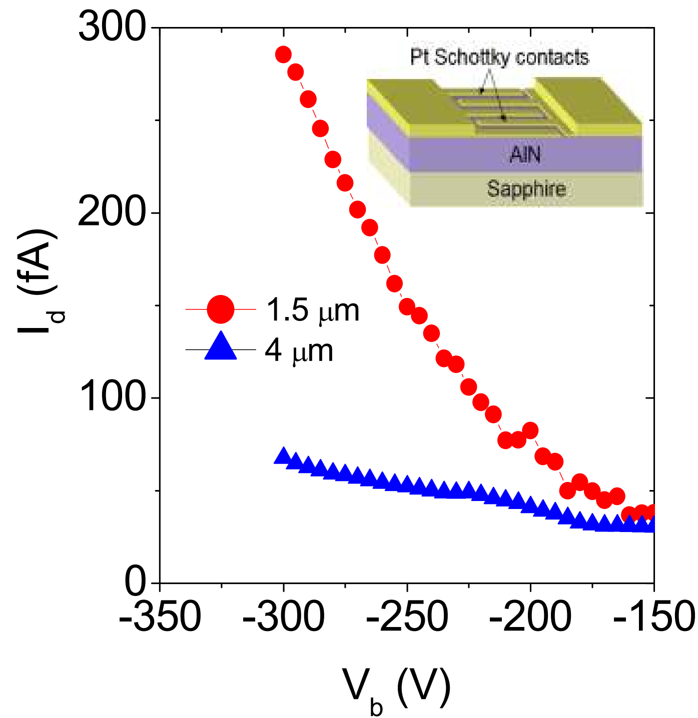

Figure 3.7 Dark *I-V* characteristics of AlN MSM photodetectors fabricated from 1.5 and 4 μm thick AlN epilayers measured at bias voltages above 150 V. The inset shows the schematic of the device layout (device size = 80×80 μm^2 and finger width/spacing = 2/4 μm).

The PL emission properties of these AlN epilayers have also been investigated and the PL spectra are displayed in Fig. 3.8 (a), which shows that the emission intensity of the free exciton (FX) recombination (I_{FX}) at 5.98 eV [2, 81] increases and that of the deep level impurity line

(I_{imp}) around 3.8 eV significantly decreases with an increase of the AlN epilayer thickness. More specifically, we noticed from Fig. 3.8 (b) that the intensity ratio of the FX emission to the deep level impurity emission, I_{FX}/I_{imp}, increases, while the FWHM of the FX transition decreases almost linearly with an increase of the AlN epilayer thickness. Since the optical absorption layer in this wavelength region is on the order of 0.1 μm, we attribute the increase of the FX emission efficiency and the reduction in FWHM of FX transition to the reduced TD density. The bottom portion of Fig. 3.8 (b) shows that the FX emission peak position blueshifts with an increase in AlN epilayer thickness, which suggests that the thicker films are more compressively strained.

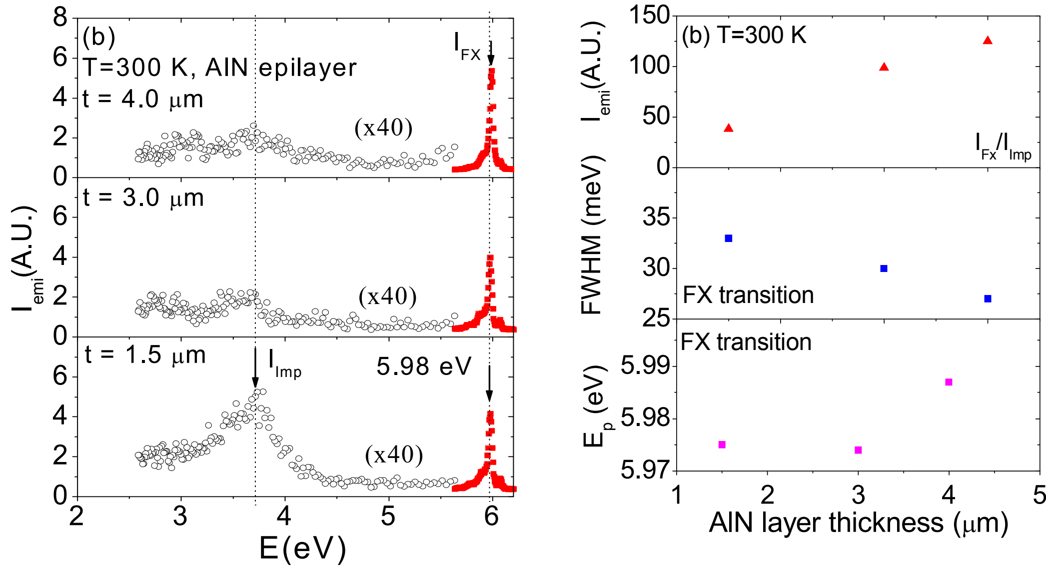

Figure 3.8 (a) PL emission spectra of AlN of different epilayer thicknesses t, (b) Epilayer thickness dependence of the ratio of the free exciton (FX) emission to the deep level impurity emission (I_{FX}/I_{imp}), the FWHM of the FX transition, and the peak position of the FX transition.

In summary, structural and optoelectronic properties of undoped AlN epilayers have been studied. For a thick AlN epilayer (~ 4 μm), the FWHM of the rocking curves of the (002) and

(102) reflections were as small as 63 and 437 arcsec, respectively, from which N_{screw} and N_{edge} for this film were estimated to be ~5×10^{6} and ~2.5×10^{9} cm^{-2}, respectively. 200 nm DUV photodetectors with outstanding characteristics were fabricated from the AlN MSM structure and it was shown that the dark current was significantly decreased in photodectectors with thick AlN epilayers. Furthermore, PL measurements revealed that the band edge emission intensity (defect related emission intensity) increases (decreases) with increasing AlN epilayer thickness. The results suggested that one effective way for attaining DUV optoelectronic devices with improved performance is to increase the thickness of the AlN epilayer template, which results in the reduction of TD density.

3.5. Structural properties of silicon doped AlN

Silicon has been shown to be an n-type dopant for AlN [80, 82] just as it is in GaN. Dopant incorporation causes crystal imperfections which can affect the structural and optical properties of the thin film. There are very few reports on the structural properties of Si-doped AlN thin films in the literature [83, 84]. The effect of silicon on such properties has not yet been fully understood. By studying the effects of doping on structural properties such as dislocations, stress, and strain conditions, we expect to open a pathway for improvement in the crystalline, electric, and optical qualities of AlN thin films.

It has been reported that Si-doping in GaN has a strong influence on structural defects. However, most of the results are still controversial and not fully understood [85-92]. Alam *et al.* [85] observed, by TEM, higher TD density at lower doping levels, N_{Si} (~ 10^{17} cm^{-3}) than at moderate levels N_{Si} (10^{18} cm^{-3}). This contradicts the result reported by Ruvimov *et al*. [86] who found that doping of GaN/a-plane sapphire by silicon to a concentration of $3\text{x}10^{18}$ cm^{-3} can

improve the layer quality by reducing N_{TD} almost one order of magnitude compared to an undoped layer. Lee *et al.* [87] found that as N_{Si} increases, the FWHM of symmetric rocking curves is also increased, which was attributed to the fact that doping of Si increases the density of misfit dislocation in the vicinity of an interface. Contreras *et al.* [91] observed, by TEM, that silicon delta doping reduces the screw component of TDs by 70%. They suggested that the reduction is associated with the bending of screw dislocations and pairing with equivalent neighboring dislocations with the opposite Burgers vector. Some other authors observed [87-90], in Si-doped GaN, that silicon incorporation induced a relaxation of compressive stress in the films with low N_{Si}, while the films were found to be under tensile stress at higher N_{Si}.

Un-doped and silicon doped AlN epilayers were grown on c-plane sapphire by MOCVD with a thin low temperature buffer layer. Trimethylaluminum (TMAl), blue ammonia (NH_3), and silane (SiH_4) were used as sources for Al, N, and Si, respectively. Silicon doping concentrations were varied from $2x10^{17}$ cm^{-3} to $1x10^{19}$ cm^{-3}. The thickness and growth conditions of all samples were kept the same in order to avoid errors arising due to different growth parameters. Measurement method is the same as that described in the above section.

The radial scans of (002) planes for un-doped and Si-doped AlN epilayers are shown in Fig. 3.9. Regardless of N_{Si}, all curves have retained their symmetric shape. This is attributed to the fact that there is no gradient of stress normal to the surface. As N_{Si} increases, the 2θ position shifts to a higher angle corresponding to a smaller *c* lattice constant. In contrast to this, at higher N_{Si} (> $2x10^{18}$ cm^{-3}) the shift of the 2θ position has been observed to be in the reverse direction.

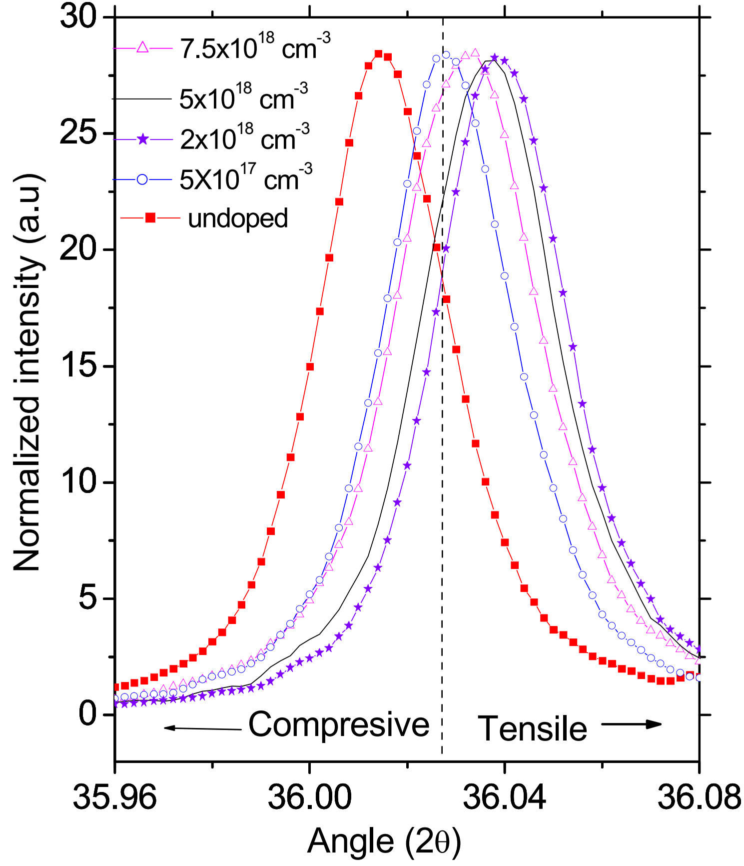

Figure 3.9 Angular shift (2θ) of (002) reflection in radial scan mode in an un-doped and Si-doped AlN epilayers.

We used a standard, perfectly flat sample holder to perform a symmetric scan so the possibility of shifting the 2θ angle due to misalignment of the sample is very small. Lattice parameters were calculated from the peak position of the ω-2θ scan of the (105) and (002) planes using the following formula,

$$\frac{1}{d_{hkl}^2} = \frac{4}{3}\left(\frac{h^2 + hk + k^2}{a^2}\right) + \frac{l^2}{c^2}, \tag{3.4}$$

where h, k, l are miller indices, and c and d are lattice constants for the (002) and (hkl) planes, respectively. The in-plane stress $\sigma_{//}$ can be roughly estimated from the following equation [93],

$$\sigma_{//} = \frac{a - a_o}{a_o}\left(C_{11} + C_{12} - 2\frac{C_{13}^2}{C_{33}}\right), \qquad (3.5)$$

where the C_{ij} are the elastic constants of AlN (C_{11} = 396 GPa, C_{12} = 137 GPa, C_{13} = 108 GPa, C_{33} = 373 GPa) [94] and a_o = 3.112 Å [95] is the lattice constant for strain-free AlN. The structural parameters investigated in this work for undoped and silicon-doped AlN epilayers are listed in Table 1.

N_{Si} (x 10^{18} cm^{-3})	Lattice constant c (Å)	Lattice constant a (Å)	Residual strain $\Delta c/c_0$ (x10^{-4})	In-plane stress ($\sigma_{//}$) (GPa)	Tilt Angle (deg)	Twist angle (deg)	N_{screw} x10^8 cm^{-2}	N_{TD} x10^9 cm^{-2}
Undoped	4.9833	3.1052	2.61	-1.03	0.122	0.275	4.2	5.9
0.5	4.9816	3.1122	0.80	0.03	0.134	0.321	5.1	8.0
2	4.9800	3.1168	4.01	0.73	0.154	0.325	6.7	8.3
5	4.9804	3.1156	3.22	0.55	0.159	0.332	7.1	8.8
7.5	4.9811	3.1145	1.81	0.38	0.172	0.299	8.5	8.4
10	4.9815	3.1133	1.00	0.20	0.179	0.286	9.0	6.8

Table 3.1 Summary of dependence of lattice parameters, state of stress and strain, twist and tilt variance of AlN epilayes on silicon doping concentrations N_{si}. In-plane lattice constant 'a' has been calculated using 'd' values of (002) and (105) lattice planes. Lattice parameters and elastic constants used for stress free AlN were taken from refs. [94] and [95].

Twist and tilt angles were derived according to ref. [36] and the Williamson-Hall plot, respectively. One can observe that the undoped layer is under compressive stress (-1.06 GaP). As N_{Si} increases, relaxation of compressive stress has been observed. The stress changed to tensile when N_{Si} exceeded 5×10^{17} cm^{-3}. The layer was almost fully relaxed at this concentration. Lee *et*

al. [92] argued that the relaxation of the stress arises via Si-induced generation of misfit dislocations. According to Dadgar *et al.*, [90] Si-promoted shrinkage of the lattice planes (correlated with edge-type dislocations) is the origin of tensile stress. The change in stress and lattice parameters of AlN due to silicon incorporation is only moderate in our samples compared to those of MBE-grown Si-doped AlN as reported by Hermann *et al.* [83]. The residual strain ($\Delta c/c_o$) was estimated in all layers and is on the order of (0.4-4.0) x 10^{-4}).

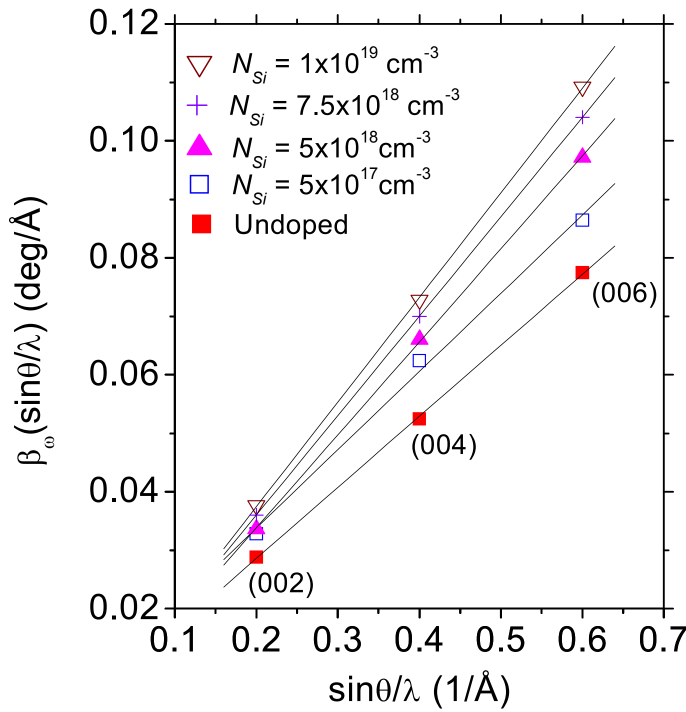

Figure 3.10 The Williamson-Hall plot (W-H plot) using integral width of the (002), (004), and (006) rocking curves for an un-doped and Si-doped AlN epilayers.

A systematic study of the dependence of symmetric and asymmetric FWHM rocking curves on N_{Si} in Si-doped AlN epilayes has been performed in order to determine the twist and tilt angles with respect to N_{Si}. Figure 3.10 shows the Williamson-Hall plots for an undoped AlN epilayer and four Si-doped AlN epilayers. The slope of the line is observed to increase with

increasing N_{Si}, which suggests that tilt angle also increases gradually as N_{Si} increases. This is in good agreement with the result reported for GaN:Si [84,87,92]. Broadening of the symmetric rocking curves can be caused by either compressive or tensile stress. If broadening is observed when stress is relaxed, there could be another mechanism such as generating dislocations. N_{screw} is estimated using Eq. (3.1).

Figure 3.11 plots the FWHM rocking curves of the symmetric (002) and several asymmetric reflecting planes with respect to inclination angle (χ) and fitted by Eq. (3.2). As N_{Si} increases from 5x 10^{17} to 5x10^{18} cm^{-3}, a gradual increase in the FWHMs for all asymmetric rocking curves has been observed. However, the FWHMs begin to decrease as N_{Si} increases further. Twist angles have been obtained by fitting the data with Eq. (3.2). These fitted angles are then used to estimate N_{edge} using Eq. (3.3). The change in twist angle with respect to N_{Si} up to 5x 10^{18} cm^{-3} is relatively small. The tensile stress in the films is most likely caused by the formation of edge dislocation which manifests itself as an increased FWHM of the asymmetric rocking curves. Note, however, that the effect of Si incorporation on the FWHMs of the asymmetric rocking curves is less pronounced than that on the symmetric rocking curves.

The variation of N_{edge}, together with screw components, N_{screw}, with respect to N_{Si} is shown in Fig. 3.12. We observed that N_{edge} (or the total dislocation density, N_{TD}, (Table 1) because the majority of dislocations are of the edge type) increases with increasing N_{Si} in moderately doped epilayers. For higher N_{Si} we found that N_{edge} decreases but the change is relatively small. This is in agreement with the result reported by Alam *et al*. [24] for GaN:Si. However, we observed that N_{edge} in silicon doped layers is correlated with an accumulation of tensile stress. One can conclude that incorporation of silicon in AlN behaves similarly to that in GaN [89-92].

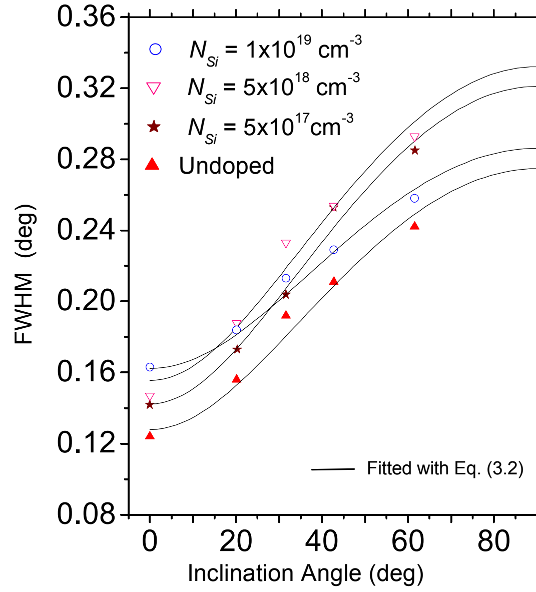

Figure 3.11 FWHM of the rocking curves of the (*hkl*) planes as a function of lattice plane inclination angle (χ) with respect to sample surface for an undoped and several Si doped AlN epilayers and fitted with Eq. (3.2).

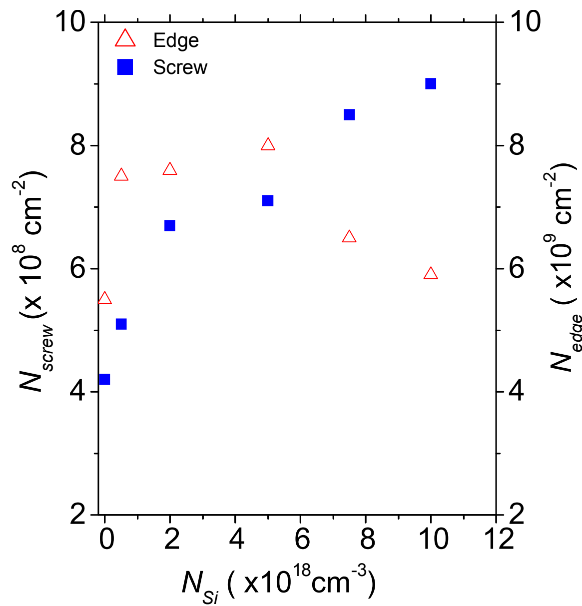

Figure 3.12 Dislocation densities of screw (N_{screw}) and edge (N_{edge}) type, as functions of N_{Si} calculated from Eqs. (3.1) and (3.3).

In summary, the effects of Si-doping on the structural properties of AlN epilayers are studied. Undoped AlN epilayers are found to be under compressive stress that gradually relaxes with increasing doping concentration (for $N_{Si} < 5x10^{17}$ cm^{-3}). Further increase in N_{Si} changes the nature of the stress to tensile. The most significant effect due to Si-doping on the structural properties is the increase of N_{screw}, indicated by the broadening of the symmetric rocking curve at all doping levels. In contrast, the effects of Si-incorporation on the lattice parameters and on N_{edge} (indicated by FWHM of asymmetric rocking curves) are moderate.

3.6. Correlation between biaxial stress and free exciton transition in AlN epilayers

AlN has emerged as an active photonic material for applications in deep ultraviolet (DUV) emitters and detectors because of its large direct bandgap of 6.1 eV [76, 16]. Due to its high thermal conductivity, large piezoelectric field, and low electron affinity, AlN also has applications in stable x-ray production, surface acoustic wave (SAW) devices, and electron emission devices [96-98]. Furthermore, if not properly managed, the stress induced by the thermal expansion coefficient mismatch between AlN and substrate may cause cracks in relatively thick epilayers. Much progress has been made recently for obtaining AlN bulk single crystal substrates [99-101]. The use of an AlN bulk single crystal as a substrate is expected to significantly enhance the overall AlN epilayer quality due to its better lattice constant and thermal expansion coefficient matches to the subsequent epilayers compared to other substrates. There have been significant advances in the epitaxial growth of high quality AlN epilayers [2, 102-110] and AlN based active photonic device structures [76, 80] on sapphire, SiC, Si, and AlN bulk substrates.

A systematic comparative study concerning the basic structural and optical properties of AlN epilayers grown on various substrates is needed because of the increased importance of AlN for various applications and the diverse choices for substrates. However, this has been highly challenging because the growth conditions of AlN epilayers on different substrates have to be independently optimized. In this section, we discuss the epitaxial growth, DUV photoluminescence (PL) and x-ray diffraction (XRD) studies of AlN epilayers grown on sapphire, SiC, Si, and AlN bulk single crystal substrates. The variations of the free exciton emission peak positions and lattice constants with respect to the growth substrate have been probed and analyzed. It was confirmed that AlN epilayers grown on AlN bulk substrates (or homoepilayers) have the same lattice parameters as AlN bulk crystals and are almost strain-free, while AlN heteroepilayers grown on sapphire substrates experience a compressive strain and those grown on SiC and Si substrates undergo a tensile strain. Based on the variations of the free exciton (FX) emission peak position and lattice constant with respect to the growth substrate, a linear relationship between the FX transition and in-plane stress was obtained and a value of 45 meV/GPa for the linear coefficient of the stress-induced bandgap shift in AlN epilayers was deduced.

The 1 μm thick un-doped AlN epilayers were grown on bulk AlN, sapphire (0001), Si (111), and 4*H*-SiC (0001) substrates by MOCVD. The AlN epilayers were grown at 1050 °C on Si and 1300 °C on sapphire, SiC, and AlN substrates. The DUV PL spectroscopy system employed consists of a frequency quadrupled 100 fs Ti:sapphire laser with an average power of 3 mW with excitation photon energy set at 197 nm or 6.28 eV (repetition rate of 76 MHz), and a 1.3 m monochromator [111].

Figure 3.13 shows the low temperature (10 K) PL spectra of AlN epilayers grown on sapphire (AlN/Al_2O_3), SiC (AlN/SiC), Si (AlN/Si), and bulk AlN (AlN/AlN) substrates measured in (a) a broad spectral range from 2.4 to 6.2 eV and (b) in a small spectral range from 5.8 to 6.2 eV. For all samples, the emission intensity of defect/impurity related lines is negligibly small compared to that of the band edge, which indicates that these AlN epilayers are of high purity. The integrated band edge emission intensity ratio is roughly 5:4:3:1 for AlN/AlN, AlN/Al_2O_3, AlN/SiC, and AlN/Si and the line-width of the band-edge emission line is narrowest for the AlN homoepilayer, implying that the homoepilayer possesses the highest crystalline quality as we expected.

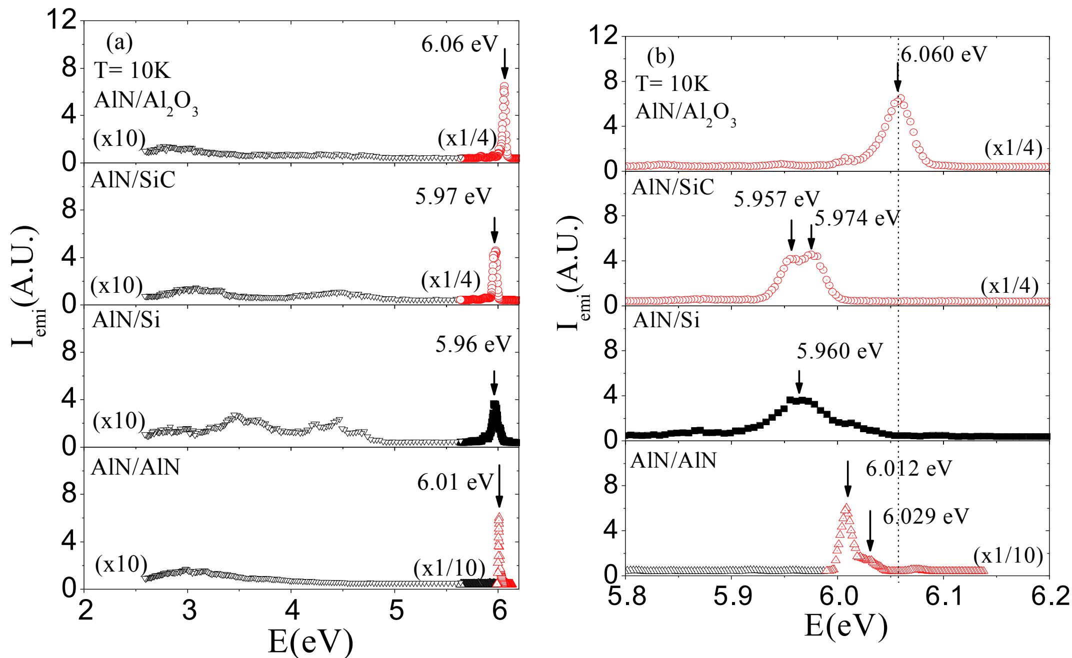

Figure 3.13 10 K PL spectra of AlN/Al_2O_3, AlN/SiC, AlN/Si, and AlN/AlN bulk, measured in (a) a broad spectral range from 2.4 to 6.2 eV and (b) small spectral range from 5.8 to 6.2 eV.

The temperature evolutions of the emission spectra and intensity have been measured for all samples. AlN/Al_2O_3 epilayers exhibit only one dominant emission peak with a position

located at around 6.06 eV at 10 K. As illustrated in Fig. 3.14 (a), the temperature dependence of the emission intensity of this line revealed an activation energy of about 78 meV, which is the measure of the binding energy of the FX in AlN epilayers [2, 104]. Therefore, we assign the 6.06 eV emission line in AlN/Al_2O_3 to the FX transition. On the other hand, AlN/AlN and AlN/SiC epilayers exhibit two emission lines. The higher energy emission line is due to the FX recombination and the lower energy emission peak is due to the donor-bound-exciton recombination (I_2), based on the known value of about 16 meV for the binding energy of the donor-bound excitons in AlN epilayers [81]. Additionally, temperature evolutions of the emission spectra and intensity, one of which is illustrated in Fig. 3.14 (b), reveal an activation energy of about 16.4 meV for the lower energy peak, which agrees very well with the spectral peak separation between the higher and lower energy peaks (6.029–6.012 eV = 17 meV) and further corroborates our assignment of I_2 and FX transitions. The inset of Fig. 3.14 (b) also clearly shows that the I_2 emission intensity decreases with temperature more rapidly than in the FX transition, which is to be expected because the donor bound excitons dissociate into FXs and neutral donors.

Compared to the FX transition in AlN/AlN, the observed energy position of the FX transition is 31 meV higher in AlN/Al_2O_3 due to a compressive strain and is 55 (69 meV) lower in AlN/SiC (AlN/Si) due to a tensile strain. Although the integrated emission intensity is highest in AlN homoepilayers, the dominant transition at low temperatures is I_2 rather than FX, which indicates the presence of a higher unintentional donor impurity concentration in AlN/AlN than in AlN/Al_2O_3. The presence of these impurities may be due to the diffusion of oxygen (Si) atoms from the AlN (SiC) bulk substrate to the subsequent AlN epilayer during the epitaxial growth.

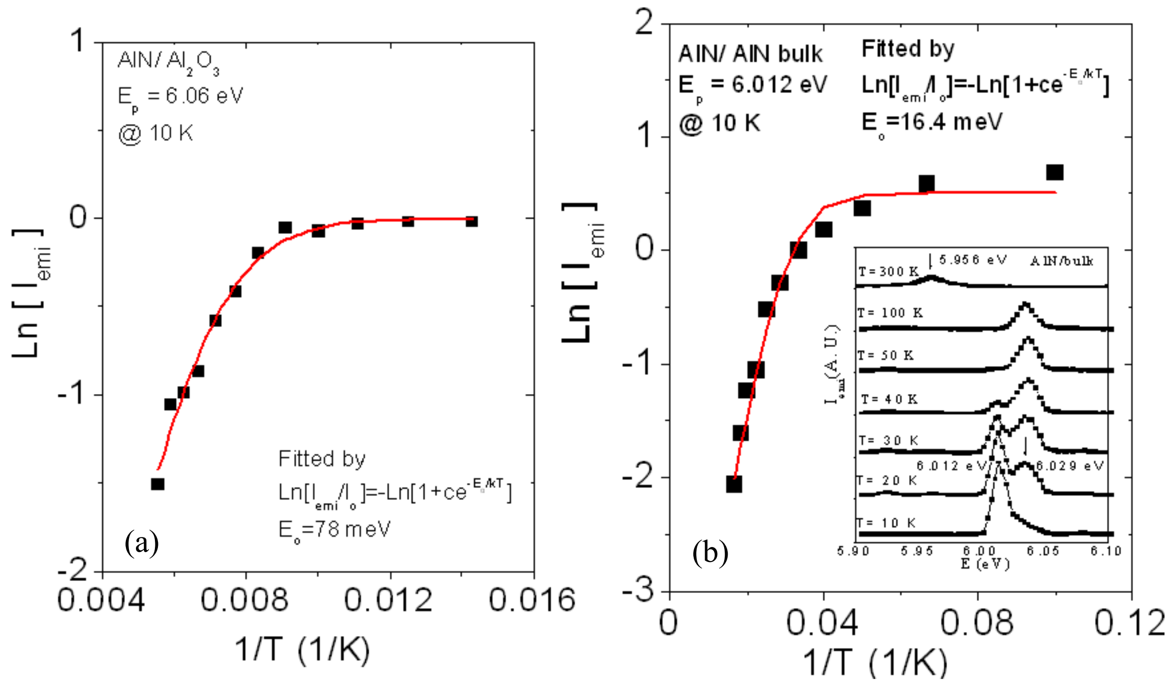

Figure 3.14 The Arrhenius plot of the intensity of the dominant emission line (6.060 eV at 10 K) in AlN/Al_2O_3 epilayers. The measured activation energy is about 78 meV. (b) The Arrhenius plot of the intensity of the lower energy emission line (6.012 eV at 10 K) in AlN/AlN homoepilayers. The measured activation energy is about 16.4 meV. The inset shows the temperature evolution of the band-edge emissions in AlN homoepilayers.

The lattice constants were determined using XRD by measuring the lattice parameters and the diffraction angles (θ) in ω-2θ scans of (002), (102), and (105) reflection planes. An example of such measurements is shown in Fig. 3.15, where ω-2θ scans of the symmetric (002) and asymmetric (102) planes of an AlN homoepilayer and AlN bulk substrate are displayed. The results shown in Fig. 3.15 clearly indicate that the AlN homoepilayer is perfectly lattice matched to the AlN bulk substrate and is almost strain-free. AlN homoepilayers have an in-plane lattice constant of a = 3.112 Å. The lattice constant a increases in AlN/SiC and AlN/Si epilayers due to the presence of a tensile stress, while it decreases in AlN/Al_2O_3 epilayers due to the presence of a

compressive stress. This is consistent with the FX transition peak position shift observed in Fig. 3.13.

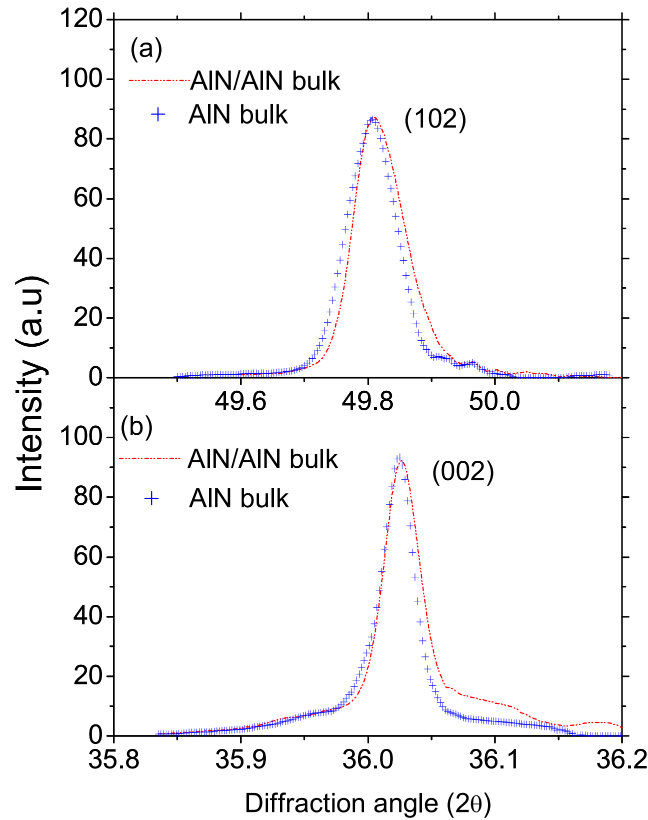

Figure 3.15 ω-2θ scan of (a) asymmetric (102) and (b) symmetric (002) reflection planes for an AlN homoepilayer and AlN bulk substrate.

To see a clearer correlation between the FX transition peak position and the magnitude of the strain in various AlN epilayers, we plot in Fig. 3.16 (a) the variation of the FX transition peak position and in (b) the variation of the in-plane lattice constant (*a*) of AlN epilayer with respect to the growth substrate. Based on the results shown in Fig. 3.15, an AlN homo-epilayer is perfectly lattice matched to the AlN substrate and the FX emission peak position in AlN homoepilayers presents the position of unstrained AlN epilayers. A one-to-one correlation between lattice

constant and FX transition peak position shift with respect to that of the AlN homoepilayer can be clearly identified. Based on the results shown in Fig. 3.16, the linear coefficient of stress-induced bandgap shift in AlN epilayer can be deduced, which is a fundamentally important parameter for the structural design of various devices. The in-plane stress $\sigma_{//}$ was estimated using equation (3.5).

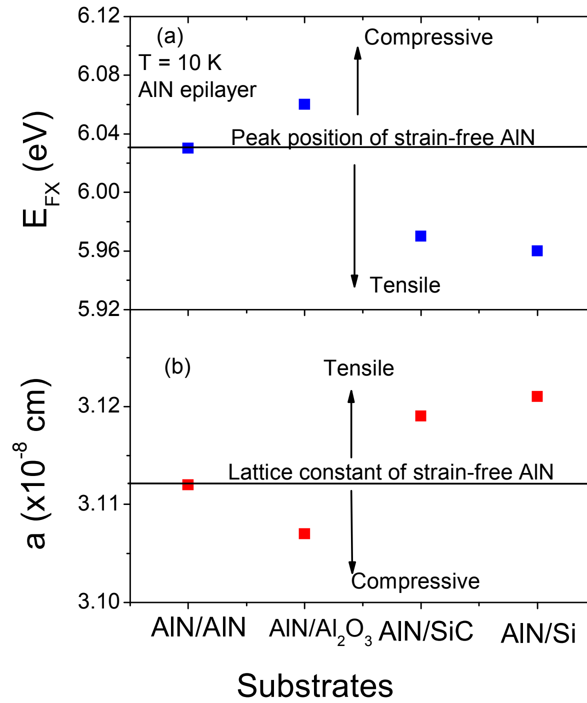

Figure 3.16 (a) Free exciton spectral peak positions (E_P) and (b) in-plane lattice constants a of AlN epilayers grown on different substrates. Stress in AlN/Al_2O_3 is compressive and is tensile in AlN/SiC and AlN/Si epilayers.

The experimental value of the linear coefficient for stress-induced FX transition (or bandgap) shift in AlN epilayers is 45 meV/GaP, which is about 88% higher than that in GaN (24 meV/GPa) [112]. This higher value for the linear coefficient of stress-induced bandgap shift in AlN than that of GaN is expected due to smaller lattice constant as well as higher mechanical strength of AlN than GaN. Although the value is deduced from the low temperature FX peak shift, the effect of measurement temperature is expected to be negligibly small. The results shown in Fig. 3.17 establish PL as a simple and effective method for monitoring the biaxial stress in AlN epilayers grown on different substrates and with different thicknesses, thereby providing a useful means for controlling and manipulating stress in AlN epilayers grown under different conditions.

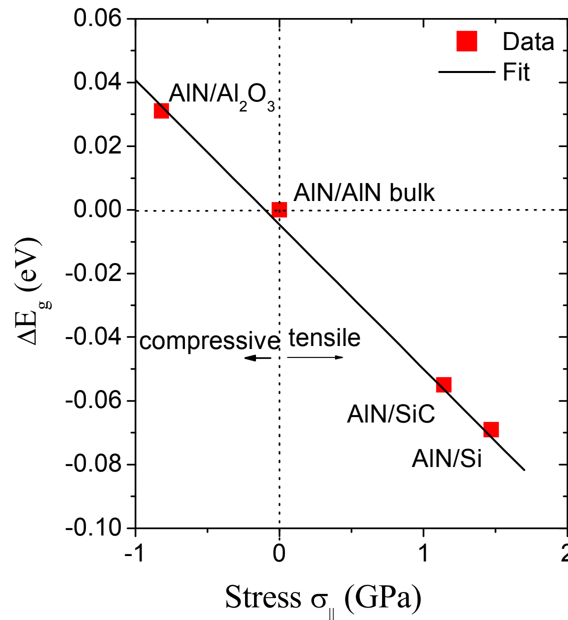

Figure 3.17 Stress-induced shift of the free exciton emission peak position in AlN epilayers as a function of the in-plane stress. The solid line is the least-squares linear fit of the experimental data. The linear coefficient of stress-induced bandgap shift in AlN epilayers is deduced to be 45 meV/GPa.

In summary, DUV PL spectroscopy and XRD have been employed to study AlN epilayers grown on sapphire, SiC, Si, and AlN bulk substrates. The spectral peak positions of the FX transitions and the lattice constants were systematically measured for epilayers grown on different substrates. AlN homoepilayers were confirmed to have the same lattice parameters as AlN bulk crystals and to be strain-free. Furthermore, compressive stress in AlN/sapphire and tensile strain in AlN/SiC and AlN/Si were verified. The stress-induced shift of the free exciton transitions in AlN epilayers grown on different substrates has been measured and correlated with XRD results, from which the stress-induced bandgap shift of 45 meV/GPa in AlN epilayers was deduced. The results presented here establish PL as another simple and effective method for monitoring the substrate induced biaxial stress in AlN epilayers in addition to XRD measurements.

CHAPTER 4- III-nitrides for thermoelectric thermopower generation

4.1. Introduction

Thermoelectric (TE) devices convert heat energy directly into electrical energy and are also used for removing local heat (cooler). Compared with other methods of electrical power generation and refrigeration, TE devices have numerous attractive features such as no moving parts, long life, low maintenance, no emission of ozone-depleting gases and radioactive radiation, light weight, small size, and high reliability [41]. However, their use has been limited due to their relatively low energy conversion efficiency. Currently, major uses of TE devices include cooling of laser diodes/beverage and providing power for deep space satellites where there is no sunlight (beyond solar system). In the past few years there has been tremendous progress in enhancing the performance of TE materials. Figure 4.1 shows the time-line of development for TE materials in terms of figure of merit (*ZT*), which will be defined later. A sharp increase in *ZT* >1 at 300 K in the year 2000 was found in nanostructured Bi_2Te_3 TE materials.

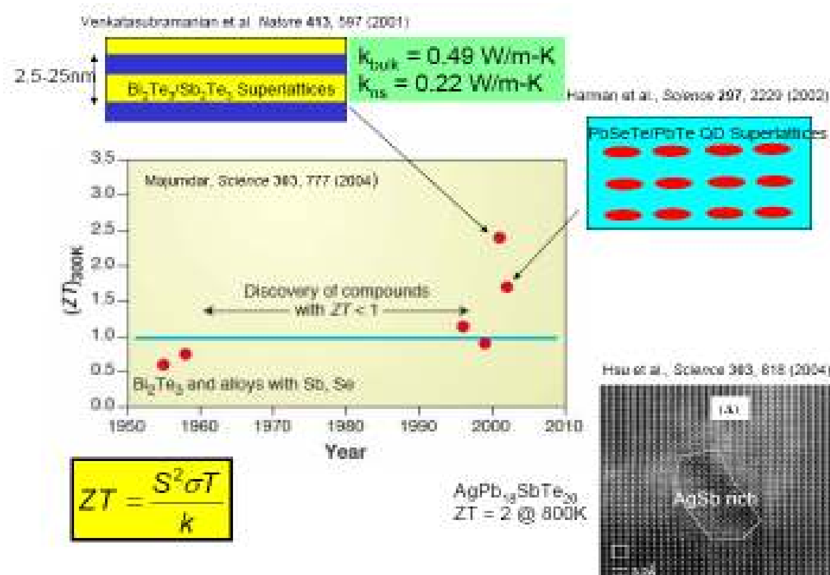

Figure 4.1 The history of TE materials developments

The best TE materials for room temperature applications are Bi_2Te_3 based materials [113, 114]. However, their applications are limited because tellurium is scarce, volatile, and toxic. Furthermore, the operational range of these materials is limited to temperatures lower than 100 ^{0}C. Therefore, the search for TE materials beyond tellurium based compounds is necessary. Some of the outstanding features of III-nitrides that are highly attractive for TE applications include the ability for high power and high temperature operation, high mechanical strength and stability, and radiation hardness. Additionally, III-nitrides offer tremendous potential enhancement of the TE figure of merit (ZT) via alloying, bandgap engineering and nano-structure incorporation. However, only a few reports concerning the thermal and TE properties of III-nitrides have been documented [9-11, 115]. Here, we investigate the potential of InGaN alloys as TE materials. Thin film TE materials in general, and InGaN thin films in particular, are of great interest because they offer the potential for direct integration of microcoolers/power generators with various photonic and electronic devices.

4.2. Thermoelectricity

Thermoelectricity (TE) is a phenomenon in solids in which a temperature difference creates electric potential and vice versa. Thermoelectric behavior depends in part on the Seebeck, Peltier and Thomson effects. They were discovered by Jean Peltier, Thomas Seebeck, and William Thomson, respectively between 1821 and 1855 [116].

4.2.1. The Seebeck effect

As shown in Fig. 4.2, two different conductors A and B have junctions at positions 1 and 2. If a temperature difference ΔT is maintained between the two junctions, then an open-circuit

potential difference ΔV is developed. This effect is called the Seebeck effect. The Seebeck coefficient S_{AB} is defined as,

$$S_{AB} = \lim_{T \to 0} \frac{\Delta V}{\Delta T}, \tag{4.1}$$

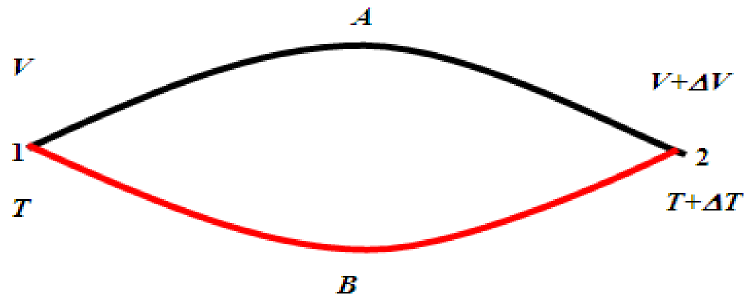

Figure 4.2 Schematic diagram for the Seebeck effect and A and B represent two different conductors.

If junction 1 is hotter than junction 2, a thermocouple *AB* that would drive a clockwise current is said to have positive *S*. In a closed circuit, the temperature difference induced Seebeck voltage can also be used to drive other electronic devices. This is how thermoelectric power generators work.

4.2.2. The Peltier effect

If two conductors *A* and *B* are joined together and a current *I* flows through the junction, then heat is generated or absorbed at the junction at a constant rate. This phenomenon is called Peltier effect. If an applied clockwise current (*I*) liberates heat at point *1* and absorbs heat at point *2*, then thermocouple is said to have a negative Peltier coefficient (Π). The rate of heat liberation or absorption at the junction is described by,

$$Q = \Pi_{AB} I \, , \tag{4.2}$$

Thermoelectric cooling is in fact the Peltier effect cooling.

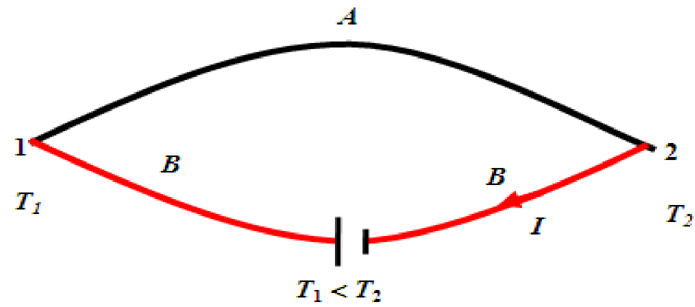

Figure 4.3 Schematic diagram for Peltier effect

4.2.3. The Thomson effect

As shown in Fig. 4.4, if a current *I* passes through a portion of a single homogeneous conductor over which there is a temperature difference ΔT, heat is liberated or absorbed at a rate ΔQ that is proportional to the *I* and ΔT. This phenomenon is called the Thomson effect. The Thomson coefficient τ is defined as,

$$\tau = \lim_{T \to 0} \frac{\Delta Q}{I \Delta T} \, , \tag{4.3}$$

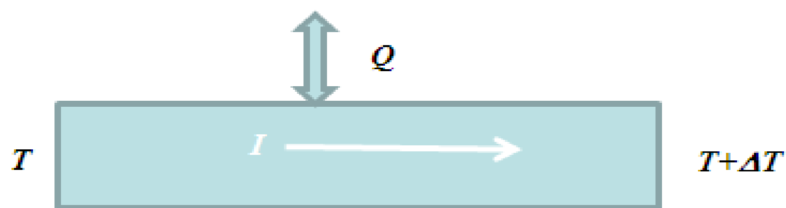

Figure 4.4 Schematic diagram for the Thomson effect

The Thomson coefficient is taken to be positive if heat liberates when a positive current passes from a higher to a lower temperature.

4.2.4. The Kelvin relation

The above three thermoelectric effects are connected by the following relations called the Kelvin relation [116].

$$\tau_A - \tau_B = T\frac{dS_{AB}}{dT}, and \tag{4.4}$$

$$\Pi_{AB} = S_{AB}T, \tag{4.5}$$

The equations (4.4) and (4.5) provide the fundamental links between thermoelectric power generation (*S*) and cooling (*Π*). Thermometric devices require joining two different materials; therefore *S* and *Π* of couples matter in practice. Since *S* is the easiest parameter to measure and relates to *Π*, we often measure *S* of materials.

4.2.5. Basics of thermoelectric devices

Thermoelectric cooling or power generating devices consist of large numbers of p- and n-type elements (TE legs) connected in series electrically and in parallel thermally. Schematics of single couple TE devices consisting of p and n type elements are shown in Fig. 4.5. In TE power generation (Fig 4.5 (b)), temperature difference creates a potential difference between the two ends of the couple which then drives the current in the circuit. In TE cooler, input current drives

the charge carriers which either give or absorb heat to or from the metal due to Peltier effect as shown in Fig 4.5 (c).

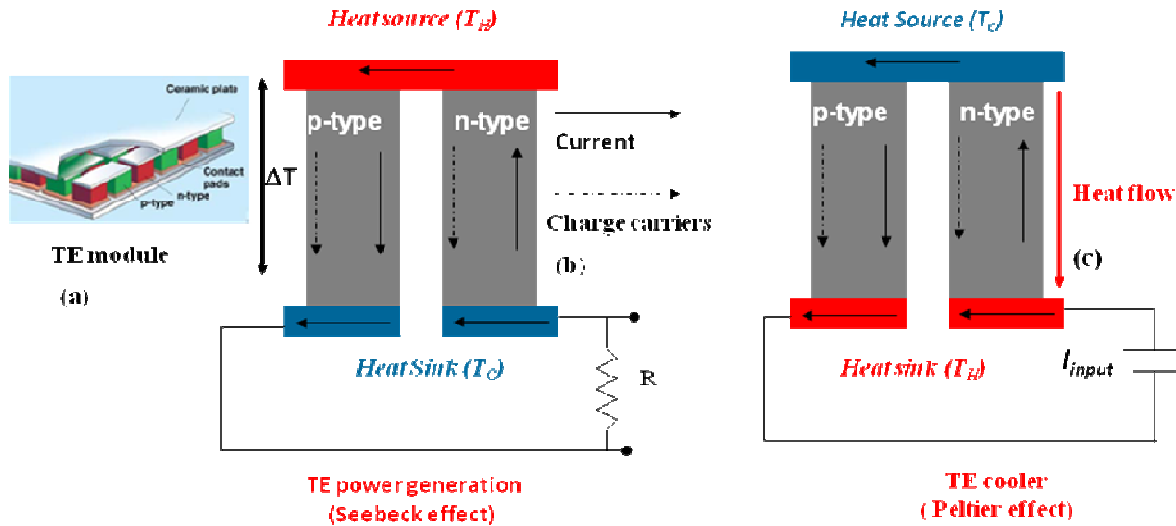

Figure 4.5 Schematic diagram for thermoelectric devices

4.2.6. Thermal and electrical conductivities

Thermal conduction and joules heating are two irreversible processes. Both lower the performance of TE devices. In TE power generation, a temperature gradient leads to an irreversible flow of heat due to thermal conduction that opposes the temperature gradient. Further, if there is flow of current I in the same direction due to the Seebeck effect, the Peltier effect opposes the temperature gradient due to electrical resistivity ρ (joules heating). In the case of TE refrigeration, one can't increase thermal gradient indefinitely by simply increasing I since joules heating is proportional to I^2. However the Peltier effect is only linear with I, so good TE materials should have high S with low ρ and low thermal conductivity κ.

4.2.7. Thermoelectric figure of merit

The performance of TE materials is quantified by the TE figure of merit (ZT) which is defined as [117],

$$ZT = \frac{S^2\sigma}{\kappa_T}\,T, and \qquad (4.6a)$$

$$\kappa_T = \kappa_e + \kappa_{ph}, \qquad (4.6b)$$

where, S = Seebeck coefficient, σ = electrical conductivity (reciprocal of resistivity ρ), κ_T = total thermal conductivity, κ_e, and κ_{ph} are electronic and phonon part of thermal conductivity respectively, and T is absolute temperature. While there is no fundamental upper limit to ZT, progress has been extremely hard to come by, mainly due to the coupling between S, σ, and κ. Changing one parameter would alter the others as well.

4.2.8. Thermoelectric power factor (*P*)

The product $S^2\sigma$ is called the power factor (P), and measures the electrical power generation capability. This figure is often used to assess the potential of materials for TE applications. Figure 4.6 shows a general relationship between S and σ in metal, semimetal or heavily doped semiconductor and semiconductor [118]. The TE power factor maximizes somewhere between metals and semiconductors. Good TE materials are typically heavily doped semiconductors or semimetals with a carrier concentration of 10^{19} to 10^{21} carriers/cm^3. The Fig. 4.6 below shows the a typical behavior of S, σ, and P with carrier concentrations. The trade-off between S and σ can be described by the following two equations [119].

$$\sigma = ne\mu, \tag{4.7}$$

$$S = \frac{k}{e}\left(r + \frac{5}{2} + ln\frac{N_c}{n}\right), \tag{4.8}$$

where e, μ, r, N_C, and n are electric charge, Hall mobility, scattering factor, effective density of states in the conduction band, and electron concentration, respectively.

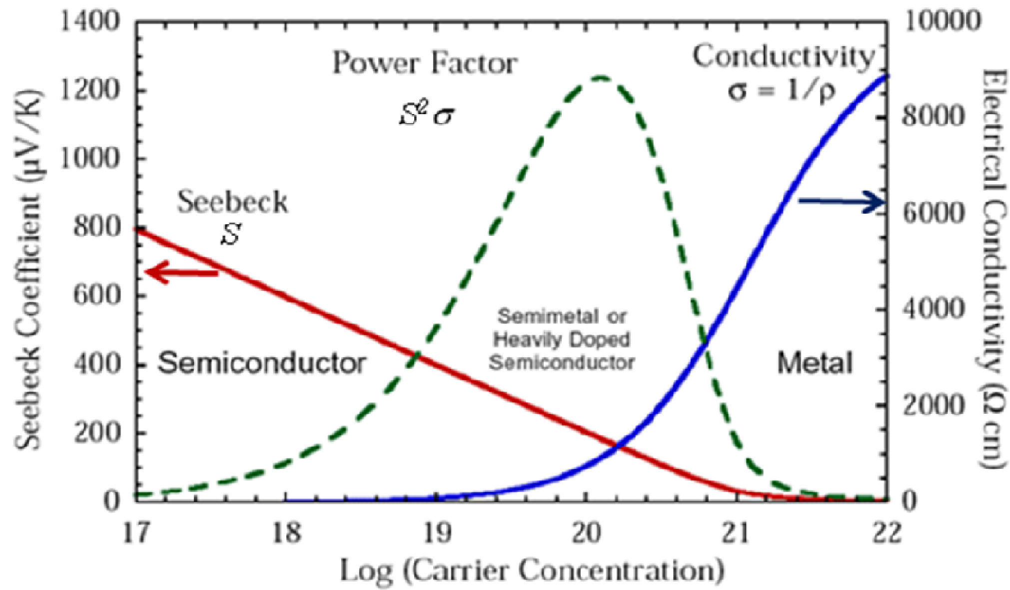

Figure 4.6 TE parameters in different materials and carrier concentrations (Ref.118).

4.3. Experimental investigation of thermoelectric properties of InGaN alloys

4.3.1. Optimization of power factor in InGaN alloys

The performance of TE devices is characterized by the material's TE figure of merit, Z ($Z = P/\kappa$, and $P = S^2\sigma$). Since S and σ depend on each other, the optimization of product $S^2\sigma$ is extremely important to achieve high Z. We have performed this experimentally in $In_{0.3}Ga_{0.7}N$ alloy by varying electron concentrations in order to optimize the figure of merit.

An un-doped and several Si-doped $In_{0.3}Ga_{0.7}N$ alloy samples, of thickness ~110 nm, were grown on ~1 μm GaN/sapphire (0001) templates by metal organic chemical vapor deposition (MOCVD). Ammonia (NH_3), trimethylgallium (TMGa), trimethylindium (TMIn), and silane were used as precursors and dopants. The thickness of the films was estimated from *in-situ* interference measurements during the epi-growth. The indium concentration was determined from peak value of x-ray diffraction (XRD) spectra of (002) reflection in θ-2θ scan mode and applying Vegard's law.

The Seebeck coefficient and electrical conductivity measurements were performed by temperature gradient and Vander Pauw Hall-effect measurement methods in the in-plane direction. Since InGaN samples were grown on GaN/sapphire templates, we performed two identical measurements in GaN/sapphire template (reference) and InGaN/GaN/sapphire samples (sample). The following two equations were used to extract the properties of top InGaN films [120].

$$\sigma_f = \frac{\sigma_s t_s - \sigma_r t_r}{t_s - t_r}, \tag{4.9}$$

$$S_f = \frac{S_s \sigma_s t_s - S_r \sigma_r t_r}{S_s t_s - S_r t_r}, \tag{4.10}$$

where σ, S, and t stands for electrical conductivity, Seebeck coefficient, and layer thickness, respectively and suffix f, S, and r stand for film, sample and reference, respectively.

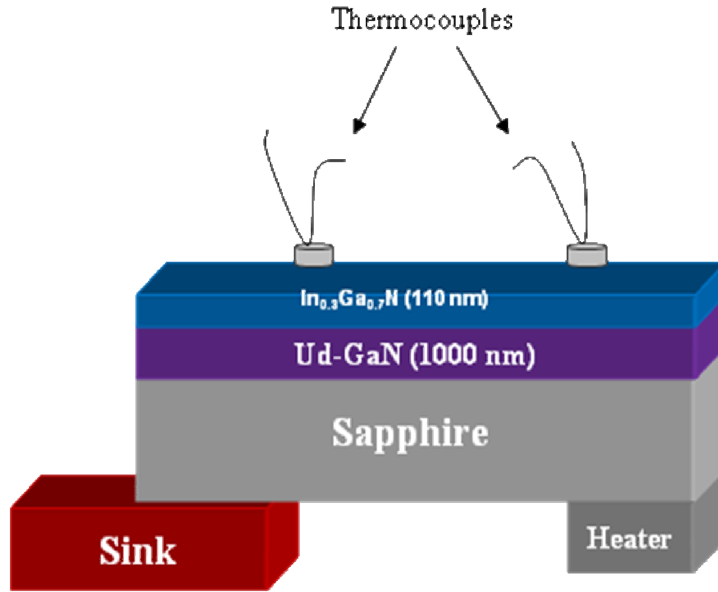

Figure 4.7 Schematic illustration of Seebeck coefficient (V_s) measurement method.

A schematic illustration of the experimental set up for Seebeck coefficient measurement is shown in Fig. 4.7. The sample to be measured was cut into a rectangular shape (~ 5 x 20 mm^2). One end of the sample was placed on the sink while on the other end, a heater was attached. On the surface of the sample, two thermocouples separated by ~ 8 mm were attached. In-plane temperature gradient was created along the sample by the heater. The Seebeck voltage and temperature gradients were measured by thermocouples. Temperature dependent measurements were performed in a cryostat with a temperature range from 300 to 750 K.

Figure 4.8 shows the Seebeck voltage (V_S) of samples with different electron concentrations (n) as a function of temperature gradient. Slope of the linear fit of the data is the measure of the Seebeck coefficients (S).

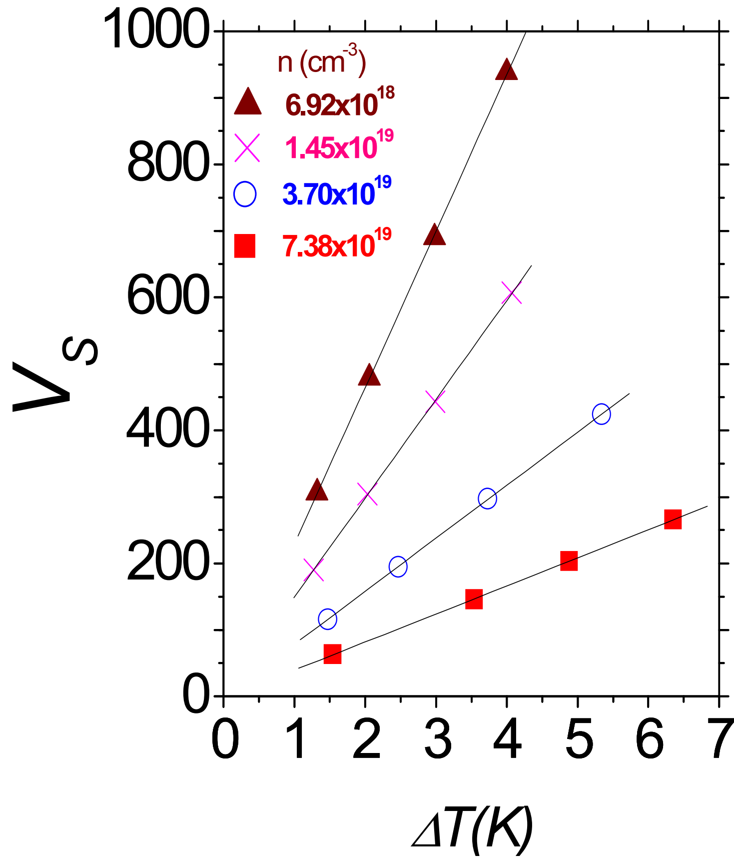

Figure 4.8 The measured Seebeck voltage V_s of $In_{0.3}Ga_{0.7}N$/GaN/sapphire samples of different electron concentrations (n) at as a function of ΔT.

Electrical conductivity (σ) and S of the top InGaN layer were extracted using Eqs. (4.9) and (4.10) respectively. Figure 4.9 (a) shows σ and S of $In_{0.3}Ga_{0.7}N$ alloys as functions of electron concentration. The usual trade-off behavior of σ and S is observed. S decreases while σ and n increase as described by above equations (4.7) and (4.8).

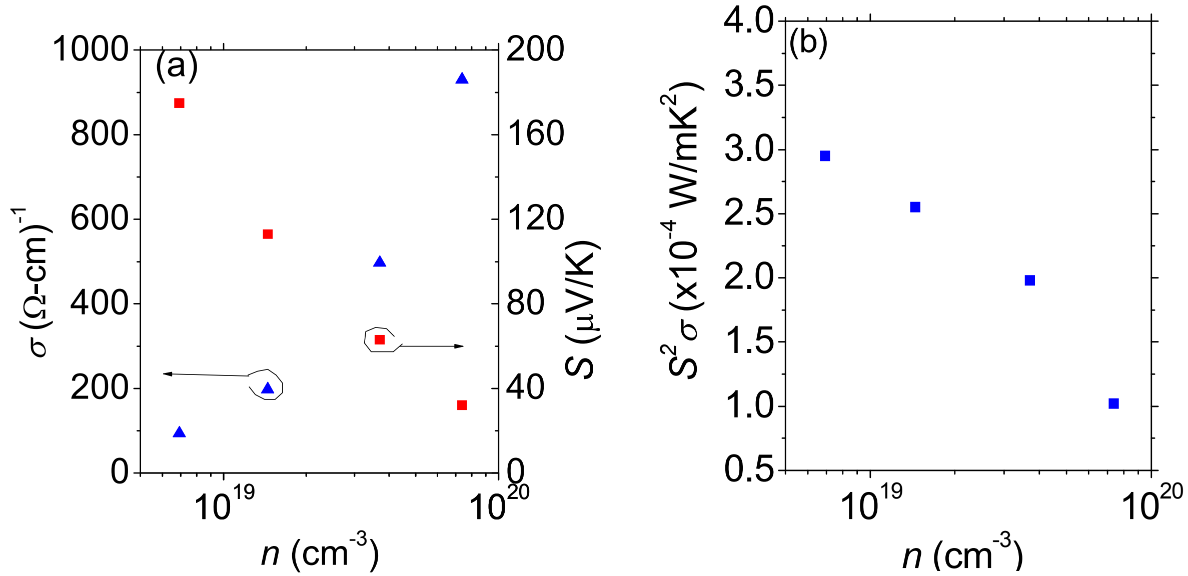

Figure 4.9 (a) Electrical conductivity (σ) and the Seebeck coefficient (S) and (b) power factor ($S^2\sigma$) as functions of electron concentration (n) of $In_{0.3}Ga_{0.7}N$ alloys.

The variation of P with n is plotted in Fig. 4.9 (b) which shows that P increases as n decreases. The maximum value of P was found in an un-doped sample ($n \sim 7\text{x}10^{18}$ cm^{-3} measured at 300 K) which is ~ 2.8x10^{-4} W/m-K^2 at 300 K. The peak value of P has yet to be found because further decreasing the carrier concentration is limited by the presence of a high background concentration of electrons which arises from native defects such as oxygen and hydrogen impurities and nitrogen vacancies [121]. Recently, our group has demonstrated the mechanism of suppressing electron background concentrations and improving the quality of InN by using AlN template and higher growth temperature [122]. The issue of a high background concentration of electrons in InGaN alloys with relatively high In-contents is currently under intensive investigation [123, 124] and significant improvements in InGaN material quality and conductivity control are expected, which will lead to further enhancement in P in InGaN alloys with larger In-contents.

The temperature dependent TE properties of $In_{0.3}Ga_{0.7}N$ alloy was measured in the temperature range from 300 to 750 K. Figure 4.10 (a) shows S and σ of $In_{0.3}Ga_{0.7}N$ alloy as functions of absolute temperature (T). It was found that S increases as T increases, whereas σ remains almost unchanged. The increase in S (regardless of no change in σ) could be due to the electron hopping conductance at higher temperatures as described by Yamaguchi *et al.* [9] in InAlN and AlInGaN alloys. The maximum Seebeck coefficient was measured to be 280 μV/K at 750 K. Temperature dependent P is plotted in Fig. 4.10 (b), which shows that P increases as T increases. The maximum measured value of P was 7.3x10^{-4} W/mK^2 at 750 K. This value is about two times higher than that of $Al_{0.35}In_{0.65}N$ and more than one order of magnitude higher than in $Al_{0.26}Ga_{0.44}In_{0.30}N$ [9]. The results suggest that $In_xGa_{1-x}N$ alloys are better candidates for TE applications than other AlInGaN alloy systems.

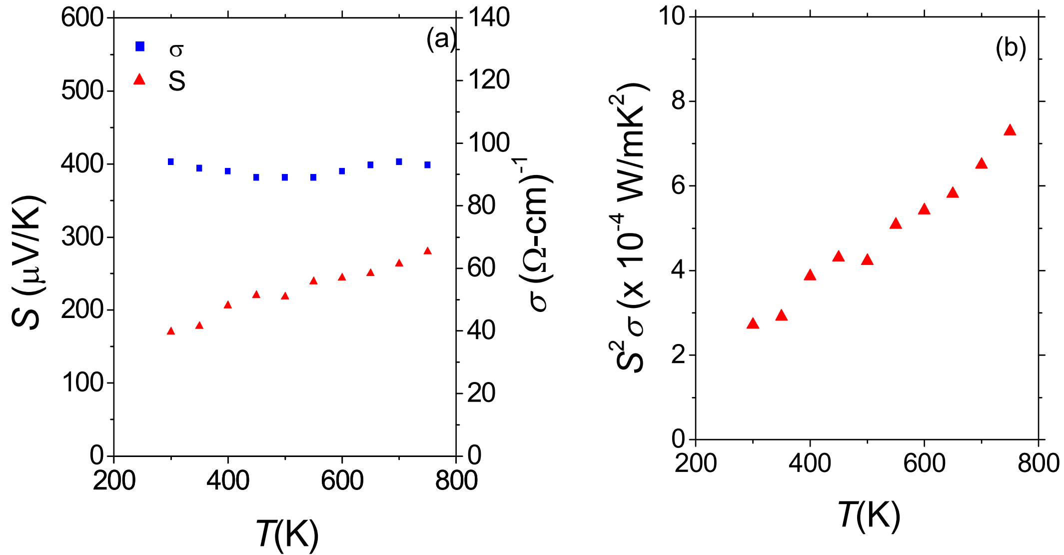

Figure 4.10 (a) Electrical conductivity (σ) and the Seebeck coefficients (S) and (b) power factor ($S^2\sigma$) as functions of temperature (T) of $In_{0.3}Ga_{0.7}N$ alloy with electron concentration ~7x10^{18} cm^{-3}.

In summary, we have measured the TE properties of MOCVD grown on un-doped and Si-doped $In_{0.3}Ga_{0.7}N$ alloys. The power factor *P* was observed to be at maximum in the un-doped sample. Further increase in power factor can be expected by reducing the background electron concentration and improving the material quality. It was found that the power factor increases as temperature increases with a maximum value of $7.3x10^{-4}$ W/mK^2 at 750 K.

4.3.2. Thermal conductivity of InGaN alloys

Since the thermal conductivities of binary III-nitride crystals such as InN, GaN, and AlN are very high (>100 W/mK) [125-127], their prospects for TE device applications are limited. The current research in thin film TE materials without tellurium is concentrating on materials such as Si/Ge, SiGe/Si, and ErAs:InGaAs/InGaAlAs supperlattices and SiGe alloys [128-132]. It has been observed that alloying significantly reduces κ in solids with very little deterioration of electrical properties [9-11, 114, 115, 125-133], making alloys a good candidate as TE materials. Here, we measure the thermal conductivity of $In_xGa_{1-x}N$ alloys as a function of In content.

$In_xGa_{1-x}N$ alloys (~110 nm in thickness) were grown on GaN/sapphire (001) templates (reference sample). The indium concentrations were determined by ω-2θ scans of the (002) reflection peak using x-ray diffraction. Thermal conductivity measurements were performed by the differential 3ω method [62, 67, 69, 134, 135]. The material structures and heater/sensor geometry employed for the thermal conductivity measurements are schematically illustrated in Fig.4.11

Since both $In_xGa_{1-x}N$ samples and GaN/sapphire templates (reference samples) are electrically conductive, we deposited 150 nm SiO_2 on the surfaces of both structures prior to the deposition of line heater/sensor. This layer provides the electrical insulation required for the 3ω

measurements. Then, heaters/sensors of identical geometry, composed of Ni (20 nm)/Au (130 nm) with a wire width and length of 12 and 1000 μm, respectively, were patterned on the top of the SiO_2 layer of both structures using optical photolithography followed by metal deposition and lift-off techniques. A digital lock-in amplifier was used to feed the sinusoidal current into the specimen at an angular frequency ω and collect the voltage at a frequency 3ω across the metal heater/sensor. Our detection system was calibrated by measuring κ values of sapphire and SiO_2 with measured κ values being 27.7 and 1.16 W/mK respectively, which agree well with literature values [11, 69, 136].

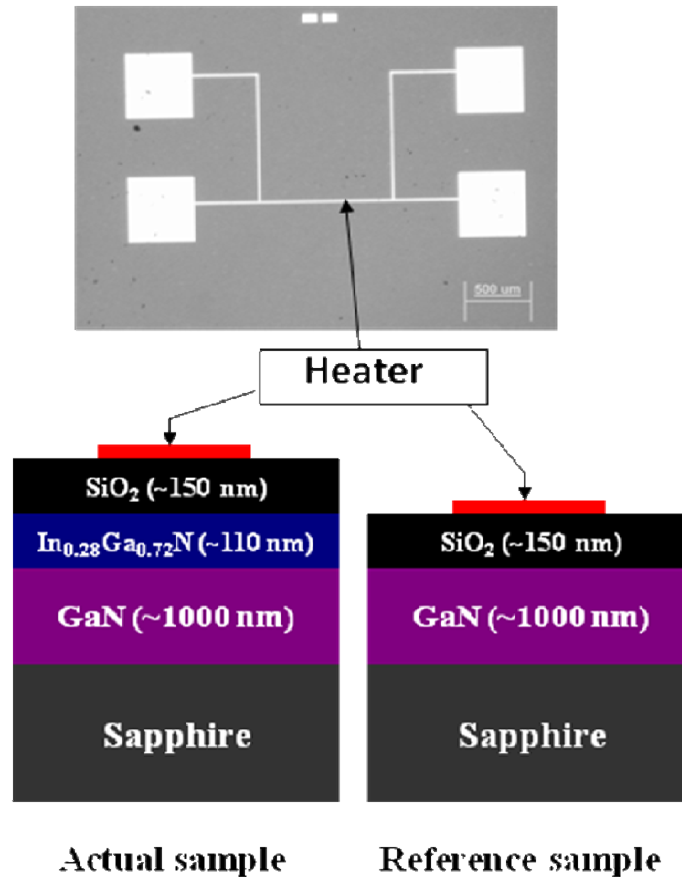

Figure 4.11 Schematic illustration of cross sections and optical photograph of the top surface of a fabricated sample for 3ω measurements.

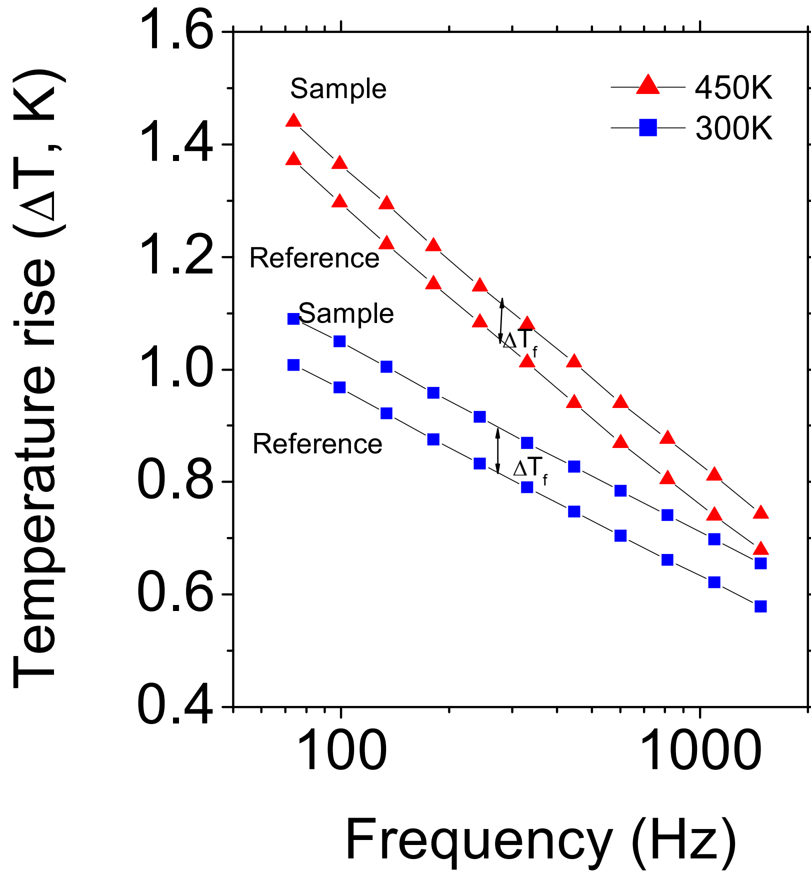

Figure 4.12 In-phase components of the temperature oscillation (ΔT) of the heater/sensor as a function of frequency of the driving current measured at 300 and 450 K for the reference (GaN/sapphire template) and an actual sample ($In_{0.28}Ga_{0.72}N$ epilayer grown on GaN/sapphire template).

Figure 4.12 shows the temperature oscillation ΔT in the line heater/sensor patterned on one of the $In_xGa_{1-x}N$ thin films (an actual sample) and its reference sample (GaN/sapphire template) as a function of frequency of the driving current measured at 300 and 450 K. The temperature drop across the film ΔT_f was calculated by subtracting ΔT of a reference sample

from ΔT of the actual sample. The mean value of ΔT_f in the entire frequency range was used to calculate κ. Standard deviations in measured ΔT_f were less than 3%. At 300 K, the measured κ of $In_xGa_{1-x}N$ alloys are 8.1, 5.4, 2.7, and 1.05 W/m K for x=0.16, 0.22, 0.28, and 0.36, respectively.

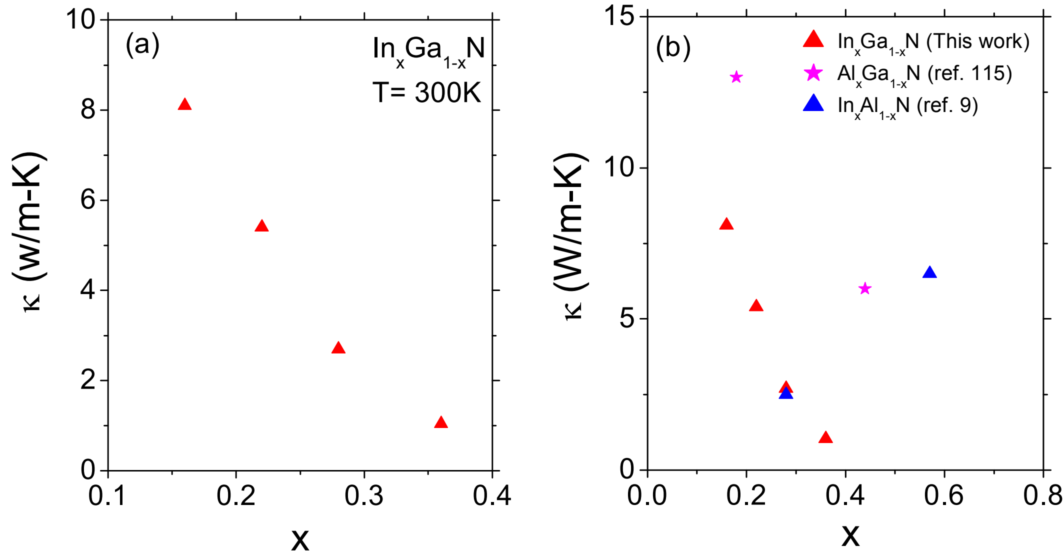

Figure 4.13 (a) Thermal conductivity (κ) of $In_xGa_{1-x}N$ alloys as a function of In content (x) at 300 K. (b) comparison of our data with $Al_xGa_{1-x}N$ and $In_xAl_{1-x}N$ [9,115].

Figure 4.11. shows the variation of κ with x, for $In_xGa_{1-x}N$ alloys measured at 300 K. Results for $Al_xGa_{1-x}N$ (Ref. 115) and $In_xAl_{1-x}N$ (Ref. 9) alloys are also included for comparison. A significant reduction in κ of $In_xGa_{1-x}N$ alloys with increasing x is observed, which is mainly attributed to the scattering of phonons due to the alloy disorder [11, 117, 125, 137].

The idea that solid alloys (solid solution) might be superior to elements or compounds in TE properties was first proposed by Ioffe *et al.* [42]. In alloys, most of the heat is transported by phonons which have a much shorter wavelength would be effectively scattered by short-range

disorder. In contrast, the wavelength of charge carrier is comparatively longer and would not affect much in mobility. Phonons are scattered by variation of both elasticity and density (mass-fluctuation). Thus, thermal conductivity of a ternary alloy $A_xB_{1-x}C$ can be estimated from their constituents' binary compounds and a scattering parameter as follows [117, 137],

$$\frac{1}{\kappa(x)} = \frac{x}{\kappa_{AB}} + \frac{1-x}{\kappa_{AB}} + \frac{x(1-x)}{C_{A-B}}, \tag{4.11}$$

$$\text{where, } C_{A-B} = N\left[\left\{\frac{\Delta M}{M(x)}\right\}^2 + g\left\{\frac{\Delta a}{a(x)}\right\}^2\right], \tag{4.12}$$

$$\Delta M = M_A - M_B, \qquad \Delta a = a_{AC} - a_{BC} \tag{4.13}$$

$$M(x) = xM_A - (1-x)M_B, \qquad \text{and } a(x) = xa_{AC} - (1-x)a_{BC} \tag{4.14}$$

Where, κ = Thermal conductivity, $C_{A\text{-}B}$ = contribution arising from lattice disorder due to random distribution of the *A* and *B* atoms usually called bowing or non-linear parameter. *N* = a phenomenological, adjustable parameter, *M* = average atomic weight, and *a* = average lattice parameter.

The mass fluctuation effect is easier to determine theoretically and considered to be predominant in most of the alloys. Most of the experimental data fits well with the theoretical curves calculated by using mass disorder only. If calculated κ is less than the observed one, then, it is reasonable to suggest that the disagreement can be attributed to a significant strain scattering effect. Besides these, there might be some effect from boundary scattering and scattering from dislocations as InGaN is plunged by large number of threading dislocations due to large lattice mismatched with the substrate on which they were grown. The κ values of $In_xGa_{1-x}N$ alloys, we

measured here, are better in particular for high In content, to those of other nitride systems, such as $In_xAl_{1-x}N$ and $Al_xGa_{1-x}N$.

4.3.3. Thermoelectric figure of merit in InGaN alloys

In order to evaluate the TE figure of merit (ZT), Seebeck coefficients (S), and electrical conductivities (σ) of $In_xGa_{1-x}N$ alloys were measured by a temperature gradient method [132] and van der Pauw Hall-effect measurement [138] in the in-plane direction.

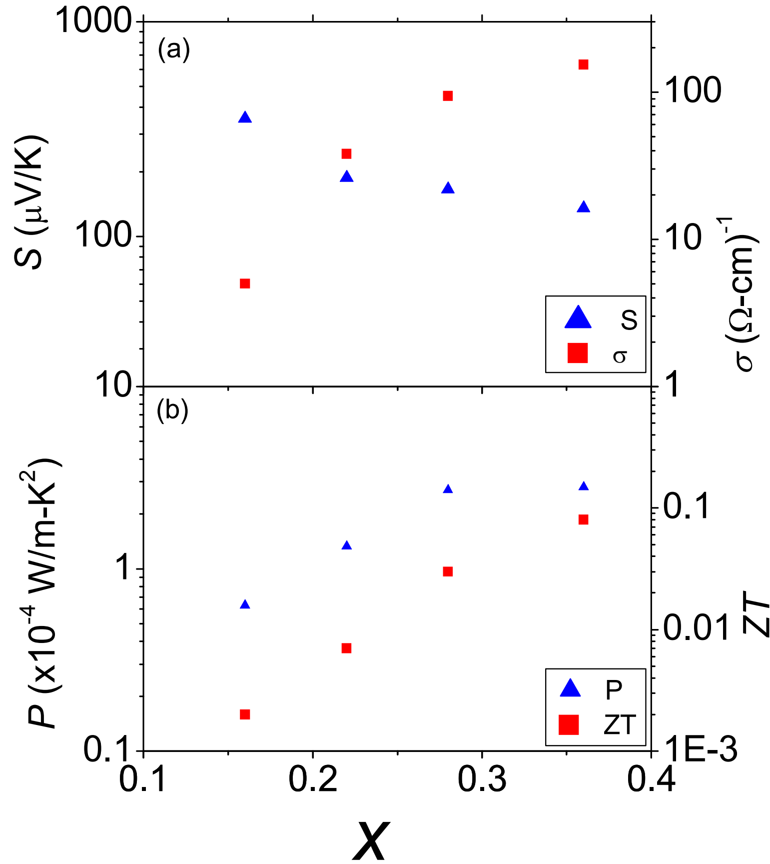

Figure 4.14 (a) Seebeck coefficient (S) and electrical conductivity (σ) of $In_xGa_{1-x}N$ alloys as functions of In content (x). (b) Power factor ($P=S^2\sigma$) and figure of merit (ZT) of $In_xGa_{1-x}N$ alloys as functions of In content (x) measured at 300 K.

Figure 4.14 (a) shows the measured S and κ of $In_xGa_{1-x}N$ alloys as functions of In content ($0.14 < x < 0.36$). S decreases while σ increases with an increase of x. The reason for this trade-off relationship between S and σ is due to the increased background electron concentration with an increase of x in $In_xGa_{1-x}N$ alloys. In Fig. 4.14 (b), we plot the power factor (P=$S^2\sigma$) and ZT as functions of In content. Both P and ZT are observed to increase with x. At 300 K, ZT = 0.08 is obtained in the $In_{0.36}Ga_{0.72}N$ alloy, which is much larger than those in AlInN [10] and AlGaN [11] alloys in which ZT is around (or even smaller than) 0.001 at 300 K. This may be due to the fact that phonons are more easily scattered in $In_xGa_{1-x}N$ alloys than in the other two ternary alloy systems, attributing to a more pronounced local strain-scattering effect because In atoms are larger than Ga and Al [117].

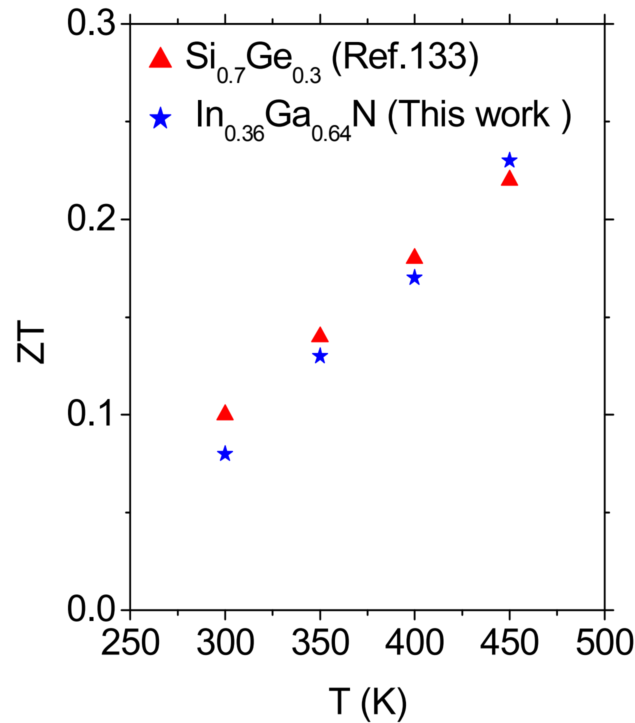

Figure 4.15 Measured ZT values of $In_{0.36}Ga_{0.64}N$ alloy from 300 to 450 K. Data for SiGe alloys [133] are included for comparison.

Furthermore, for materials with comparable free electron concentrations, InGaN has higher electron mobility than AlGaN or AlInN. The issue of high background electron concentration in InGaN alloys with relatively high In contents is currently under intensive investigation [123, 124] and significant improvements in InGaN material quality and conductivity control are anticipated, which will lead to further enhancement in *ZT* and *P* in InGaN alloys with larger In contents.

The temperature dependent TE properties of $In_xGa_{1-x}N$ alloys were also measured in the temperature range from 300 to 450 K. Figure 4.15 shows *ZT* of $In_{0.36}Ga_{0.68}N$ alloy as a function of temperature. Data for SiGe alloys [133] are also included for comparison. The *ZT* values of $In_{0.36}Ga_{0.64}N$ alloy in the measured temperature range are comparable to those of the SiGe alloys, which is the current prime choice of TE materials for thermopower generation in high temperature environments such as in radio-isotope TE generators. We observed that *ZT* increases linearly with temperature and reaches a value of 0.23 at 450 K. The results suggest that $In_xGa_{1-x}N$ alloys may replace SiGe alloys for applications in prolonged TE device operation at high temperatures due to their superior physical properties over those of SiGe, including the ability to operate in high temperature/high power conditions and their high mechanical strength and stability.

4.3.4. Conclusion and future direction of InGaN alloys as TE materials

The thermoelectric (TE) properties of $In_xGa_{1-x}N$ alloys grown by metal organic chemical vapor deposition have been investigated. It was found that as In content increases, the thermal conductivity decreases and power factor increases, which leads to an increase in the TE figure of merit (*ZT*). The value of *ZT* was found to be 0.08 at 300 K and reached 0.23 at 450 K for

$In_{0.36}Ga_{0.64}N$ alloy. Our result suggested that ZT would be even higher if we increased In content in InGaN. High quality InGaN with In > 40 % is very difficult to achieve due to solid state miscibility and other reasons which will be discussed in chapter 5. However, In-rich InGaN alloys have attracted much attention in recent years due to its applications as active materials in many solid state devices such as solar cells, PEC cells, TE devices, and long wavelength emitters.

Since TE devices consist of both p-type and n-type materials, investigation of the TE properties of p-InGaN alloys is realize priority for the realization of real TE devices from InGaN alloys. Recently, we have achieved p-type conductivity (chapter 6) in InGaN alloys up to In= 35%. So the TE devices (micopower generators and microcoolers) consisting of InGaN materials are on the road in the future. Further, significant enhancement in the TE figure of merit of InGaN alloys is anticipated due to the fact that III-nitrides potentially offer tremendous scope for the enhancement of *ZT* values via the bandgap engineering and nanoscale structuring (eg. quantum dots quantum wires etc), which were shown in other material systems to allow one to either use quantum confinement of carriers or spectrally dependent scattering of phonons to manipulate S, κ, and σ independently that can increase *ZT* beyond the bulk values [139]. Furthermore, III-nitride planar processing is now well developed for photonic/electronic devices and sensors, which can facilitate relatively low cost fabrication by the use of existing semiconductor processing equipment. Finally, future communication platforms will employ highly sophisticated micro-nanoscale sensor systems in which III-nitride based devices will play increasingly important roles because of their superior material properties. The development of III-nitride based TE devices may open up the possibility for monolithic integration of TE power generator/cooler modules onto remote micro-nanoscale sensor networks.

CHAPTER 5-Growth and characterization of single phase InGaN alloys in the middle range

5.1. Introduction

InGaN ternary alloys are of great interest because of their ability to tune the direct band gap from the infrared region of ~0.7 eV (InN) to the UV region of ~3.4 eV (GaN) [3-5, 140]. In particular, high quality In-rich InGaN alloys have potential applications in many important areas including (1) full solar spectrum, high efficiency, and radiation hard multijunction solar cells [12], (2) high efficiency photoelectrochemical (PEC) cells for H_2 generation using sunlight to split water [48, 141], and (3) high brightness nitride green light emitting diodes (LEDs) and laser diodes (LDs) [3]. More recently, our group showed that high In-content InGaN alloys are potentially important thermoelectric (TE) material for power generation and/or solid-state cooling (Chapter 4). These findings have further broadened the applications of ternary InGaN alloys into new areas that are distinctively different from traditional optoelectronics.

Many previous experimental studies have found that the growth of high quality In-rich InGaN is extremely challenging due to the low solubility of InN (GaN) in GaN (InN) (solid phase miscibility gap that usually results in phase separation in InGaN alloys). Phase separation in InGaN has been theoretically predicted and experimentally observed [51, 143-146]. However, single phase InGaN alloys can be achieved in the entire composition range under certain growth conditions. Ho and Stingfellow's [144] calculation showed that the solubility of InN in GaN is only about 6% at growth temperature ~ 800 ^{o}C and the miscibility gap covers almost the entire composition range. On the other hand, Karpov's [147] calculation revealed that phase separation may be considerably suppressed if the strain produced during the epitaxial process is taken into

account; however, the problem remains significant for In content higher than 40%. The calculation also implied a much lower critical temperature and increased solubility in strained InGaN alloys (750 °C versus 1175 °C and 6% versus 35%) compared to previously calculated results [144]. This could be one of the reasons that InGaN alloys with InN content up to 30% (inside the miscibility gap from Ref. [144] without phase separation have been repeatedly grown by several techniques [51, 143, 148, 149]. In a previous work, it was shown that single phase $In_xGa_{1-x}N$ films of x=0.5 to 1 can be grown by metal organic chemical vapor deposition (MOCVD) by lowering the growth temperature to 550 °C [150]. More recently, InGaN alloys and nonowires without phase separation have been grown by molecular beam epitaxy and by low pressure halide phase epitaxy in the entire composition range [53, 151].

The phase separation in InGaN alloys is believed to have arisen due to the large difference in the equilibrium lattice constants of InN and GaN (11%). This difference in equilibrium results in a considerable internal strain. Figure 5.1 shows the phase diagram (T-x) of $In_xGa\text{-}_{1x}N$ alloys system calculated by Ho and Stringfellow using modified virtual-force-field (VFF) model [144]. Binodal curve at a given temperature is calculated as In composition where first derivative of enthalpy mixing energy with respect to composition is zero $(\delta H/\delta x = 0)$. The spinodal decomposition is that where $\delta^2 H/\delta x^2 = 0$. The solid solution is stable outside the bimodal curve and unstable inside the spinodal curve. The region between the two curves is called metastable state. This model found that the critical temperature where stable and unstable solution co-exist is very high (1250°C) at In = 0.5. and solubility of InN in GaN is very low. This calculation suggested that the InGaN alloys are unstable for nearly the entire range of solid solution.

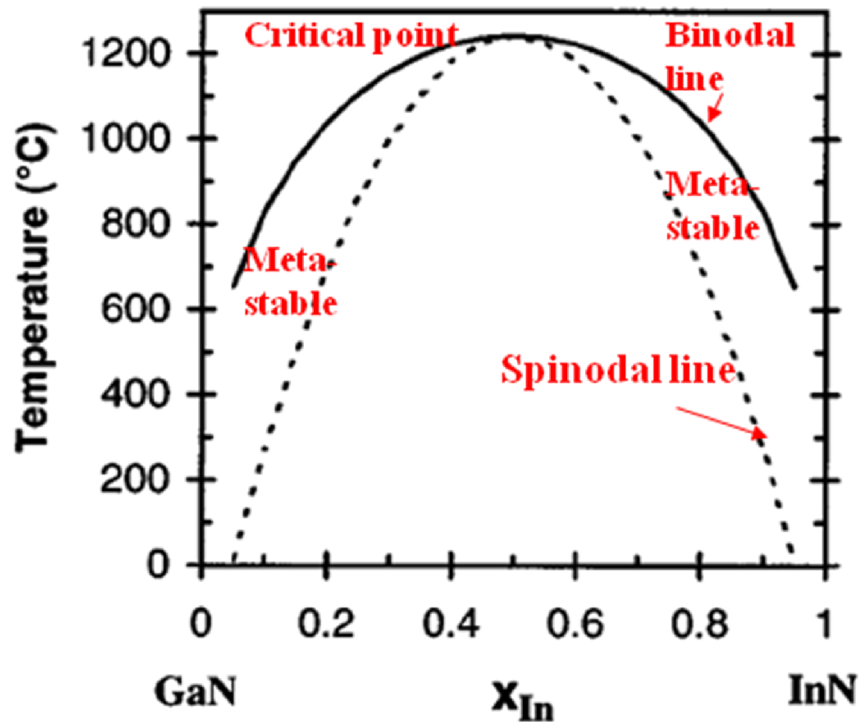

Figure 5.1 Binodal (solid) and spinodle (dahed) curves for the InGaN alloys, calculated assuming a constant average value for the solid phase interaction parameter [144].

5.2 Growth conditions for the suppression of phase separation

5.2.1 Biaxial strain

InGaN alloys are normally grown on sapphire substrates or GaN/sapphire or AlN/sapphire templates. Since the lattice constants of sapphire, GaN, and, InN are so different, InGaN epitaxially grown on underlying substrates or templates is uniformly strained until a certain thickness. This effect has been studied by Kaporav in 1998 [147]. Figure 5.2 compares the phase diagrams of relaxed and stained InGaN alloys. The result suggests that phase separation in InGaN alloys can be considerably suppressed in strained layers with a shift in the phase separation region towards higher indium mole fraction.

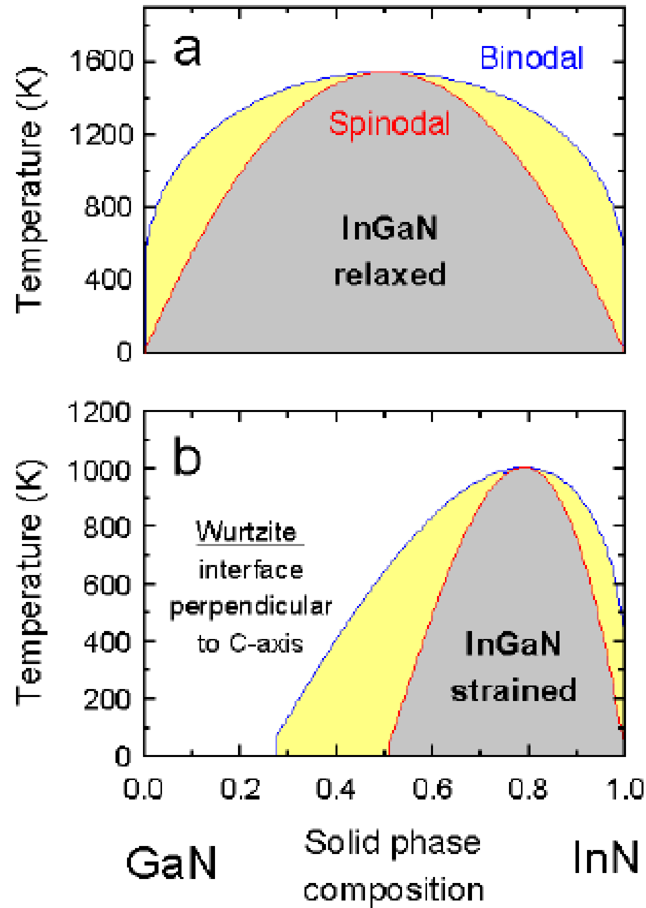

Figure 5.2 T-x phase diagram of ternary $In_xGa_{1-x}N$ alloys for (a) relaxed layers, (b) strained layers [147].

We observed this effect experimentally in InGaN alloys grown on AlN/sapphire templates by MOCVD. Figure 5.3 (a), for example, shows ω-2θ spectra of (002) plane of $In_{0.65}Ga_{0.35}N$ alloys of different layer thickness. The layer structure is shown in Fig. 5.3 (b) Single phase was observed for InGaN alloys with a thickness of 1 μm. Multiple peaks correspond to different phases and an metal peak was obtained in the 2 μm thick layer. We believe that this layer is thick enough to release biaxial stain. Hence, one can conclude that the absence of biaxial stain is the one of the reasons for phase separation.

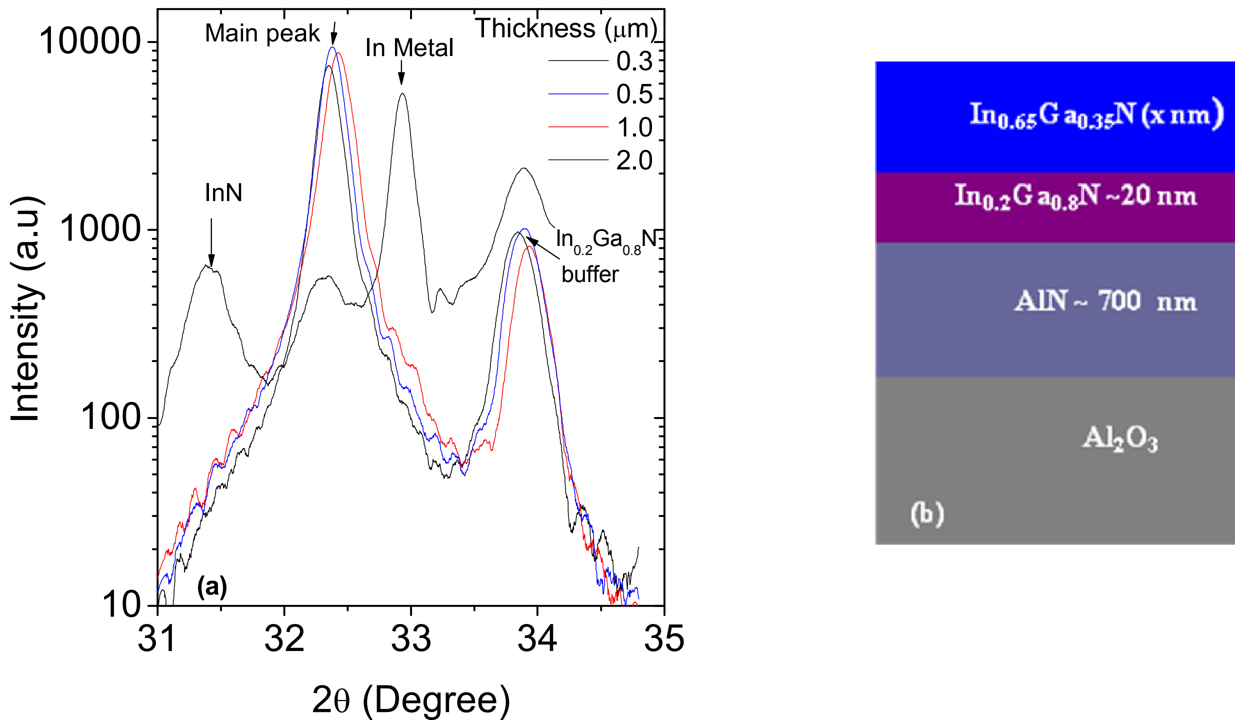

Figure 5.3 (a) X-ray diffraction spectra of (002) plane of $In_{0.65}Ga_{0.55}N$ alloys of different layer thickness in ω-2θ scan mode, (b) Layer structure.

5.2.2. Thermodynamic process:

The T-x phase diagram for InGaN alloys is mostly modeled or calculated under equilibrium condition [144]. In contrast, MOCVD growth process is far away from this condition. So, we believe that non-equilibrium nature of MOCVD growth could be one of the main reasons of successful growth in single phase InGaN alloys in the theoretically predicted phase separation region. We believe that a higher growth rate favors non-equilibrium conditions. As shown in Fig 5.4, at lower growth rate (210 nm/hr) XRD curve for ω-2θ scan is so broad that we can't tell the exact composition of GaN and InN. For growth rate 486 nm/hr, the curve emerges as single peak, although line width is still too broad. As growth rate increases to 962

nm/hr, the width of this peak becomes narrower. The details of growth rate depend on the structural and electric properties discussed in section 5.6.

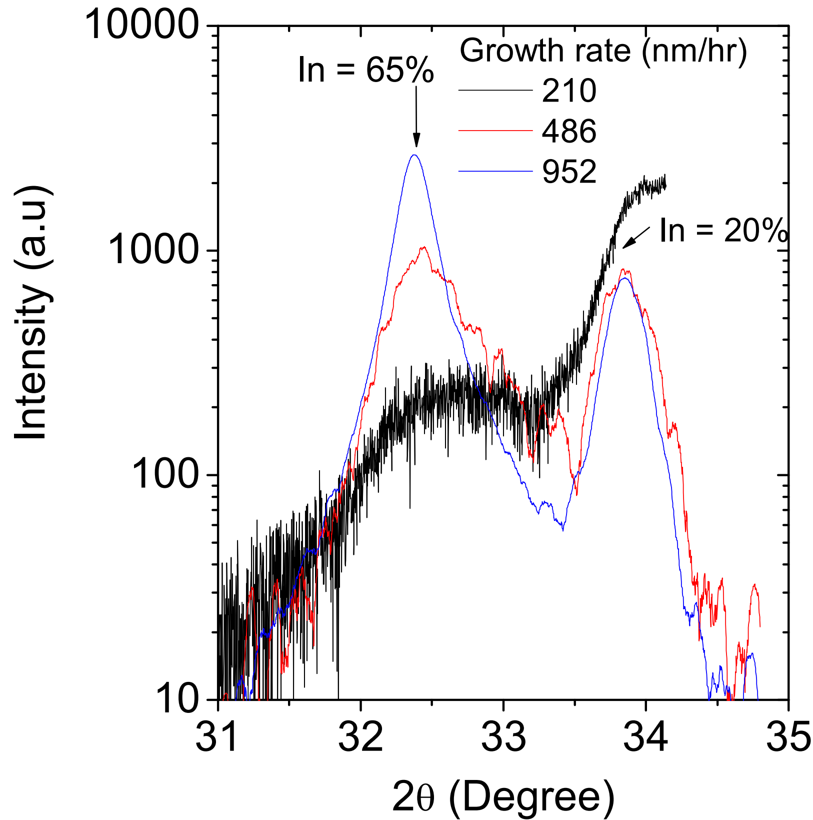

Figure 5.4 ω-2θ x-ray diffraction spectra of (002) plane of $In_{0.65}Ga_{0.55}N$ alloys grown at different growth rate G_R.

5.2.3. Low growth temperature

InGaN alloys of higher In contents have to be synthesized at a much lower growth temperature $T_G \sim 600$ °C (T_G for GaN ~ 1000 °C) by MOVCD) to avoid InN decomposition, phase separation, and In droplets. The evidence of phase separation and In metal droplets on the surface grown at higher T_G is shown in Fig. 5.5. The ω-2θ scan of (002) plane for $In_{0.65}Ga_{0.35}N$

alloys at different growth temperatures shows that phase separation and In droplets can be suppressed or removed by lowering the growth temperature.

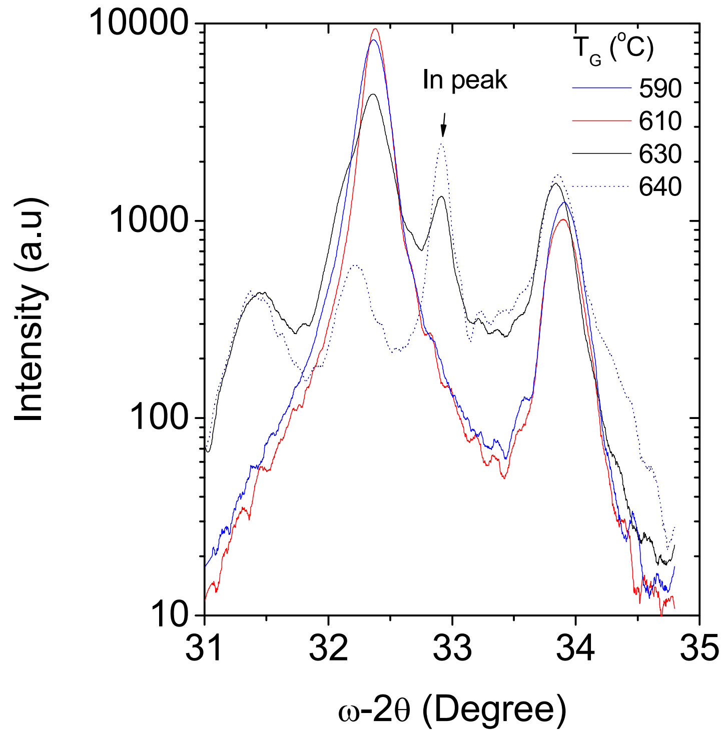

Figure 5.5 XRD ω-2θ spectra of (002) plane of $In_{0.46}Ga_{0.54}N$ alloys grown at different growth temperature T_G.

5.3. Growth and characterization of single phase InGaN alloys

InGaN alloys are of great interest because of their tunable direct band gap that spans from the infrared region of ~0.7 eV (InN) to the UV region of ~3.4 eV (GaN) [3-5, 140]. In particular, high quality In-rich InGaN alloys offer potential applications in many important areas including high efficiency homo- and multi-junction solar cells [12], direct hydrogen generation from aqueous solution of water by photoelectrochemical effect [48,141], super bright solid state

lighting (Light emitting diodes and laser diodes) [3], and thermoelectric (TE) power generation and/or solid-state cooling [142].

$In_xGa_{1-x}N$ alloys of thickness ~200 nm with different In contents were grown on GaN/Al_2O_3 and AlN/Al_2O_3 templates by MOCVD. The precursors were trimethylgallium, trimethylindium, and ammonia (NH_3) for Ga, In, and N, respectively. The growth pressure was 100 torr. The In content was controlled by growth temperature. In order to increase the In content from 25% to 63%, the growth temperature was decreased from 730 to 610 °C, while all other conditions were kept the same.

GaN/Al_2O_3 or AlN/Al_2O_3 templates were preheated in NH_3 environment prior to growth. There were no intermediate or buffer layers between the templates and InGaN epilayers. In content in InGaN was estimated from the peak value of x-ray diffraction (XRD) spectra of (002) reflection peak in ω-2θ scan mode and applying Vegard's law. The thicknesses of the films were obtained from *in situ* interference measurements during epigrowth. Electrical properties and surface morphology were probed by Hall-effect and atomic force microscopy (AFM) measurements.

In content and growth rate of InGaN alloys as functions of growth temperature,T_G are shown in Fig.5.6. Both the growth rate and In content increase linearly as T_G decreases. The linear relation between T_G and amount of In incorporation eases the engineering process of InGaN/GaN heterostructures and quantum wells for device applications. We also observed that In-incorporation can be increased by increasing growth rate, growth pressure, and flow rate of TMIn. However, the effectiveness of these parameters was found to be less pronounced than T_G.

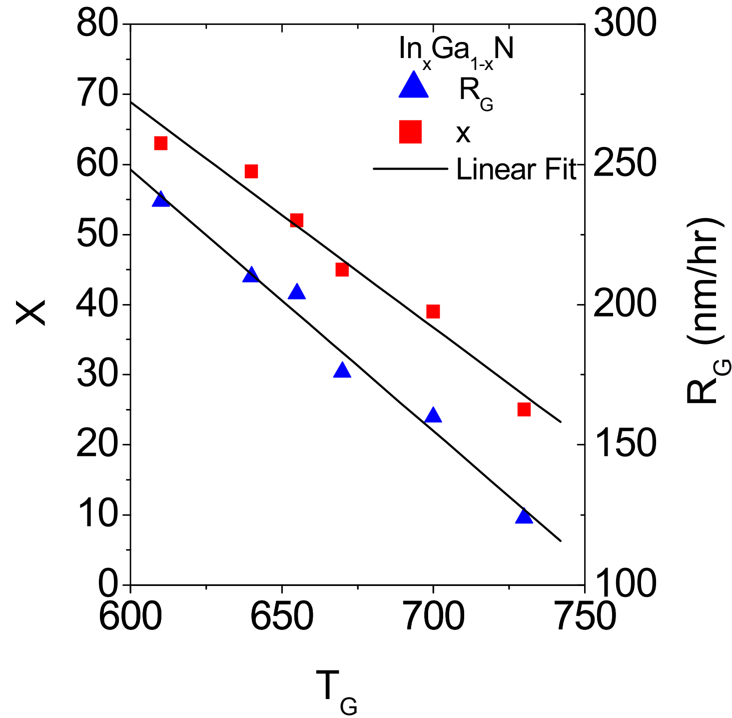

Figure 5.6 In composition (x) and growth rate (R_G) of $In_xGa_{1-x}N$ alloys as functions of growth temperature (T_G). Solid lines are linear fit of data.

Figures 5.7 (a) and (b) show the XRD (002) ω-2θ spectra of $In_xGa_{1-x}N$ alloys grown on GaN/Al_2O_3 templates in linear and semi-log scales, respectively. All curves, scanned down to InN peak position, have no multiple peaks, as seen by other authors with lower In content (<30%) [51,143], which implies that InGaN alloys are not phase separated.

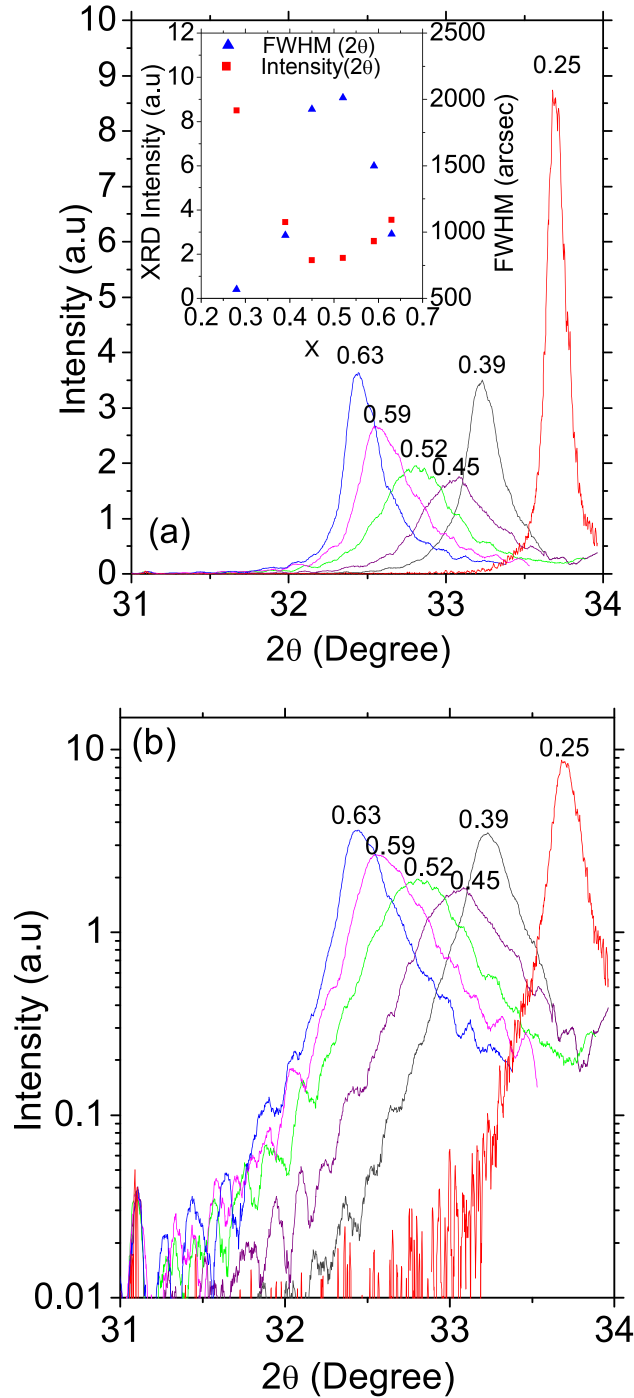

Figure 5.7 XRD ω-2θ curves of (002) planes of $In_xGa_{1-x}N$ alloys grown on GaN/Al_2O_3 templates (a) in linear scale and (b) in semi-log scale. The inset shows the full width at half maxima FWHM) and relative intensities as functions of In content. In contents # are also indicated in the figures.

The attainment of single phase InGaN alloys inside the previously thought miscibility gap by MOCVD here may be attributed to: 1) the presence of strain between the InGaN thin films and the templates since we grew InGaN directly on the templates without any buffer or intermediate layer to release it, 2) non-equilibrium growth processes taking place in epitaxial growth techniques like MOCVD, and 3) relatively low growth temperatures. The effect of these conditions and evidences of phase separation suppression methods are already discussed in section 5.2. The inset of Fig. 5.7 (a) shows the intensity and full width at half maximum (FWHM) of ω-2θ curves as functions of In content in InGaN alloys. The FWHM is found to be varied between ~570 and 2000 arcsec and anti-correlated with the intensity; the higher the XRD intensity, the smaller the FWHM and vice versa. The FWHM of the ω-2θ curves depends on many factors, including the homogeneity of the solid solution. We found that the homogeneity is quite good except the region where In content lies between 45% and 55%.

XRD (002) rocking curves of InGaN alloys and the variation in rocking curve FWHM with In content in InGaN are shown in Figs. 5.8 (a) and (b), respectively. Figure 5.8 (b) shows that FWHM increases as In content increases. Broadening of the FWHM of rocking curves with In content is due to the increased lattice mismatch with GaN. We also found that the FWHM decreases as the thickness of the InGaN layer decreases. The smallest value of FWHM of XRD (002) rocking curve was found to be associated with $In_{0.45}Ga_{0.55}N$ alloy (~ 60 nm thick), which is about 600 arcsec with optimized growth conditions.

Figure 5.9 (a) shows the AFM images of $In_xGa_{1-x}N$ alloys grown on GaN/Al_2O_3 templates for $0.25 \leq x \leq 0.63$ with a scanning area of (10×10) μm^2. The surface roughness, quantified by the root-mean-square (RMS) values, against the In content is plotted in Fig. 5.8 (b). It was found that RMS increases from 1.5 to 4.0 nm as x increases from 0.25 to 0.59. No In

droplets on the surface were observed in any samples we examined. We found similar surface morphologies of samples grown on AlN/Al_2O_3 templates as well.

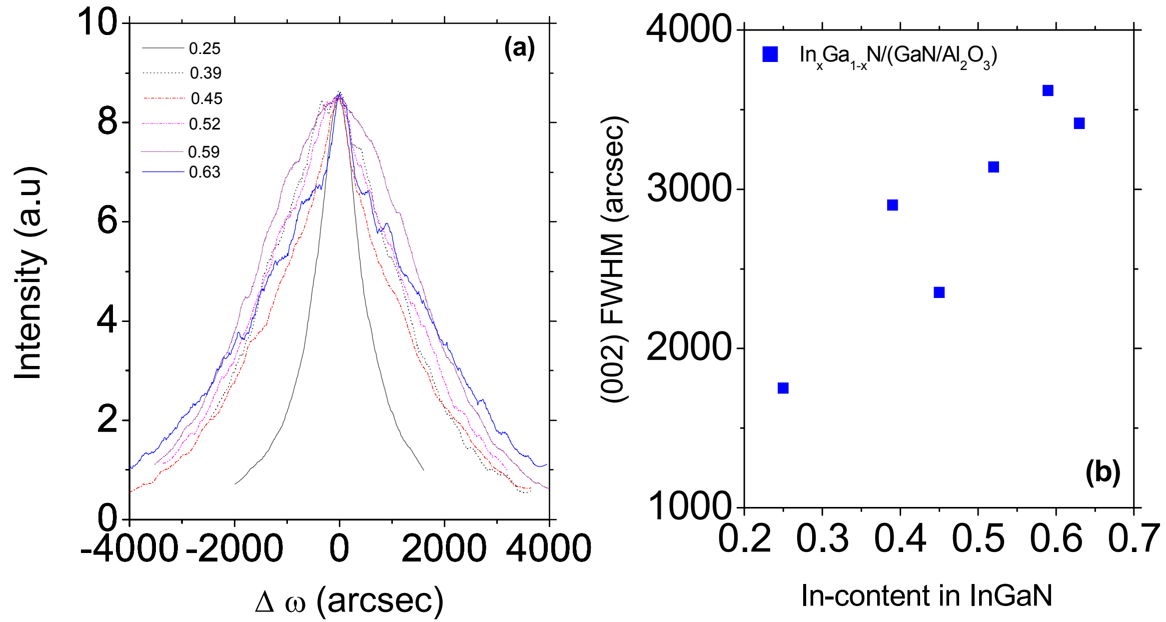

Figure 5.8 (a) XRD (002) rocking curves for different InGaN alloys and (b) variation of FWHMs as a function of In content in $In_xGa_{1-x}N$ alloys.

In order to evaluate the electrical properties, we grew InGaN alloys on AlN/Al_2O_3 templates. These structures make the electrical measurements straightforward, quick, and precise because AlN is highly insulating. Compositional dependence of Hall mobility (μ) and free electron concentration (n) of InGaN alloys with In content are plotted in Fig. 5.10. It was observed that both μ and n increase as In content increases and n lies between (1.9–3.4) $\times 10^{19}$ cm^{-3} while μ increases sharply as In mole fraction increases from 0.25 to 0.55. The reason for increasing μ with increasing In content could be the lower effective mass of the electrons

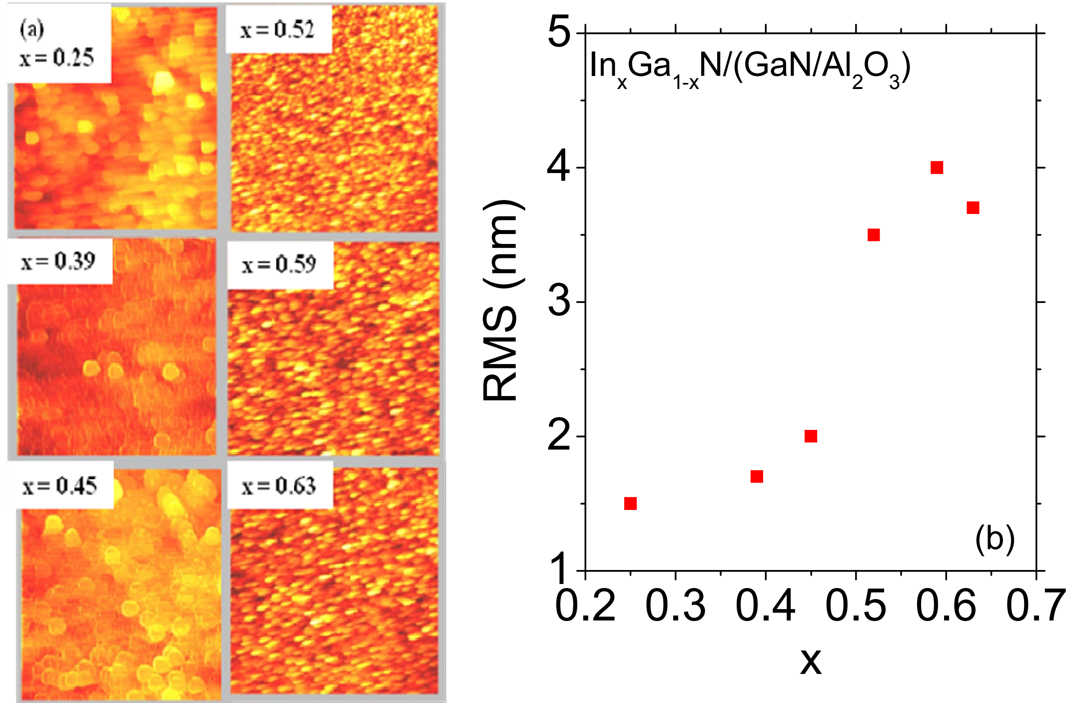

Figure 5.9 (a) AFM images and (b) surface roughness (RMS) as functions of In content in $In_xGa_{1-x}N$ alloys.

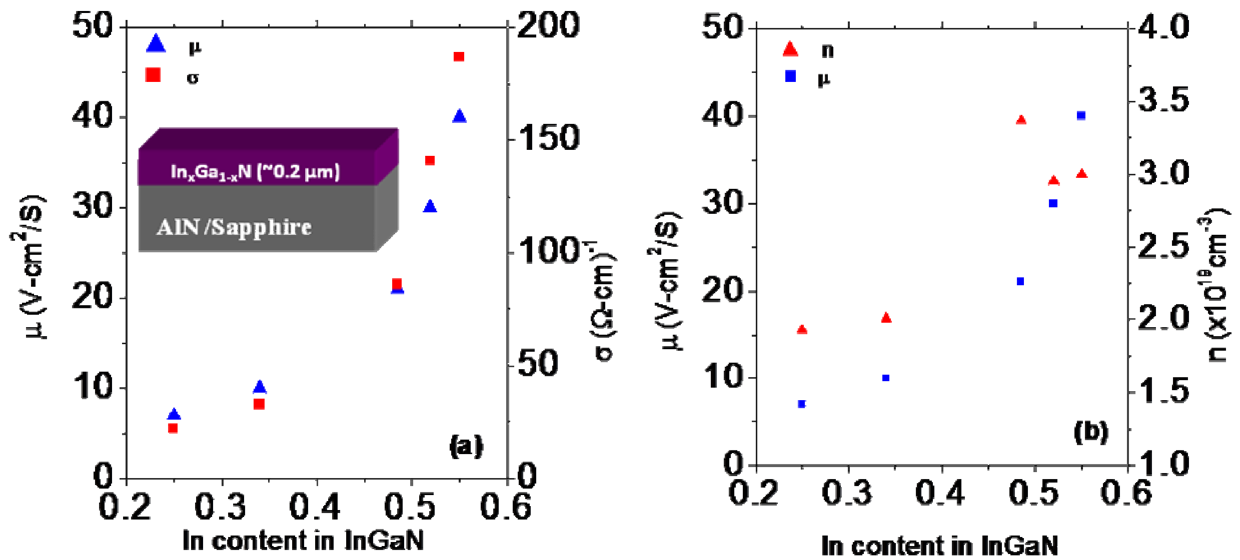

Figure 5.10 (a) Hall mobility and (a) electron concentration as functions of In content in $In_xGa_{1-x}N$ alloys. The layer structure employed for this study is shown in the inset of (a).

The room temperature electron mobility of $In_{0.55}Ga_{0.45}N$ alloys is about 40 cm^2/Vs and pure InN is as high as 1400 cm^2/Vs [122].

In conclusion, we have synthesized InGaN alloys without phase separation inside the previously thought miscibility gap by MOCVD. We believe that the presence of strain, nonequilibrium nature of epitaxial growth process, and low growth temperatures have promoted the suppression of phase separation. The structural properties, electrical properties, and surface morphology studies indicated that InGaN alloys in this previously thought miscibility gap region possess reasonably good quality. Further improvement in material quality is expected by optimizing other growth parameters.

5.4. Correlations between growth rate phase separation/suppression and film quality of $In_{0.65}Ga_{0.35}N$ alloys.

As discussed in section 5.1, high In-content InGaN alloys have attracted considerable attention as photonic and energy materials. The growth of such high In content alloys inside the previously thought miscibility gap region has proved to be very challenging. Nakamura *et al* [3] has shown experimentally that the quality of InGaN films can be improved by reducing the growth rate in low In content region. However, we found that such low growth rate for relatively higher In content resulted in phase separation and poor electrical and structural properties. Here, we discuss the effect of growth rate on phase separation/suppression, structural and electrical properties of $In_{0.65}Ga_{0.35}N$ alloys.

$In_{0.65}Ga_{0.35}N$ alloys were grown on AlN/sapphire template by MOCVD. A thin $In_{0.2}Ga_{0.8}N$ buffer layer (~20 nm) was gown before the growth of this layer. Trimethylgallium(TMGa), trimethylindium (TMIn), and ammonia (NH_3) were used for Ga, In,

and N sources. Growth temperature and pressure were fixed at 610°C and 500 torr. Growth rate was increased by increasing flow rate of group III sources, while keeping ammonia and In/Ga ratio the same. Electrical and structural properties were studied by Hall-effect and x-ray diffraction (XRD).

Figure 5.11 (a) show the ω-2θ scan XRD curves for (002) plane. In content in InGaN were determined from the peak angle using the Vegard law. In the figure, right peaks correspond to InGaN buffer layer while left peaks are from top InGaN layer. In content in buffer and top layer is found to be ~20% and 65% respectively. The figure clearly shows that as growth rate (R_G) increases, phase separation suppression occurs, which yields the single peaks for top $In_{0.65}Ga_{0.35}N$ layers. Figure 5.11(b) shows that In incorporation remains almost same with the wide range of G_R.

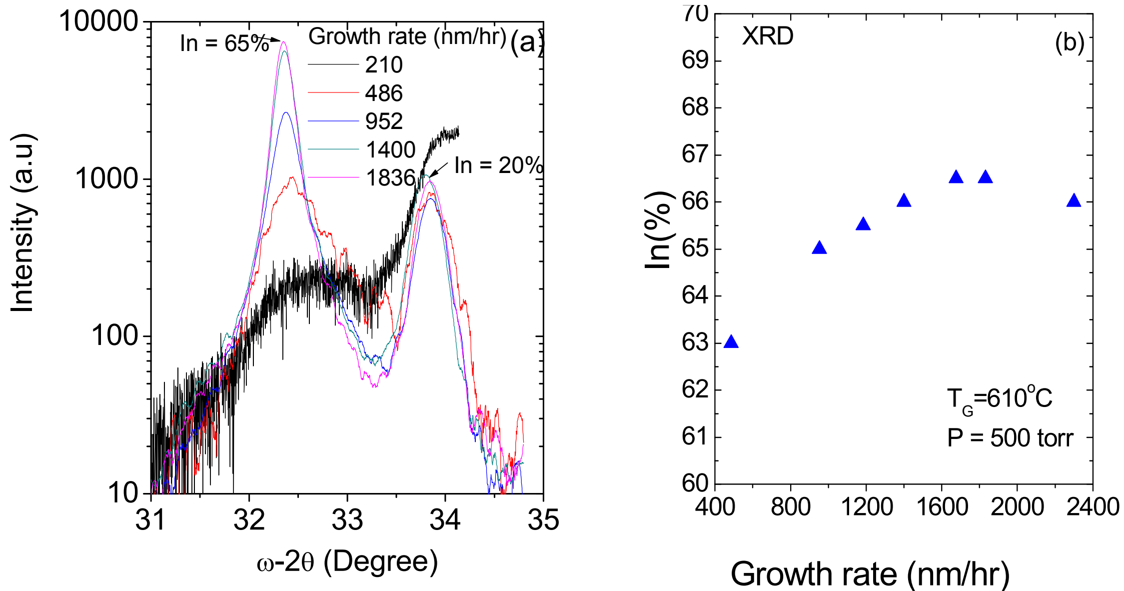

Figure 5.11 (a) XRD spectra of (002) ω-2θ scan of $In_{0.65}Ga_{0.35}N$ alloys at different growth rate R_G, (b) In content as a function of growth rate G_R with fixed growth temperature T_G and pressure P.

Growth rate (R_G) dependence structural properties are shown in Fig 5.12 (a) and (b). It has been found that as R_G increases, full-width at half maximum (FWHM) decreases and intensity increases for both ω-2θ and ω-scans (rocking curve). FWHMs of ω-2θ/ω scans decreased from ~2300/11000 to ~700/3700 arcsec when R_G increased from ~ 480 to ~1400 nm/hr. Further increases in R_G only moderately improve the film's quality.

Electrical properties of $In_{0.65}Ga_{0.35}N$ alloys as a function of growth rate are shown in Fig. 5.13. The result denotes that electron mobility (μ) increases as growth rate (R_G) increases. μ has increased almost linearly as G_R increased until it is ~1200 nm/hr and remains almost the same for further increase of G_R . We have observed a direct correlation between XRD and Hall results such that both are improving with increasing G_R. Mobility has increased by more than a factor of two when growth rate has increased from 210 to 1400 nm/hr while background concentration of electron remains the same, although very high. The origin of such a high n (~$3x10^{19}$ cm^{-3}) is still an unsolved issue. Impurities such as hydrogen, oxygen and nitrogen vacancy are thought to be responsible for such high n. However clear evidence from the experiment has yet to be achieved as single phase InGaN with this In content has not been achieved in the past. Better control of n and understanding of its origin could be achieved by detail dependence of growth parameters such as V/III ratio, pressure, temperature etc and strain management.

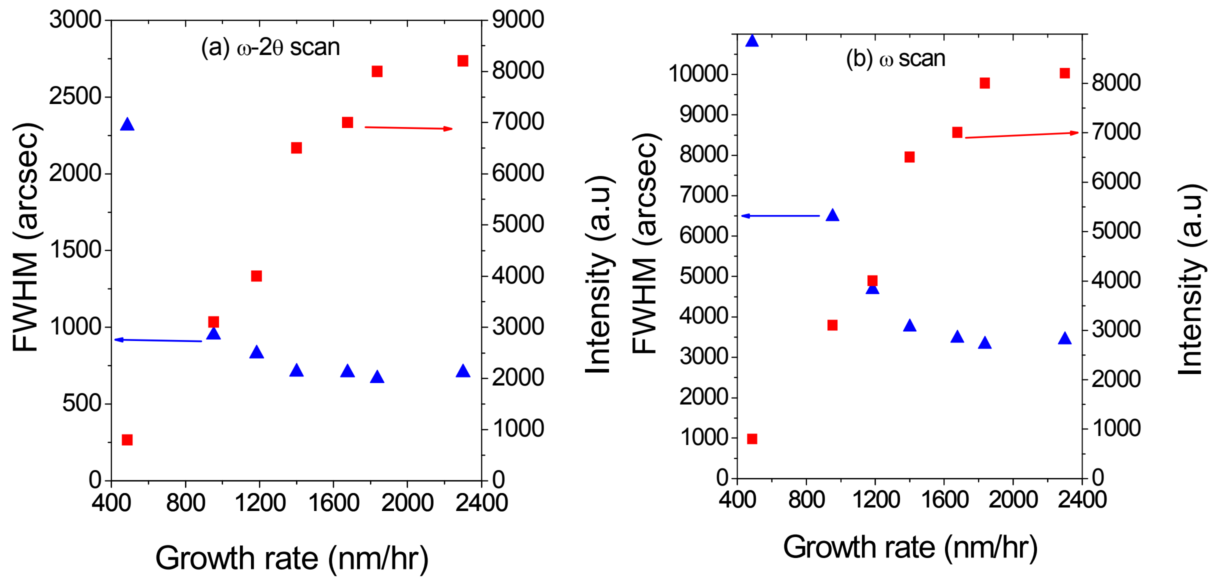

Figure 5.12 FWHMs and intensity of XRD spectra of (002) (a) ω-2θ scan (b) ω-scans of $In_{0.65}Ga_{0.35}N$ alloy as functions of growth rate, R_G.

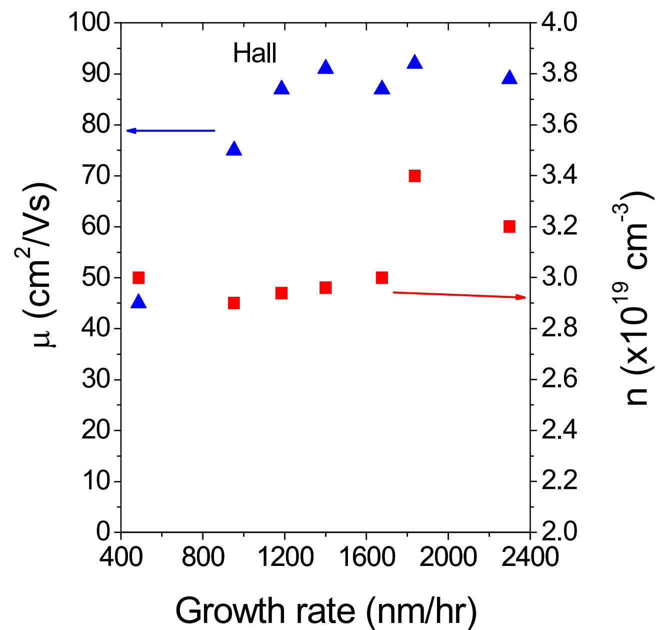

Figure 5.13 Hall mobility of electrons μ and background electron concentration n of $In_{0.65}Ga_{0.35}N$ alloy as functions growth rate G_R.

In summary, we have systematically investigated the effect of growth rate on phase separation/suppression and material quality of $In_{0.65}Ga_{0.35}N$. We found that as growth rate increases phase separation/suppression removes/occurs and material quality improves. With this and our previous work [8], we have established that an effective way to remove the phase separation and improve the material quality of InGaN alloys inside the theoretically predicted miscibility gap region is to grow it far away from thermodynamically equilibrium condition and higher growth rate would be such a condition. The optimization of other growth parameters and strain managements require further study.

CHAPTER 6- Synthesis of p-type InGaN alloys for longer wavelength emitters

6.1. Introduction

InGaN based laser diodes (LD) have attracted tremendous attention as a light source for high density optical data storage and RGB applications (full color display, laser TV, and cell phone projector etc). In 2000, commercial application of InGaN based ultraviolet (UV) LDs has started for optical data storage and Blu-ray Disc (Sony) using an emission wavelength of 405 nm. It took several years to extend wavelengths from 405 nm to 450 nm. Sample LDs with emission wavelengths up to 493 nm are now available in the market (Source: Nichia Corporation). In recent years, tremendous progress has been made by several research groups to extend wavelengths to the pure green region for RGB applications [152-156]. The longest wavelength of InGaN based LDs reported so far has a wavelength of 531nm [157].

The technological challenges for pure green InGaN based LDs are the growth of high quality high In-content InGaN quantum wells (QWs) with optimized InAlGaN cladding and wave guiding layer designs. As discussed in chapter 5, high quality In-rich InGaN alloys are very difficult to grow due to the solid phase miscibility and high density of dislocations. Furthermore, since the growth temperature of InGaN QWs is much lower than that of GaN or AlGaN, subsequent growth of high temperature layers deteriorates the material quality of InGaN due to the decomposition of InN. Another difficulty in obtaining longer wavelength emitters is the quantum confined stark effect (QCSE) which normally occurs due to polarization related fields. The QCSE reduces the overlap between the electron and hole wave functions in the QWs, limiting their radiative recombination efficiency and leading to a blue-shift in peak emission

wavelength with increasing current injection [158, 159]. To overcome this effect, non-polar or semi-polar GaN bulk substrates have been studied extensively in the recent years [160]. In this section, we discuss the growth and characterization of III-nitride based LD structures in the emission wavelength of ~ 500 nm.

6.2. Basic working principle of semiconductor LDs

Semiconductor LD is a p-i-n diode. In semiconductor LDs, the direct band gap semiconductor serves as a gain medium while polished facets provide optical feedback (by forming a resonant cavity). Electric current under forward bias conditions is the source of pumping. Figure 6.1 below shows a schematic illustration of how charge carriers and optical modes can simultaneously confine in a semiconductor LD structure. The active layer has a lower band gap and a higher refractive index than those of the p-and n-type materials.

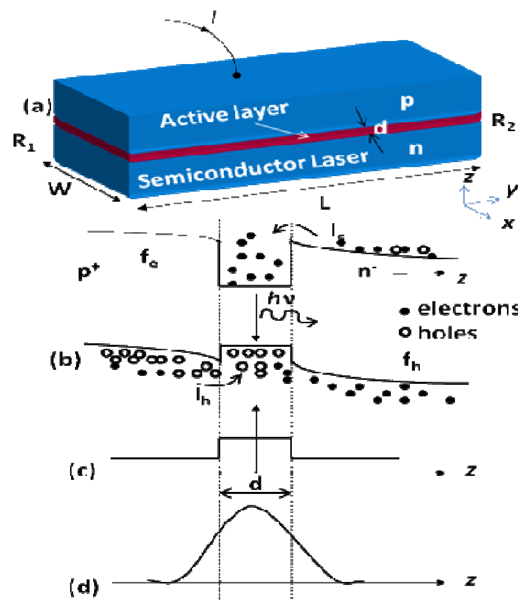

Figure 6.1 Schematic illustration of a typical (a) LD structure, (b) band structures, (c) refractive index profile for wave guiding, (d) Intensity profile of optical mode.

6.3. InGaN based green LDs

The LD structures were grown by MOCVD on c-plane n-GaN/AlN/Al_2O_3 templates. InGaN double quantum well (DQW) LD structures consists of a 0.6-μm-thick Si-doped n-type $Al_{0.14}Ga_{0.86}N$ (2 nm)/GaN (2 nm) supperlattice (SL) n-cladding layer, a 0.1-μm-thick Si-doped n-type GaN guiding layer, a 0.05-μm-thick $In_{0.03}Ga_{0.97}N$ transition layer, an $In_{0..3}Ga_{0.7}N$/ $In_{0.03}Ga_{0.97}N$ DQW structures consists of two 3-nm-thick un-doped $In_{0.3}Ga_{0.7}N$ well layers forming the gain medium separated by 8-nm-thick un-doped $In_{0.05}Ga_{0.95}N$ barrier layers, a 20-nm-thick Mg-doped p-type $Al_{0.2}Ga_{0.8}N$ electron blocking layer (EBL), a 0.1-μm-thick Mg-doped p-type GaN guiding layer, a 0.5-μm-thick Mg-doped p-type $Al_{0.14}Ga_{0.86}N$ (2 nm)/GaN (2 nm) SL p-cladding layer, and a 0.1-μm-thick Mg-doped p-type GaN contact layer. The layer structure and electronic band diagram are shown in Fig. 6.2.

Grown wafers were tested in a probe station under forward bias conditions and 20 mA dc currents for first order information about light output, EL spectra, and I-V characteristics. Growth conditions were then optimized accordingly. A microscopic image of a light emitted wafer and corresponding EL spectrum are shown in Fig 6.3 (a) and (b). The peak emission wavelength was ~ 500 nm.

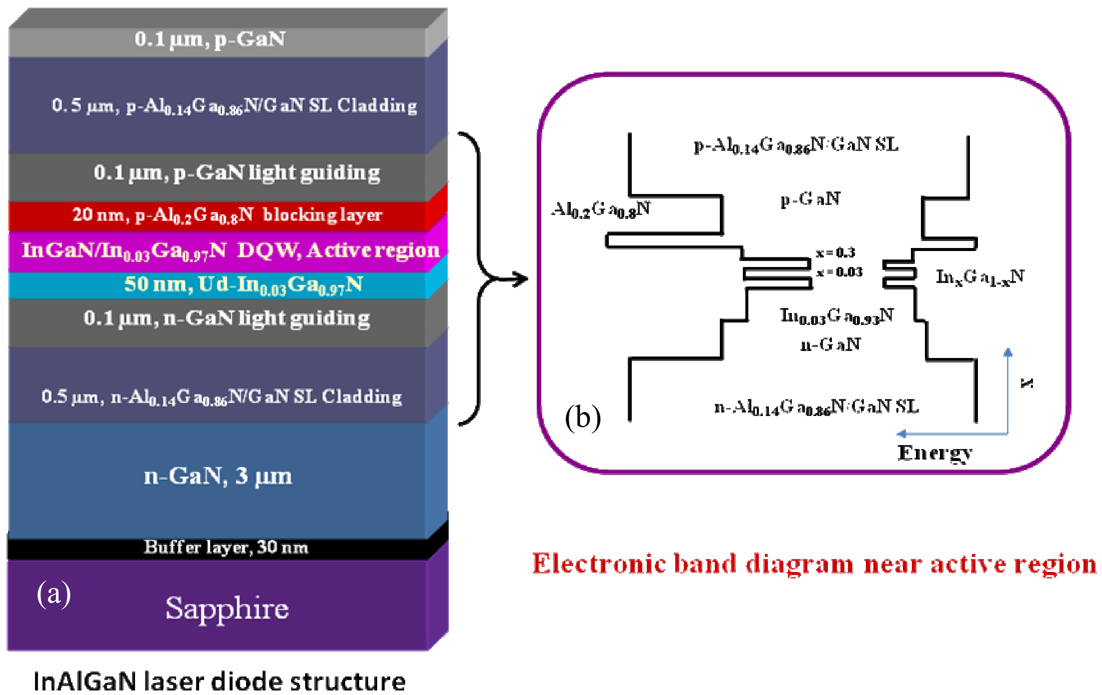

Figure 6.2 (a) LD structure for 500 nm laser diode and (b) electronic band diagram near active region.

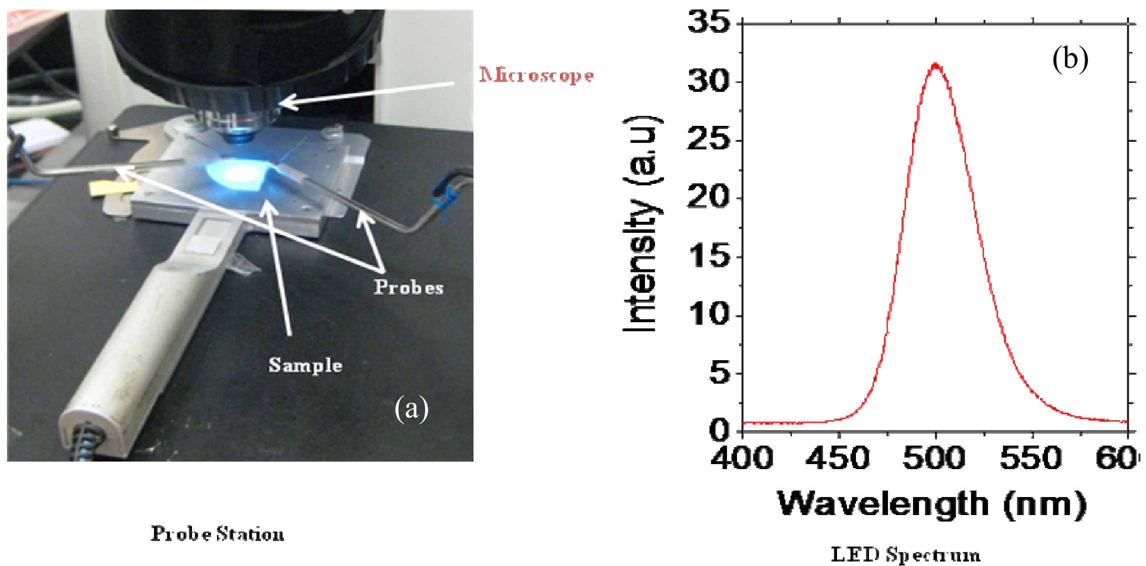

Figure 6.3 (a) Probe station where LD structure is emitting light under the forward bias @ 20 mA dc current and (b) EL spectrum showing peak emission wavelength ~ 500 nm.

The LD fabrication process consists of the following steps. First, ridge area was defined by photolithography. This was followed by partial dry etching of about ~ 0.2 µm of the p-layer. Then, the n-GaN contact layer was exposed by etching. About 300 nm of SiO_2 was deposited using plasma enhanced CVD. Photolithography, and selective area wet etching of SiO_2 were used to open the window for n-and p-contact metal depositions. For the p-contact, Ni/Au (30/200 nm) and for n-contact, Ti/Al/Ni/Au (30/120/30/120 nm) were deposited using e-beam evaporator. Finally, the waveguide cavity was formed by polishing the facets. TiO_2/SiO_2 DBR was formed for reflecting mirrors. The schematic of the fabricated laser structure is shown in Fig. 6.4.

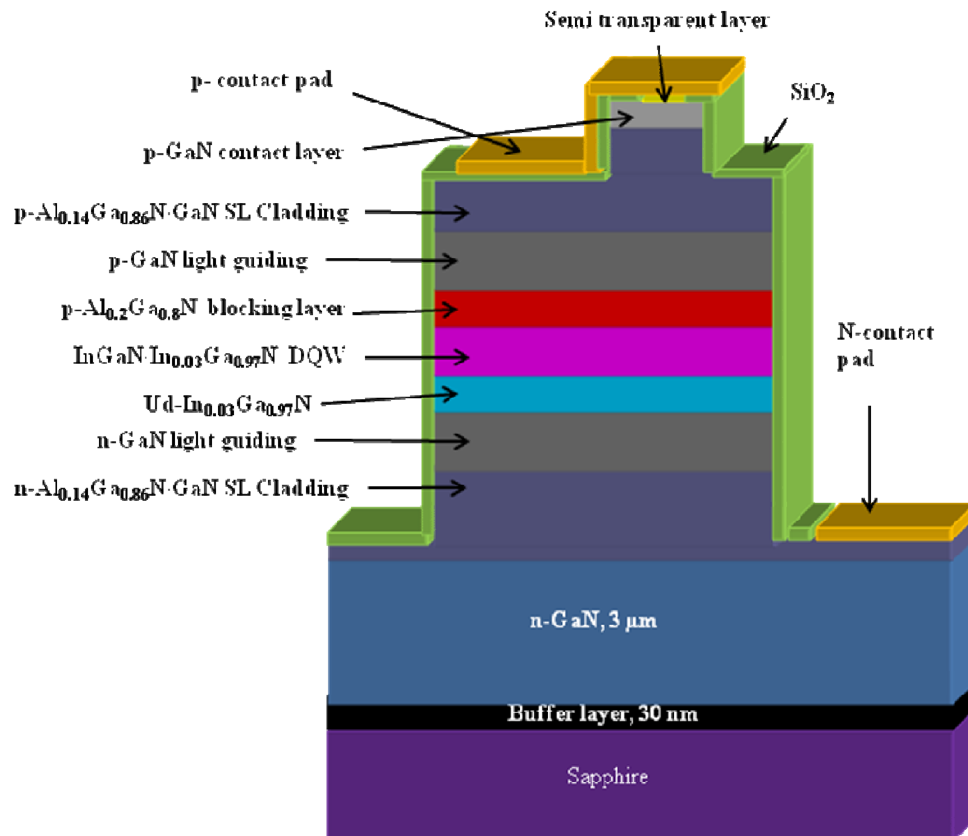

Figure 6.4 Schematic of a fabricated ridge waveguide laser diode grown on sapphire substrate.

I-V and L-I characteristics of fabricated devices are shown in Fig. 6.5 (a) and (b), respectively. High breakdown voltage *V* could be related to the relatively high p-type contact resistance and resistivity of the p-type material itself. The L-I curve as shown in Fig. 6.5 (b) was measured under pulse current injection (duty cycle = 0.1%). Current densities as high as 25 kA/cm^2 were injected; however, at this point, we could not achieve lasing. A high density of dislocations and relatively low p-type GaN hole concentration might be the reasons lasing were not achieved from this InAlGaN LD structure.

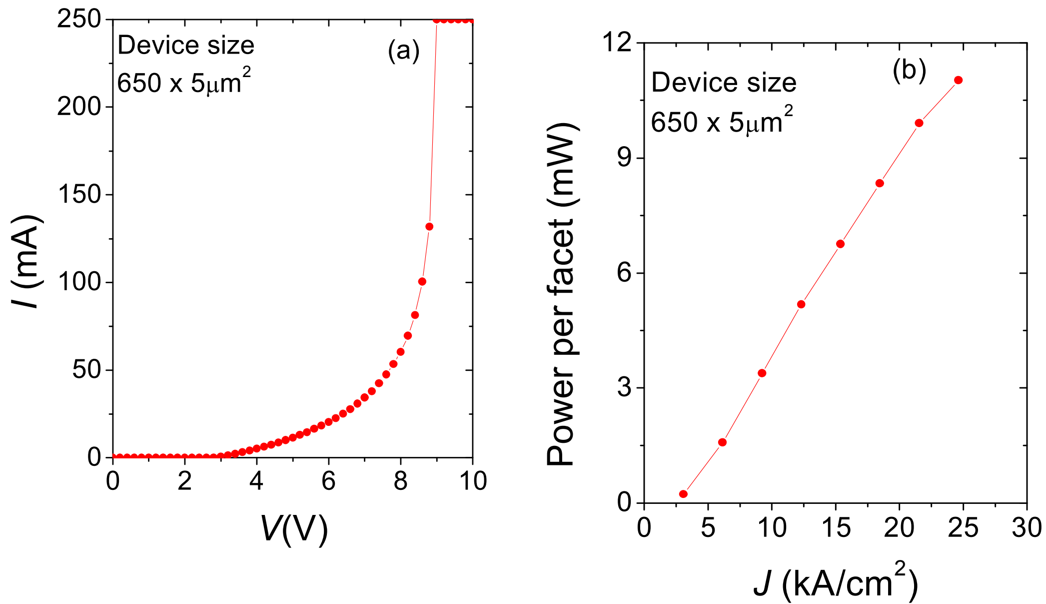

Figure 6.5 (a) I-V and (b) L-I characteristics of a fabricated LD device.

In summary, we have synthesized, fabricated, and characterized the InAlGaN LD structure but no lasing has been achieved, although very high current density can be injected into the device. To achieve lasing, we need to reduce the number of dislocations, improve the conductivity of p-type material, etc. Use of high quality, low dislocation bulk GaN as substrates for the growth of LD is one of the best options for reducing dislocations while p-type InGaN can

be adopted to reduce the contact resistance and increase the hole injection in the active region. The synthesis of low resistive p- type InGaN alloys and their properties are discussed in section 6.4.

6.4. Electrical and optical properties of Mg-doped $In_xGa_{1-x}N$ ($0 \leq x \leq 0.35$) alloys

P-type GaN was thought impossible for a long time until Amano *et al*. in 1989 realized it via Mg doping and post-growth low-energy electron-beam irradiation (LEEBI) treatment [27]. Hole concentration and the lowest resistivity they found were 10^{17}cm^{-3} and 12 Ω-cm respectively. Later Nakamura *et al.* discovered that post growth thermal annealing in hydrogen free ambient is the most effective and reliable method of achieving p-type GaN [28]. Since then, thermal annealing is established as a standard method to achieve p-type conductivity in MOCVD grown Mg-doped GaN. The reason for annealing or LEEBI treatment is now well understood. Mg forms Mg-H complexes during growth, which makes Mg doped GaN insulating. After LEEBI treatment or annealing, the dissociation and removal of H from electrically inactive Mg-H complexes takes place, leaving Mg free. The binding energy of the donor or acceptor can be described by modifying the equation for the binding energy of an electron bound to a proton (a hydrogen atom). Replacing free electron mass and the dielectric constant with the effective mass m^* of the electron or hole and the relative dielectric constant ($\varepsilon_r = \varepsilon/\varepsilon_o$) of the semiconductor respectively, one can roughly estimate the donor/acceptor binding energy (E_A for acceptor and E_D for donor) using the following equation [74],

$$E = \frac{m^* e^4}{2(4\pi\varepsilon_r\varepsilon_o\hbar)^2} \quad (6.1)$$

Applying Eq. (6.1) to GaN, we find a value of E_A = 1 90 meV for p-type GaN. Experimental values are also close to this number (150-200 meV) [161-163]. This relatively large binding energy (large compared to k_BT at room temperature) is due to the large hole mass and the low dielectric constant of GaN. Because the E_A of Mg-acceptor is so deep, only about 1% of all Mg impurities occupying proper group III lattice sites are thermally ionized at room temperature. Hydrogen passivation or compensating native donor-like defects, such as N vacancies, can further reduce the concentration of active Mg-acceptors. Therefore, high free hole concentrations in GaN are difficult to achieve, even with high acceptor concentrations. To attain the desired hole concentration, it is necessary to be able to incorporate extremely large dopant concentrations in excess of 10^{20} cm^{-3}, which is detrimental for hole mobility (~10 cm^2/Vs) and crystalline quality. The limited free hole concentration coupled with the low hole mobility results in p-type GaN with relatively low conductivity compared to other semiconductor materials. In InGaAlN systems, effective hole mass decreases and dielectric constant increases as band gap decreases, so one can expect lower E_A of Mg-accepter in Mg-doped InGaN as compared to that in Mg-doped GaN and AlGaN.

Since E_A decreases as band gap decreases [163], Mg-doped InGaN (InGaN:Mg) would result in a higher hole concentration (p) at room temperature compared to Mg-doped GaN. On the other hand, use of p-type InGaN (which is synthesized at much lower temperature compare to that of p-type GaN in MOCVD process) instead of p-type GaN is beneficial, particularly in devices such as LDs, long wavelength emitters, and solar cells where the active region has to be grown at temperatures much lower than that of the top p-type GaN layer. Low etching damage and low contact resistance are other characteristics of p-type InGaN that are superior to those of p-type GaN [161]. Improvements in the performance of GaN based devices using p-type InGaN

either as a contact layer or as the p-layer itself has already been demonstrated [164-166]. In recent years, applications of InGaN alloys are expanding from optoelectronics/photonics to hydrogen generation (from aqueous solution of water) and thermoelectric (TE) power generation [142, 167-169]. For hydrogen generation, p-type InGaN alloys are found to be more stable in aqueous solution. It is also a component of TE power generating devices (TE modules). For all these applications, high optical and electrical quality p-type InGaN is sought.

P-type doping in relatively high In content InGaN alloys is challenging due to the high background electron concentrations, which is believed to come from defects such as oxygen and hydrogen impurities or nitrogen vacancies [123, 124]. These nitrogen vacancies could be the result of an insufficiency of nitrogen atoms due to the low decomposition rate of ammonia as high In content InGaN has to grow at temperatures lower than $< 800\ ^{o}C$ (growth temperature of GaN is generally $> 1000\ ^{o}C$). Although synthesis of p-type InGaN has been reported as early as in 1995 [161], there are only few reports on p-type InGaN [161, 170-176]. Furthermore, use of high In content p-InGaN is inevitable in the future as nitride based devices are rapidly expanding towards longer wavelength emitters [8]. In this section, a systematic study of the electrical and optical properties of Mg-doped p-type $In_xGa_{1-x}N$ alloys, including E_A of Mg dopant, as a functions of x up to $x = 0.35$ is carried out . To the best of our knowledge, so far E_A of p-type $In_xGa_{1-x}N$ has only been reported up to $x = 0.17$ [174].

Mg-doped p-type $In_xGa_{1-x}N$ alloys ($0 \leq x \leq 0.35$) were grown on semi-insulating c-GaN/sapphire templates by MOCVD. Ammonia (NH_3), trimethylgallium (TMGa), trimethylindium (TMIn), and biscyclopentadienyl-magnesium (Cp_2Mg) were used as N, Ga, In, and Mg sources. N_2 gas was used as a carrier gas. Growth temperature was varied from 1050 to 740 ^{o}C to increase x from 0 to 0.35. A variable temperature Hall-effect experiment was

performed to measure hole concentration (p), hole mobility (μ_h), and resistivity (ρ) of the samples. Continuous wave (CW) photoluminescence (PL) spectra were measured using a Ti–sapphire laser spectroscopy system coupled with a super tripler, which gives an average output power of about 40 mW at 4.7 eV and a spectral resolution of about 0.2 meV. Indium content was determined from the peak angle of (002) ω-2θ curves of x-ray diffraction (XRD) and using the Vegard law.

Room temperature electrical properties of Mg doped p-type $In_xGa_{1-x}N$ alloys grown on semi-insulating c-GaN/sapphire templates (SI-GaN) as functions of x are plotted in Fig. 6.6. We have chosen SI-GaN templates to minimize the errors in electrical measurements of top Mg-doped InGaN alloys. Since p-type $In_xGa_{1-x}N$ layer is thin (~ 200 nm), resistivity of the underneath layer has to be high to assure accuracy of measurements. It was found that as x increases from 0 to 0.35, p continuously increases from 2×10^{17} for $x = 0$ (GaN) to 5×10^{18} cm^{-3} until $x = 0.22$. μ_h is found to decrease from 15 cm^2/Vs to 1.8 cm^2/Vs as x increases from 0 to 0.35. The variation in ρ with x shows that ρ decreases as x increases and reaches a minimum value of 0.4 Ω-cm at x = 0.22 ($In_{0.22}Ga_{0.78}N$). This value of ρ is among the smallest reported for p-type InGaN. Though even high p has been reported for similar In content InGaN [175], μ_h in our samples are much better and hence results in this record low ρ. High μ_h corresponds to the high quality of the material and low ρ will improve the device performance for many applications. Relatively higher ρ and lower p beyond x =0.22 in p-type $In_xGa_{1-x}N$ is due to the high compensation of Mg-acceptors with background electron concentration, which increases as x increases. This is the main hindrance of obtaining p-type conductivity to extend p-type InGaN alloys with even higher In content.

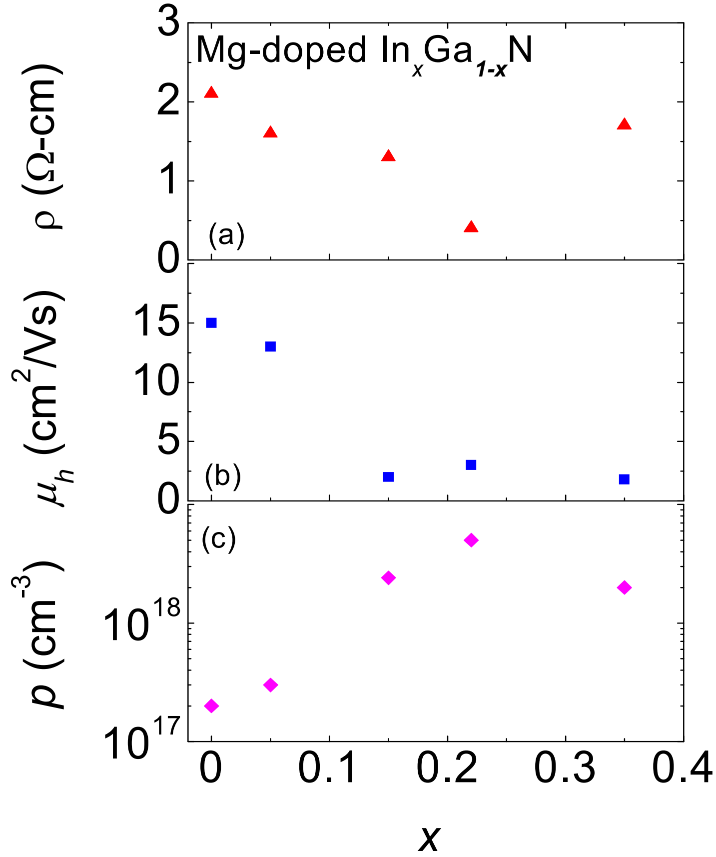

Figure 6.6 Room temperature (a) hole concentration p, (b) hole mobility μ_h, and (c) reistivity ρ as functions of In content x in Mg doped $In_xGa_{1-x}N$ alloys.

Temperature dependent p of p-$In_xGa_{1-x}N$ alloys were measured by Van dar pauw Hall measurements. Figure 6.7 is the Arrhenius plot of free hole concentration p for x = 0.05, 0.15, 0.22, and 0.35, respectively. Straight lines are the linear fits of the experimental data of p with following equation,

$$p = p_o\, e^{-\frac{E_A}{k_B T}}, \tag{6.2}$$

where E_A is Mg activation energy and k_B is Boltzmann constant.

The plot E_A as a function of x is shown of Mg doped $In_xGa_{1-x}N$ alloys in Fig. 6.8 along with other reported values [161, 174, 176]. It was found that E_A continuously decreases as x increases as expected. A lower value of E_A is the main reason that room temperature p increases as x increases. An E_A value as low as 43 meV was obtained in Mg-doped $In_{0.35}Ga_{0.65}N$ alloy, which is ~ 4 times smaller than that of Mg-doped GaN. This result indicates that one can get even better conductivity in p-InGaN if we could better control the background electron concentration. The issues of high background electron concentration in InGaN alloys with relatively high In content are currently under intensive investigation [123, 124] and significant improvements in p-type conductivity in relatively high In content $In_xGa_{1-x}N$ alloys are anticipated.

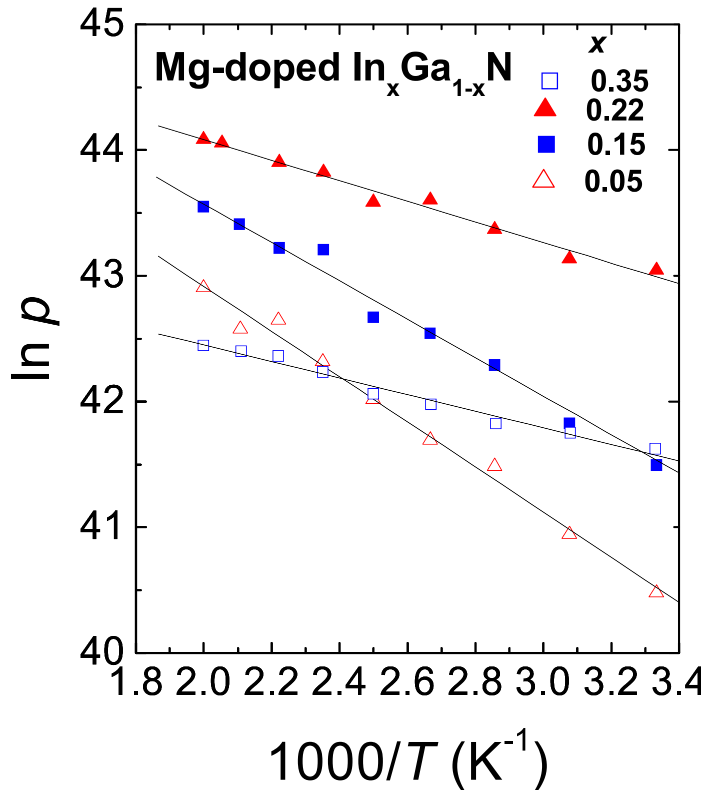

Figure 6.7 The Arrhenius plot of free hole concentration, p, in Mg doped $In_xGa_{1-x}N$ alloys.

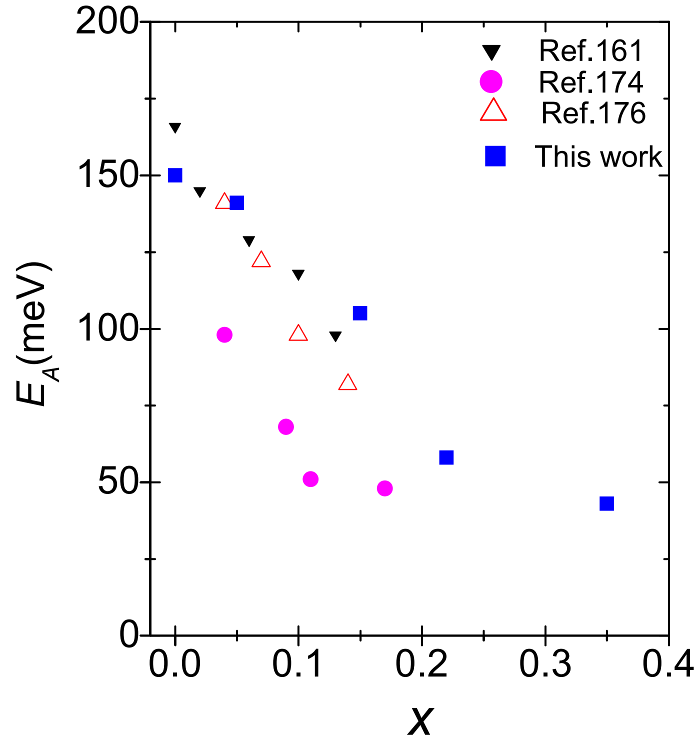

Figure 6.8 Energy level E_A of Mg acceptors in Mg doped p-$In_xGa_{1-x}N$ alloys as a function of In content x. Data from references available up to x = 0.17 are also included.

Fig. 6.9 shows low temperature (10 K) PL spectra of Mg-doped $In_xGa_{1-x}N$ for x = 0, 0.05, 0.11, and 0.22. We observed that the spectra of Mg-doped GaN is dominated by a broad emission band centered around 2.90 eV, which is a donor-acceptor-pair (DAP) type transition involving deep donor, D^o, and Mg acceptor, Mg^o. Deep donors appeared in Mg doped GaN but disappeared in all Mg doped InGaN alloys. One speculation is that the much lower growth temperature for InGaN alloys somehow suppresses the formation of these deep donors. Relatively weak features in the higher energy side with a peak at 3.29 eV is band-to-impurity type transition involving the conduction band, e^- and, Mg^o which is believed to dominate the spectra of Mg doped GaN with light or moderate doping. Except for Mg doped GaN samples, all Mg doped p-type $In_xGa_{1-x}N$ spectra show the dominant peak with the same mechanism as that of

3.29 eV line in Mg doped GaN. The feature of an emission line at 3.29 eV also appear in the spectra for samples with x=0.11, and 0.22. It is related to the GaN template, which is slightly doped with Mg to make it semi-insulating. From the PL peak positions observed here and the values of band-gaps reported already in the literature [123], we have estimated the acceptor level of Mg in our $In_xGa_{1-x}N$ epilayers, which is plotted in Fig. 6.10. As expected, Mg levels in $In_xGa_{1-x}N$ alloys are found to become shallower as In-content increasing.

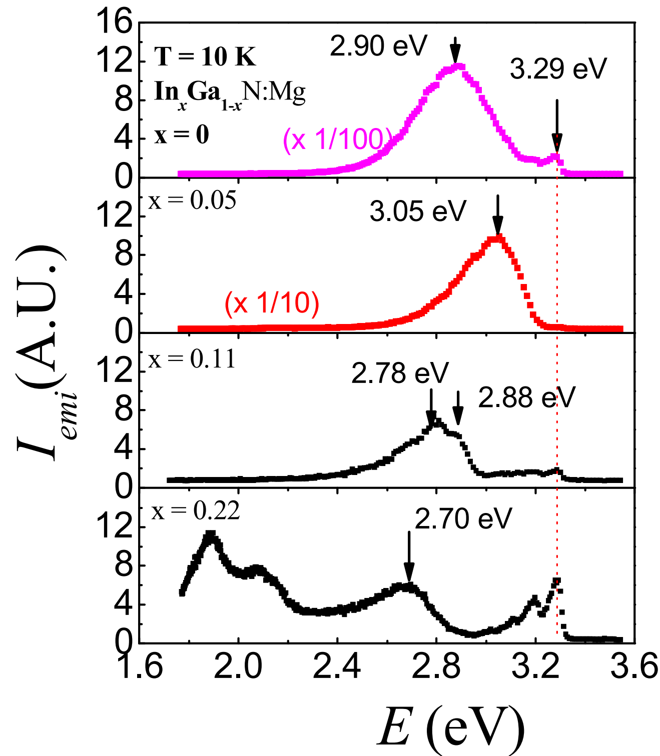

Figure 6.9 Photoluminance spectra of Mg-doped p-type $In_xGa_{1-x}N$ alloys measured at 10 K.

The band to Mg impurity related PL emission intensity from these epilayers is found to decrease exponentially as In-content increases. If we compare the PL emission intensity of Mg doped GaN with that of Mg doped $In_{0.22}Ga_{0.78}N$, it decreases by almost three orders of

magnitude, which is shown in Fig. 6.10. The reduction of PL intensity may partly be related with incorporation of impurities which are also responsible for high electron background concentrations in high In content InGaN alloys.

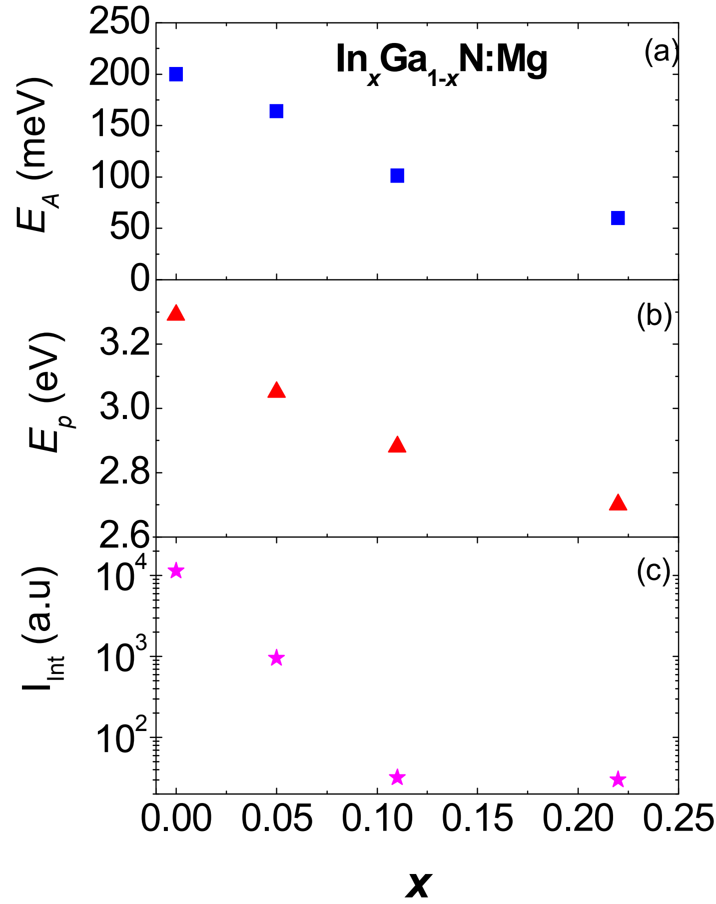

Figure 6.10 Integrated PL intensity, I_{int}, peak position of Mg related emission E_p, and Mg acceptor energy levels E_A as functions of In content x. (a) E_A, (b) E_p, (c) I_{int} (c).

In summary, we have synthesized the Mg-doped p-type $In_xGa_{1-x}N$ alloys for x up to 0.35 by MOCVD and analyzed their electrical and optical properties. P-type resistivity in Mg-doped InGaN alloys was found to be lower than that in Mg-doped GaN. Resistivity as low as 0.4 Ω-cm with a free hole concentration as high as $5x10^{18}$ cm^{-3} was measured in Mg doped $In_{0.22}Ga_{0.78}N$.

We have measured the E_A of the Mg acceptor in Mg-doped $In_xGa_{1-x}N$ alloys for x up to 0.35 using temperature dependent hole concentrations measured from Hall-effect experiments. E_A as low as 43 meV was obtained in Mg doped $In_{0.35}Ga_{0.65}N$. Using low temperature PL measurements, we found Mg acceptor levels for x up to 0.22, which is in close agreement with the E_A obtained from the electrical measurements. The difficulties of obtaining p-type InGaN in relatively high In-content is due to the high background election concentration as growth.

CHAPTER 7- General conclusions

III-nitride nanostructures and devices were synthesized by MOCVD. XRD, 3ω method, AFM, PL, Hall-effect measurements, etc were employed to characterize them.

Structural, optical, and optoelectronic properties of AlN epilayers have been studied extensively. These properties were found to be better in thicker AlN epilayers compared to those in thinner AlN epilayers. For a thick AlN epilayer (~ 4 μm), the FWHM of the rocking curves of the (002) and (102) reflections were as small as 63 and 437 arcsec, respectively. N_{screw} and N_{edge} for this film were estimated to be ~5×10^6 and ~2.5×10^9 cm^{-2}, respectively. 200 nm DUV photodetectors with outstanding characteristics were fabricated from the AlN MSM structure and it was shown that the dark current was significantly decreased in photodectectors with thick AlN epilayers. The results suggested that one effective way for attaining DUV optoelectronic devices with improved performance is to increase the thickness of the AlN epilayer template, which results in a reduction in TD density. Effects of Si-doping on the structural properties of AlN epilayers were also studied. Un-doped AlN epilayers were found to be under compressive stress while Si doped AlN epilayers above certain doping concentrations (N_{Si} = 5x10^{17} cm^{-3}) were under tensile stress. The most significant effect of Si-doping on structural properties was an increase of N_{screw}, indicated by the broadening of the symmetric rocking curves at all doping levels. DUV PL spectroscopy and XRD studies verified that AlN epilayers grown on sapphire substrates are under compressive stress while those grown on SiC and Si are under tensile stress. The stress-induced shift of the free exciton transitions in AlN epilayers grown on different substrates has been measured and correlated with XRD results, from which a stress-induced bandgap shift of 45 meV/GPa in AlN epilayers was deduced. These results established that PL is

another simple and effective method for monitoring the biaxial stress in AlN epilayers in addition to XRD measurements.

The potential of III-nitrides for thermopower generation (which is the least explored area in the field of nitride research) has been investigated. The TE properties of $In_xGa_{1-x}N$ alloys were found improve as In content increased. It was found that as In content increases, thermal conductivity decreases and power factor increases, which lead to an increase in the TE figure of merit (*ZT*). The value of *ZT* was found to be 0.08 at 300 K and reached 0.23 at 450 K for $In_{0.36}Ga_{0.64}N$ alloys. Also, the *ZT* values of $In_{0.36}Ga_{0.64}N$ alloy in the measured temperature range are comparable to those of the SiGe alloys, which is currently the prime TE material of choice for thermopower generation in high temperature environments such as in radio-isotope TE generators. Our results suggested that ZT would be even higher if In content in InGaN is increased further. For practical TE applications based on nitrides, we need to investigate the TE properties of p-type InGaN alloys because TE devices consist of p-type and n-type materials.

InGaN alloys without phase separation inside the theoretically predicted miscibility gap region are synthesized by MOCVD for photovoltaic and TE applications. We believe that the presence of strain, nonequilibrium nature of epitaxial growth process, and low growth temperatures have promoted the suppression of phase separation. The structural properties, electrical properties, and surface morphology studies indicated that InGaN alloys in this previously thought miscibility gap region possess reasonably good quality. Further, we have systematically investigated the effect of growth rate on phase separation/suppression and material quality of $In_{0.65}Ga_{0.35}N$ alloy. Crystalline quality and mobility were found improved as growth rate increased.

Mg-doped p-type $In_xGa_{1-x}N$ alloys for x up to 0.35 were synthesized by MOCVD for their applications in long wavelength emitters such as green LDs. P-type resistivity in Mg-doped InGaN alloys was found to be lower than that of Mg-doped GaN. Resistivity as low as 0.45 Ω-cm with a free hole concentration as high as $5x10^{18}$ cm^{-3} was obtained in Mg doped $In_{0.22}Ga_{0.78}N$. We have measured the energy level of Mg acceptor (E_A) in Mg-doped $In_xGa_{1-x}N$ alloys for x up to 0.35 using temperature dependent hole concentrations measured from Hall-effect experiments. E_A as low as 43 meV was obtained in Mg doped $In_{0.35}Ga_{0.65}N$. Using low temperature PL measurements, we found that the Mg acceptor levels for x up to 0.22 are in close agreement with E_A obtained from the electrical measurements. The difficulties in obtaining p-type InGaN with even higher In-content are due to the high background election concentration as growth temperature for InGaN alloys becomes lower, which seems to promote the incorporation of donor-like defects and impurities.

Tremendous efforts are still needed to improve the material quality of InGaN alloys in the middle compositional range and to obtain p-type InGaN alloys with the even higher In-content necessary to realize efficient energy devices (solar cell, TE, and PEC) and long wavelength emitters. One of the major obstacles for MOCVD synthesis of nitrides at reduced temperatures is low cracking efficiency of NH_3, which results in a high deficiency of N atoms in high In content InGaN alloys.

References

1. J. Li, K. B. Nam, M. L. Nakarmi, J. Y. Lin, and H. X. Jiang, Appl. Phys. Lett. **81**, 3365 (2002).
2. J. Li, K. B. Nam, M. L. Nakarmi, J. Y. Lin, H. X. Jiang, P. Carrier, and S. H. Wei, Appl. Phys. Lett. **83**, 5163 (2003).
3. S. Nakamura and G. Fasol, *The Blue Laser Diode* Springer, Berlin, 1997, pp. 201–260.
4. V. Y. Davydov, A. A. Klochikhin, R. P. Seisyan, and V. V. Emtsev, Phys. Status Solidi B **229**, R1 (2002).
5. J. Wu, W. Walukiewicz, K. M. Yu, J. W. Ager III, E. E. Haller, H. Lu, W. J. Schaff, Y. Saito, and Y. Nanishi, Appl. Phys. Lett. **80**, 3967 (2002).
6. J. Wu, W. Walukiewicz, K. M. Yu, J. W. Ager III, E. E. Haller, H. Lu, and W. J. Schaff, Phys. Rev. **B 66**, R201403 (2002).
7. M. Trivedi and K. Shenai, J. Appl. Phys. **85**, 6889 (1999).
8. W. Junqiao, J. Appl. Phys, **106**, 011101 (2009).
9. S. Yamaguchi, R. Izaki, K. Yamagiwa, K. Taki, Y. Iwamura, and A. Yamamoto, Appl. Phys. Lett. **83**, 5398 (2003).
10. S. Yamaguchi, Y. Iwamura, and A. Yamamoto, Appl. Phys. Lett. **82**, 2065 (2003).
11. W. Liu and A. A. Balandin, J. Appl. Phys. **97**, 123705 (2005).
12. J. Wu, W. Walukiewicz, K. M. Yu, W. Shan, J. W. Ager III, E. E. Haller, H. Lu, W. J. Schaff, W. K. Metzger, and S. Kurtz, J. Appl. Phys. **94**, 6477 (2003).
13. W. C. Johnson, J. Parsons, and M. C. Crew, J. Phys. Chem. **36**, 2561 (1932).
14. H. P. Maruska and J. J. Tietjen, Appl. Phys. Lett. **15**, 327 (1969).
15. S. Yoshida, S. Misawa, and S. Gonda, Appl. Phys. Lett. **42**, 427 (1983).
16. I. Akasaki, H. Amano, Y. Koide, H. Hiramatsu, and N. Sawak, J. Cryst. Growth **98**, 209 (1989).
17. S. Nakamura. Jpn. J. Appl. Phys. **30**, L1705 (1991).

18. I. Akasaki, T. Kozowa, H. Hiramatsu, N. Sawak, K. Ikeda, and Y. Ishii. J. Lumin. **40**, 121 (1988).
19. J. A. van Vechten, J. D. Zook, and R. D. Horning, Jpn. J. Appl. Phys, **31**, 3662 (1992).
20. S. Nakamura, N. Iwasa, M. Senoh, and T. Mukai, Jpn. J. Appl. Phys., **31**, 1258 (1992).
21. M. Ilegems and R. Dingle, J. Appl. Phys. **44**, 4234 (1973).
22. J. I. Pankove, M. T. Duffy, E. A. Miller, and Berkeyhelser, J. Lumin. **8**, 89 (1973).
23. O. Lagerstedt and B. Monemar, J. Appl. Phys. **45**, 2266 (1974).
24. B. Monemar, O. Lagerstedt, and H. P. Gislason, J. Appl. Phys. **51**, 625 (1980).
25. J. I. Pankove and J. A. Hutchby, J. Appl. Phys. **47**, 5387 (1976).
26. J. I. Pankove, E. A. Miller, and J. E. Berkeyheiser, J. Lumin. **5**, 84 (1972).
27. H. Amano, M. Kitoh, K. Hiramatsu, and I. Akasaki, Jpn. J. Appl. Phys, Part 1 **28,** L2112 (1989).
28. S. Nakamura, T. Mukai, M. Senoh, and N. Iwasa, Jpn. J. Appl. Phys., Part 1 **31**, L139 (1992).
29. S. Nakamura, T. Mukai, and M. Senoh. Appl. Phys. Lett. **64**, 1687 (1994).
30. L. H. Peng, C.W. Chuang, J. K. Ho, C. N. Huang, and C. Y. Chen, Appl. Phys. Lett. **72** 939 (1998).
31. C. H. Ko, Y. K. Su, S. J. Chang, W. H. Lan, J. Webb, M. C. Tu, and Y. T. Cherng, Mater. Sci. & Eng. **B 96**, 43 (2002).
32. http://www.ioffe.ru/SVA/NSM/Semicond.
33. R. P. Vaudo, V. M. Phanse, X. H. Wu, Y. Golan, and J. S. Speck, The Second International Conference on Nitride Semiconductors, Tokushima, Japan, 156 (1997).
34. H. Marchand, X. H. Wu, J. P. Ibbetson, P. T. Fini, P. Kozodoy, S. Keller, J. S. Speck, S. P. DenBaars, and U. K. Mishra, Appl. Phys. Lett. **73**, 747 (1998).
35. C. J. Humphreys, MRS bulletin **33**, 459 (2008).
36. S. R. Lee, A. M. West, A. A. Allerman, K. E. Waldrip, D. M. Follstaedt, and C. R. Abernathy, Appl. Phys. Lett. **86**, 241904 (2005).
37. V. Srikant, J. S. Speck, and D. R. Clarke, J. Appl. Phys. **82**, 4286 (1997).
38. T. Metzger, R. Hopler, E Born, O. Ambacher, M. Stutzmann, R. Stommer, M. Schuster, H. Gobel, S. Christiansen, M. Albrecht, and H. P. Strunk, Philos. Mag. **A77**, 1013 (1998).

39. Y. J. Sun, O. Brandt, T. Y. Liu, A. Trampert, K. H. Ploog, J. Bläsing, and A. Krost, Appl. Phys. Lett. **81**, 4928 (2002).

40. W. R. Busing and H. A. Levy, Acta Crystallogr. **22**, 457 (1967).

41. G. Mahan, B. Sales, and J. Sharp, Phys. Today **50**, 42 (1997).

42. A. F. Ioffe, *Physics of Semiconductors,* (Academic, New York, 1960).

43. R. Venkatasubramanian, Phys. Rev. B **61**, 3091 (2000).

44. B. Poudel, Q. Hao, Y. Ma, Y. Lan, A. Minnich, B. Yu, X. Yan, D. Wang, A. Muto, D. Vashaee, X. Chen, J. Liu, M. S. Dresselhaus, G. Chen, and Z. Ren. *Science* **320**, 634 (2008).

45. T. Matsuoka, Superlattices and Microstructures **37,** 19 (2005).

46. P. Waltereit, H. Sato, C. Poblenz, D. Green, J. Brown, M. McLaurin, T. Katona, S. DenBaars, J. Speck, J. H. Liang, M. Kato, H. Tamura, S. Omori, and C. Funaoka, Appl. Phys. Lett. **84,** 2748 (2004).

47. http://www.lbl.gov/Science-Articles/Archive/MSD-full-spectrum-solar-cell.html.

48. K. Fujii, K. Kusakabe, and K. Ohkawa, Jpn. J. Appl. Phys. **44**, 7433 (2005).

49. K. Fujii, T. Karasawa, and K. Ohkawa, Jpn. J. Appl. Phys. **44**, L543 (2005).

50. I. M. Huygens, K. Strubbe, and W. P. Gomes, J. Electrochem. Soc. **147** 1797 (2000).

51. R. Singh, D. Doppalapudi, T. D. Moustakas, and L. T. Romano, Appl. Phys. Lett. **70**, 1089 (1997).

52. B. N. Pantha, J. Li, J. Y. Lin, and H. X. Jiang, Appl. Phys. Lett. **93**, 182107 (2008).

53. E. Iliopoulos, A. Georgakilas, E. Dimakis, A. Adikimenakis, K. Tsagaraki, M. Androulidaki, and N. T. Pelekanos, Phys. Status Solidi A **203**, 102 (2006).

54. S. Fischer, C. Wetzel, E. E. Haller, and B. K. Meyer, Appl. Phys. Lett. **67**, 1298 (1995).

55. C. G. Van de Walle, C. Stampfl, and J. Neugebauer, J. Crystal Growth **189/190**, 505 (1998).

56. H. O. Pierson, *Handbook of Chemical Vapor Deposition (CVD), 2nd ed.* (Noyes Publications 1999).

57. R. Didchenko, J. E. Alix, and R. H. Toeniskoetter, J. Inorg. Nucl. Chem**.** **14**, 35 (1960).

58. P. Burgraaf, “The Status of MOCVD technology’’, Semiconductor International, pp. 80-83 (July 1993).

59. Instruction manual provided with Hydrogen Purifier Johnson Matthey.

60. I. Hatta, Y. Sasuga, R. Kato, and A. Measan, Rev. Sci. Instrum., **56**, 1643 (1985).

61. D. G. Cahill, Rev. Sci. Instrum. **61**, 802 (1990).

62. D. G. Cahill, H. E. Fischer, T. Klistner, E. T. Swartz, and R. O. Pohl, J. Vac. Sci. Tech. **A7**, 1259 (1989).

63. W. S. Capinski and H. J. Maris, Rev. Sci. Instrm. **67**, 2720 (1996).

64. L. A. Rosenthal, Rev. Sci. Instrum. **32**, 1033 (1961).

65. L. R. Holland, J. Appl. Phys. **34**, 2350 (1963).

66. N. O. Birge and S. R. Nagel, Rev. Sci. Instrum. **58**, 1464 (1987).

67. L. Lu, W. Yi, and D. L. Zhang, Rev. Sci. Instrum. **72**, 2996 (2001)

68. Instruction manual Hall-effect card (for model 7075, Keithley instrument, Inc (1987).

69. S. M. Lee and D. G. Cahill, J. Appl. Phys. **81**, 2590 (1997).

70. Q. S Paduano, A. J. Drehman, D. W. Weyburne, J. Kozlowski, J. Seraflnczuk, J. Jasinski, and Z. Liliental-Weber, Phys. Stat. Sol. (c) **0**, 2014 (2003).

71. J. Bai, M. Dudley, W. H. Sun, H. M. Wang, and Asif Khan, Appl. Phys. Lett. **88**, 051903 (2006).

72. S. Tomiya, T. Hino, S. Goto, M. Takeya, and M. Ikeda, IEEE J. Sel. Top. Quantum, Electron. **10**, 1277 (2004).

73. H. Morkoç, *Nitride Semiconductors and Devices* (Springer, Berlin, 1999), **32**, pp. 149–190.

74. C. Kittel, *Introduction to solid state physics, 7th* ed. (John Wiley & Sons, Inc, 1996).

75. http://www.cmse.ed.ac.uk/AdvMat45/CrystalBasics.pdf.

76. J. Li, Z. Y. Fan, R. Dahal, M. L. Nakarmi, J. Y. Lin, and H. X. Jiang, Appl. Phys. Lett. **89**, 213510 (2006).

77. M. Imura, K. Nakano, N. Fujimoto, N. Okada, K. Balakrishnan, M. Iwaya, S. Kamiyama, H. Amano, I. Akasaki, T. Noro, T. Takagi, and A. Bndoh, Jpn. J. Appl. Phys. **45**, 8639 (2006).

78. C. G. Dunn and E. F. Koch, Acta Metall. **5**, 548 (1957).
79. J. K. Jeong, H. J. Kim, H. C. Seo, H. J. Kim, E. Yoon, C. S. Hwang, and H. J. Kim, Electrochem. Solid-State Lett. **7**, C43 (2004).
80. Y. Taniyasu, M. Kasu, and T. Makomoto, Nature (London) **441**, 325 (2006).
81. K. B. Nam, J. Li, M. L. Nakarmi, J. Y. Lin, and H. X. Jiang, Appl. Phys. Lett. **82**, 1694 (2003).
82. Y. Taniyasu, M. Kasu, and T. Makimoto, Appl. Phys. Lett. **85**, 4672 (2004).
83. M. Hermann, F. Furtmayr, F. M. Morales O. Ambacher, M. Stutzmann, and M. Eickhoff, J. Appl. Phys. **100**, 113531 (2006).
84. T. Ive, O. Brandt, H. Kostial, K. J. Friedland, L. Däweritz, and K. H. Ploog, Appl. Phys. Lett. **86**, 024106 (2005).
85. J. Alam, R. Bathe, R. D. Vispute, J. M. Zavada, C. W. Litton, A. A. Iliadis, and S. N. Mohammad, J. Vac. Sci. Technol. **B22** , 624 (2004).
86. S. Ruvimov, Z. Liiental-Weber, T. Suski, J. W. Ager III, J. Washburn, J. Krueger, C. Kisielowski, E. R. Weber, H. Amano, and I. Akasaki, Appl. Phys. Lett. **69,** 990 (1996).
87. I. H. Lee , I. H. Choi, C. R. Lee, E. J. Shin, D. Kim, S. K. Noh , S. J. Son, K. Y. Lim, and H. J. Lee, J. Appl. Phys. **83**, 5787 (1998).
88. A. Cremades, L. Görgens, O. Ambacher, M. Stutzmann, and F. Scholz, Phys. Rev. B, **61**, 2812 (2000).
89. Z. Chine, A. Rebey, H. Touati, E. Goovaerts, M. Oueslati, B, El Jani, and S. Laugt, Phys. Stat. Sol. (a) **203,** 1954 (2006).
90. A. Dadgar, F. Schulze, T. Zettler, K. Haaberland, R. Clos, G. Straβburger, J. Bläsing, A. Diez, and A. Krost, J. Cryst. Growth **277**, 72 (2004).
91. O. Contreras, F. A. Ponce, J. Christen, A. Dadgar, and A. Krost, Appl. Phys.Lett. **81**, 4712 (2002).
92. C. Lee, H. Y. Lee, H. Shin, C. Kim, H. Ko, J. Han, H. Kim, and K. Lee, Phys. Stat. Sol. (c) **2**, 2137 (2005).
93. V. S. Harutyunyan, A. P Aivazyan, E. R. Weber, Y. Kim, Y. Park, and S. G. Subramanya, J. Phys. D: Appl. Phys. **34**, A35 (2001).
94. A. F. Wright, J. Appl. Phys. **82**, 2833 (1997).

95. I. Vurgaftman, J. R. Meyer, and L. R. Ram-Mohan, J. Appl. Phys. **89**, 5815 (2001).
96. T. Matsutani, M. Kiuchi, K. Shirouzu, A. Yoshioka, R. Shimizu, and S. Takahashi, Solid State Phenom. **107**, 43 (2005).
97. V. Mortet, O. Elmazria, M. Nesladek, M. B. Assouar, G. Vanhoyland, J. D'Haen, M. D'Olieslaeger, and P. Alnot, Appl. Phys. Lett. **81**, 1720 (2002).
98. A. T. Sowers, J. A. Christman, M. D. Bremser, B. L. Ward, R. F. Davis, and R. J. Nemanich, Appl. Phys. Lett. **71**, 2289 (1997).
99. R. Schlesser, R. Dalmau, R. Yakimova, and Z. Sitar, Mater. Res. Soc. Symp. Proc. **693**, I9.4.1 (2002).
100. L. J. Schowalter, G. A. Slack, J. B. Whitlock, K. Morgan, S. B. Schujman, B. Raghothamachar, M. Dudley, and K. R. Evans, Phys. Status Solidi C **0**, 1997 (2003).
101. Z. Gu, L. Du, J. H. Edgar, N. Nepal, H. X. Jiang, J. Y. Lin, and R. Witt, J. Cryst. Growth **297**, 105 (2006).
102. A. Watanabe, T. Takeuchi, K. Hirosawa, H. Amano, K. Hiramatsu, and I. Akasaki, J. Cryst. Growth **128**, 391 (1993).
103. N. Teofilov, K. Thonke, R. Sauer, D. G. Ebling, L. Kirste, and K. W. Benz, Diamond Relat. Mater. **10**, 1300 (2001).
104. K. B. Nam, J. Li, M. L. Nakarmi, J. Y. Lin, and H. X. Jiang, Appl. Phys. Lett. **84**, 5264 (2004).
105. C. M. Zetterling, M. Ostling, K. Wongchotigul, M. G. Spencer, X. Tang, C. I. Harris, N. Nordell, and S. S. Wong, J. Appl. Phys. **82**, 2990 (1997).
106. E. Silveria, J. A. Freitas, M. Kneissl, D. W. Treat, N. M. Jonson, G. A. Slack, and L. J. Schowalter, Appl. Phys. Lett. **84**, 3501 (2004).
107. E. Silveira, J. A. Freitas, O. J. Glembocki, G. A. Slack, and L. J. Schowalter, Phys. Rev. B **71**, 041201 (2005).

108. T. Shibita, K. Asai, S. Sumiya, M. Mouri, M. Tanaka, O. Oda, H. Katsukawa, H. Miyake, and K. Hiramatsu, Phys. Status Solidi C **0**, 2023 (2003).

109. J. Li, J. Y. Lin, and H. X. Jiang, Appl. Phys. Lett. **88**, 171909 (2006).

110. G. I. M. Prinz, A. Landenburger, M. Schirra, M. Feneberg, K. Thonke, R. Sauer, Y. Taniyasu, M. Kasu, and T. Makimoto, J. Appl. Phys. **101**, 023511 (2007).

111. http://www.phys.ksu.edu/area/GaNgroup

112. W. Rieger, T. Metzger, H. Angerer, R. Dimitrov, O. Ambacher, and M. Stutzmann, Appl. Phys. Lett. **68**, 970 (1996).

113. M. G. Kanatzidis, S. D. Mahanti, and T. P. Hogan, *Chemistry, Physics, and Materials of Science and Thermoelectric Materials* (Kluwer Academic/Plenum, New York, 2002).

114. R. Venkatasubramanian, E. Slivola, T. Colpitts, and B. O'Quinn, Nature (London) **413**, 597 (2001).

115. B. C. Daly, H. J. Maris, A. V. Nurmikko, M. Kuball, and J. Han, J. Appl. Phys. **92**, 3820 (2002).

116. H.J. Goldsmid, *Thermoelectric Refrigeration*, Plenum, New York, 1964.

117. G. S. Nolas, J. Sharp, and H. J. Goldsmid, *Thermoelectrics Basic Principles and New Materials Development*, Springer Series in Material Science Vol. 45 (Springer, New York, 2001)

118. http://www.its.caltech.edu/~jsnyder/thermoelectrics/science_page.htm.

119. K. Seeger, *Semiconductor Physics* (Springer, Berlin, 1999).

120. L. Liu, T. Borca-Tasciuc, J. L. Liu, K. Taka, K. L. Wang, M. S. Dresselhaus, and G. Chen, Proceeding of 20th International Conference in Thermoelectric, 340 (2001).

121. D. C. Look, H. Lu, W. J. Schaff, J. Jasiniski, and Z. Liliental-Weber, Appl.Phys. Lett. **80**, 258 (2002).

122. N. Khan, A. Sedhain, J. Li, J. Y. Lin, and H. X. Jiang, Appl. Phys. Lett. **92**, 172101

(2008).

123. C. G. Van de Walle and D. Segev, J. Appl. Phys. **101**, 081704 (2007).

124. P. D. C. King, T. D. Veal, C. F. McConville, F. Fuchs, J. Furthmüller, F. Bechstedt**,** P. Schley and R. Goldhahn, J. Schörmann, D. J. As, K. Lischka, D. Muto, H. Naoi, Y. Nanishi, H. Lu, and W. J. Schaff, Appl. Phys. Lett. **91**, 092101 (2007).

125. J. Piprek, *Semiconductor Optoelectronic Devices* (Academic, San Diego, 2003).

126. K. E. Sichel and J. I. Pankove, J. Phys. Chem. Solids **38**, 330 (1977).

127. G. A. Slack, R. A. Tanzilli, R. O. Pohl, and J. W. Vandersande, J. Phys. Chem. Solids **48**, 641 (1987).

128. S. M. Lee, D. G. Cahill, and R. Venkatasubramanian, Appl. Phys. Lett. **70**, 2957 (1997)

129. S. T. Huxtable, A. R. Abramson, C. L. Tien, A. Majumdar, C. LaBounty, X. Fan, G. Zeng, J. E. Bowers, and A. Shakouri, Appl. Phys. Lett. **80**, 1737 (2001).

130. G. Zeng, J. E. Bowers, J. M. O. Zide, A. C. Gossard, W. Kim, S. Singer, A. Majumdar, R. Singh, Z. Bian, Y. Zhang, and A. Shakouri, Appl. Phys. Lett. **88**, 113502 (2006).

131. M. Takashiri, T. Borca-Tasciuc, A. Jacquot, K. Miyazaki, and G. Chen, J. Appl. Phys. **100**, 054315 (2006).

132. B. Yang, W. L. Liu, J. L. Liu, K. L. Wang, and G. Chen, Appl. Phys. Lett. **81**, 3588 (2002).

133. J. P. Dismukes, L. Ekstrom, E. F. Steigmeier, I. Kudman, and D. S. Beers, J. Appl. Phys. **35**, 2899 (1964).

134. D. G. Cahill, M. Katiyar, and J. R. Ablson, Phys. Rev. B **50**, 6077 (1994).

135. C. Dames and G. Chen, Rev. Sci. Instrum. **76**, 124902 (2006).

136. K. A. McCarthy and S. S. Ballard, J. Opt. Soc. Am. **41**, 1062 (1951).

137. S. Adachi, J. Appl. Phys. **54**, 1844 (1983).

138. L. J. van der Pauw, Philips Res. Rep. **13**, 1 (1958).

139. L. D. Hicks, T. C. Harman, X. Sun, and M. S. Dresselhaus, Phys. Rev. B **53**, R10493 (1996).

140. J. Wu, W. Walukiewicz, K. M. Yu, J. W. Ager III, E. E. Haller, H. Lu, and W. J. Schaff, Appl. Phys. Lett. **80**, 4741 (2002).

141. O. Khaselev and J. A. Turner, Science **280**, 425 (1998).

142. B. N. Pantha, R. Dahal, J. Li, J. Y. Lin, H. X. Jiang, and G. Pomrenke, Appl. Phys. Lett. **92**, 042112 (2008).

143. N. A. El-Masry, E. L. Piner, S. X. Liu, and S. M. Bedair, Appl. Phys. Lett. **72**, 40 (1998).

144. RI. Ho and G. B. Stringfellow, Appl. Phys. Lett. **69**, 2701 (1996).

145. J. Adhikari and D. A. Kofke, J. Appl. Phys. **95**, 4500 (2004).

146. L. K. Teles, M. Marque, L. M. R. Scolfaro, and J. R. Leite, Braz. J. Phys. **34**, 593 (2004).

147. S. Y. Karpov, MRS Internet J. Nitride Semicond. Res. **3**, 16 (1998).

148. H. P. D. Schenk, P. de Mierry, M. Laügt, F. Omnès, M. Leroux, B. Beaumont, and P. Gibart, Appl. Phys. Lett. **75**, 2587 (1999).

149. M. Hori, K. Kano, T. Yamaguchi, Y. Satio, T. Araki, Y. Nanishi, N. Teraguchi, and A. Suzuki, Phys. Status Solidi B **234**, 750 (2002).

150. A. Yamamoto, Y. Nakagawa, T. Sugiura, and A. Hashimoto, Phys. Status Solidi A **176**, 237 (1999).

151. T. Kuykendall, P. Ulrich, S. Aloni, and P. Yang, Nature Mater. **6**, 951 (2007).

152. T. Miyoshi, T. Yanamoto, T. Kozaki, S. Nagahama, Y. Narukawa, M. Sano, T. Yamada, and T. Mukai: Proc. SPIE 6894, 689414 (2008).

153. K. S. Kim, J. K. Son, S. N. Lee, Y. J. Sung, H. S. Paek, H. K. Kim, M. Y. Kim, K. H. Ha, H. Y. Ryu, O. H. Nam, T. Jang, and Y. J. Park: Appl. Phys. Lett. **92**, 101103 (2008).

154. D. Queren, A. Avramescu, G. Bru¨derl, A. Breidenassel, M. Schillgalies, S. Lutgen, and U. Strau, Appl. Phys. Lett. **94**, 081119 (2009).

155. H. Asamizu, M. Saito, K. Fujito, J. S. Speck, S. P. DenBaars, and S. Nakamura: Appl. Phys. Express **1**, 091102 (2008).

156. T. Miyoshi, S. Masui, T. Okada, T. Yanamoto, T. Kozaki, S. Nagahama, and T. Mukai: Appl. Phys. Express **2**, 062201 (2009).

157. Y. Enya, Y. Yoshizumi, T. Kyono, K. Akita, M. Ueno, M. Adachi, T. Sumitomo, S. Tokuyama, T. Ikegami, K. Katayama, and T. Nakamura, Appl. Phys. Express **2** 082101 (2009).
158. S. Chichibu, T. Azuhata, T. Sota, and S. Nakamura: Appl. Phys. Lett. **69**, 4188 (1996).
159. T. Takeuchi, S. Sota, M. Katsuragawa, M. Komori, H. Takeuchi, H. Amano, and I. Akasaki: Jpn. J. Appl. Phys. **36**, L382 (1997).
160. U. T. Schwarz and M. Kneissl, Phys. Stat. Sol. (RRL) **1**, A44 (2007)
161. K. Kumakura, T. Makimoto, and N. Kobayashi, J. Appl. Phys. **93**, 3770 (2003).
162. W. Götz, N. M. Johnson, J. Walker, D. P. Bour, and R. A. Street, Appl. Phys. Lett. **68**, 667 (1996).
163. J. Li, T. N. Oder, M. L. Nakarmi, J. Y. Lin, and H. X. Jiang, Appl. Phys. Lett. **80**, 1210 (2002).
164. T. Makimoto, K. Kumakura, and N. Kobayashi, Appl. Phys. Lett. **79**, 380 (2001).
165. K. Kumakura, T. Makimoto, and N. Kobayashi, Appl. Phys. Lett. **79**, 2588 (2001).
166. P. C. Chen, C. H. Chen, S. J. Chang, Y. K. Su, P. C. Chang, and B. R. Huang, Thin Solid Films **498,** 113 (2006).
167. B. N. Pantha, R. Dahal, J. Li, J. Y. Lin, H. X. Jiang, and G. Pomrenke, J. Electronic Materials, **38,** 1132 (2009).
168. K. Fujii and K. Ohkawa, Jpn. J. of App. Phys. **44**, L909 (2005).
169. N. Kobayashi, T. Narumi, and R. Morita, Jpn. J. of App. Phys. **44**, L784 (2005).
170. S. Yamasaki, S. Asami, N. Shibata, M. Koike, K. Manabe, T. Tanaka, H. Amano, and I. Akasaki, Appl. Phys. Lett. **66**, 1112 (1995).
171. K. Kumakura, T. Makimoto, and N. Kobayashi, Jpn. J. Appl. Phys., Part 2 **39**, 337 (2000).
172. K. Kumakura, T. Makimoto, and N. Kobayashi, J. Cryst. Growth **221**, 267 (2000).
173. T. C. Wen, W. I. Lee, J. K. Sheu, and G. C. Chi, Solid-State Electron. **45**, 427 (2001).
174. D. Iida, M. Iwaya, S. Kamiyama, H. Amano, and I. Akasaki, Appl. Phys. Lett. **93**, 182108 (2008).
175. C. A. Chang, T. Y. Tang, P. H. Chang, N. C. Chen, and C. T. Liang, Jpn. J. App. Phys. **46**, 2840 (2007).

176. K. Kumakura, T. Makimoto, and N. Kobayashi, Jpn. J. Appl. Phys. **39**, L337 (2000).

Appendix A - Publications

1. R. Dahal, **B.N. Pantha,** J. Li, J. Y. Lin, and H. X. Jiang, " InGaN/GaN multiple quantum well solar cells with long operating wavelengths", Appl. Phys. Lett**. 94,** 063505 (2009).
2. **B. N. Pantha,** R. Dahal, J. Li, J. Y. Lin, H. X. Jiang and G. Pomrenke, "Thermoelectric Properties of $In_{0.3}Ga_{0.7}N$ Alloys", Journal of Electronic Materials, **38,** 1132 (2009).
3. **B. N. Pantha,** J. Li, J. Y. Lin, and H. X. Jiang , "Single phase $In_xGa_{1-x}N$ ($0.25 < x < 0.63$) alloys synthesized by metal organic chemical vapor deposition", Appl. Phys. Lett. **93**, 182107 (2008).
4. **B. N. Pantha,** R. Dahal, J. Li, J. Y. Lin, H. X. Jiang, and G. Pomrenke, " Thermoelectric properties of $In_{x}Ga_{1-x}N$ alloys", **Appl**. Phys. Lett. 92, 042112 (2008).
5. **B. N. Pantha,** N. Nepal, T. M. Al Tahtamouni, M. L. Nakarmi, J. Li, J. Y. Lin, and H. X. Jiang, "Correlation between biaxial stress and free exciton transition in AlN epilayers", Appl. Phys. Lett. **91**, 121117 (2007).
6. **B. N. Pantha,** R. Dahal, M. L. Nakarmi, N. Nepal, J. Li, J. Y. Lin, H. X. Jiang, Q. S. Paduano, and David Weyburne, "Correlation between optoelectronic and structural properties and epilayer thickness of AlN", Appl. Phys. Lett. **90**, 241101 (2007).